DYNAMICS OF HEAVY ION REACTIONS INVOLVING COMPOUND AND NON COMPOUND NUCLEUS MECHANISMS

A THESIS

Submitted to the

FACULTY OF SCIENCE

TIET, PATIALA

for the degree of

DOCTOR OF PHILOSOPHY

by

NEHA GROVER

THAPAR INSTITUTE
OF ENGINEERING & TECHNOLOGY
(Deemed to be University)

SCHOOL OF PHYSICS AND MATERIALS SCIENCE

THAPAR INSTITUTE OF ENGINEERING AND TECHNOLOGY

PATIALA-147004, INDIA

NOVEMBER, 2018

Dedicated to

MY BELOVED GOD

AND MY FAMILY

CERTIFICATE

This is to certify that the thesis entitled "**DYNAMICS OF HEAVY ION REACTIONS INVOLVING COMPOUND AND NON COMPOUND NUCLEUS MECHANISMS**" being submitted by **Ms. Neha Grover** for the fulfillment of the requirements for the award of Degree of Doctor of Philosophy in the School of Physics and Materials Science, Thapar Institute of Engineering and Technology, Patiala, is a record of the candidate's own work carried out by her under my supervision. The matter presented in this thesis has not been submitted in part or full for the award of any degree in any university or institute.

Supervisor

Dr. Manoj K. Sharma

Professor

School of Physics and Materials Science

Thapar Institute of Engineering and Technology (TIET)

Patiala- 147004

Punjab (India)

Acknowledgements

"Gratitude is a miracle of its own recognition. It brings out a sense of appreciation and sincerity of a being."∼ Auliq-Ice

I believe He, the supreme force, pushes us to the edge and we feel we are about to fall but rather GOD does that to help us learn to fly. This journey of knowledge and accomplishment wouldn't have been possible without His persistent and positive thrust towards my goal. So, first and foremost, I would like to thanks GOD, the Almighty, for giving me the strength, knowledge, ability and opportunity to undertake this research study and to persevere and complete it satisfactorily. Without his blessings, this achievement would not have been possible.

Undertaking this PhD has been a truly life-changing experience for me and it would not have been possible to do without the support and guidance that I received from numerous people. Throughout this long journey, I have gained a lot by learning to persevere despite hardship. Here, I would like to thank all those people who made this journey considerably pleased and easier, and were always with me during this tenure. At the end of my thesis, it is a pleasant task to express my thanks to all those who contributed in many ways to the success of this study and made it an unforgettable experience for me.

At the very outset, from the core of my heart, I would like to express my sincere gratitude to my esteemed supervisor Prof. Manoj K. Sharma, for not only giving me the opportunity to achieve my dream, but also for showing me what a researcher should strive to be; patient, thorough, passionate and personable. His positive outlook and confidence not only inspired me, but also gave the privilege and honour to share his exceptional scientific knowledge and extraordinary human qualities. He ploughed through several preliminary versions of my text, making critical suggestions and posing challenging questions. In other words, his careful editing contributed enormously to the production of this thesis. His expertise, invaluable guidance, constant encouragement, affectionate attitude, understanding nature, patience and healthy criticism added considerably to my experience. Without his continual inspiration, it would have not been possible to complete this journey. His un-

flinching courage and conviction will always inspire me, and I hope to continue to work with his noble thoughts. I can only say a proper thanks to him through my future work. Big thanks once again go to him for believing in me and encouraging my research. To him, I wish to say 'You are a wonderful supervisor, professor and researcher'. A special word of thanks is also due to Mrs. Sonam Sharma for all her love and affection.

I would like to thank my doctoral committee, Dr. Alka Upadhyaya, Dr. Raj Kumar and Dr. Mahesh Kumar for their valuable suggestions and constructive ideas during the progress report held every six months. I am extremely grateful to Prof. O. P. Pandey, Head, School of Physics and Materials Science, TIET, Patiala and Ex-TIET Dean, Research and Sponsored Projects, for providing the possible research facilities here at TIET Campus and fellowship as a teaching associate well in time. My sincere thanks also goes to Prof. Rafat Siddique, present Dean, Research and Sponsored Projects, TIET, Patiala for providing the grants to attend the conferences and necessary resources to accomplish my research work. Special thanks to Prof. Kulvir Singh for his encouragement and constant moral support throughout my PhD. I greatly appreciate the help and co-operation of all the faculty members and staff of the SPMS for their help and kind support. I am also extremely thankful to Dr. Debabrata Deb and Dr. Bhaskar Chandra Mohanty for helping me to curb the plagiarism.

My acknowledgement will never be complete without the special mention of my lab seniors Dr. Gudveen Sawhney, Dr. Manpreet Kaur, Dr. Gurvinder Kaur, Dr. Kirandeep Sandhu, Dr. Mahesh Kumar Sharma and Dr. Manjeet Singh Gautam. They have provided me a wonderful environment to do research and helped me through their gentle guidance and suggestions during my PhD tenure. My special words of gratitude to Dr. Gurvinder Kaur and Dr. Kirandeep Sandhu for all their support and motivation during the initial days of my stay in the lab. My heartfelt thanks goes to senior cum friend Dr. Rajni Mittal for her support, advice, and affection. Thank you for your understanding and encouragement in many moments of different problems. The discussion and suggestions from you were valuable being a source for moral support that has helped me to write this

thesis. I truly appreciate the bond we share and appreciate your friendship. Ms. Amandeep Kaur also deserves special thanks for her inspirational talks and affectionate behavior.

I would like to express my heartfelt thanks to my fellow labmates, Gurjit Kaur and Ishita Sharma for their co-operation and encouragement. I would also like to extend my thanks to my hostel friends Saloni Sharma and Raveena for all the beautiful time I spent in the hostel. If I have missed out some names, it is on purpose. I would like to acknowledge Kanishka Sharma, Shivani Jain and Aman separately for being a friend before a labmate and hostelmate. Our association goes a long way since days of post graduation and they have been with me ever since then as a friend. I have been lucky enough to have them and extremely thankful for listening, supporting and standing beside me in every problem. Thank you for bearing with me and giving me all the encouragement I needed. I am also thankful to my friend Dr. Dipayan Chattopadhyay for his valuable suggestions to write and improve my thesis. Thanks are also due to my friends from department specially Sangeeta, Deepshikha, Navjot Kaur, Pallavi, Jagroop, Kaushlendra, Manmeet, Arshpreet, Shoaib, Neeraj, Jaspreet, Kundan, Bharti for being so nice, cooperative and helpful.

Lastly the most important, I also thank my entire family for all their love and encouragement. Specially, my paternal uncle cum elder brother Pawan Grover and my younger brother Vishal Grover deserve my gratitude and thanks for supporting me in all of my pursuits and inspiring me to follow my dreams. My thanks also goes to Mrs. Seema Grover for her motivation. I dont think I can ever repay my parents (Mr. Sham Sunder Grover and Mrs. Veena Grover) for their infallible love and support that has always been my strength. They deserve big salute for showing faith in me and giving me liberty to choose what I desired. Their patience and sacrifice will remain my inspiration throughout my life. Thank you mummy and papa for teaching me what books couldn't and for telling me to figure out life's tough problems all by myself. That is what made me understand that they were not tough in the first place. A special thanks goes to my younger cousins Mehak Grover, Priyanka Dhawan and Vivek Grover. During last six months, they kept on reminding me: "Didi, go to lab and write your thesis"!

The financial assistance from Thapar Institude of Engineering and Technology, Patiala in the form of teaching associate is gratefully acknowledged.

Patiala

November, 2018.

(Neha Grover)

List of Publications

I. International Journals:

1. Dynamics of ^{17}F + ^{58}Ni reaction via complete and incomplete fusion processes at above barrier energies.

   Neha Grover, Kirandeep Sandhu, and Manoj K. Sharma

   Nucl. Phys. A **974**, 56-71 (2018).

   doi.org/10.1016/j.nuclphysa.2018.03.010 [Impact factor = 1.992].

2. Decay analysis of pre-actinide and trans-actinide nuclei formed using various projectiles on a ^{197}Au target at E^*_{CN} = 60 MeV.

   Neha Grover, Gurvinder Kaur and Manoj K. Sharma

   Phys. Rev. C **93**, 014603 (2016).

   doi.org/10.1103/PhysRevC.93.014603 [Impact factor = 3.304].

3. Dynamics of ^{47}V* formed in ^{20}Ne+^{27}Al reaction in view of fusion fission and DIC mechanism.

   Neha Grover, Kanishka Sharma, and Manoj K. Sharma

   Eur. Phys. J. A **53**: 239 (2017).

   DOI 10.1140/epja/i2017-12439-6 [Impact factor = 2.799].

4. Analysis of dynamical behavior associated with ^{118,120,122}Xe isotopes.

   Neha Grover, Ishita Sharma, Gurvinder Kaur and Manoj K. Sharma

   Nucl. Phys. A **959**, 10-26 (2017).

   doi.org/10.1016/j.nuclphysa.2016.12.008 [Impact factor = 1.992].

5. Complete and incomplete fusion dynamics of ^{6,7}Li +^{159}Tb reactions around the Coulomb barrier.

   Manjeet Singh Gautam, **Neha Grover**, and Manoj K. Sharma

   Eur. Phys. J. A **53**: 12 (2017).

   DOI 10.1140/epja/i2017-12198-4 [Impact factor = 2.799].

6. Role of rotational energy and deformations in the dynamics of ^{6}Li+^{90}Zr reaction [Not part of this thesis].

   Gurvinder Kaur, **Neha Grover**, Kirandeep Sandhu and Manoj K. Sharma

   Nucl. Phys. A **927**, 232-248 (2014).

   doi.org/10.1016/j.nuclphysa.2014.04.033 [Impact factor = 1.992].

7. Fragmentation and related aspects of ^{28}Si + ^{90}Zr$\rightarrow^{118}$Xe* reaction over E$_{c.m.}\approx$ 65-92 MeV.

   Neha Grover, and Manoj K. Sharma

   AIP Conference Proceedings **2006**, 030007 (2018).

   doi.org/10.1063/1.5051263

II. International and National Conferences, Symposiums and Workshops:

1. Study of complete and incomplete fusion processes observed in ^{8}B induced reaction, **Neha Grover**, Gurvinder Kaur and Manoj K. Sharma, Page No. 25, National Conference on emerging challenges in nuclear and many body physics (ECNMP-2014), Nov. 10-11, (2014) Jammu University Jammu.

2. Fusion-fission and quasi-fission contribution in decay of heavy mass nuclei, Gurvinder Kaur, **Neha Grover**, and Manoj K. Sharma, Proceedings of the DAE Symp. on Nucl. Phys. **59**, 344 (2014).

3. Decay analysis of ^{9}Be induced reactions using stable and non-deformed targets, Shilakha Dawar, **Neha Grover**, Gurvinder Kaur, Manoj K. Sharma, Proceedings

of the DAE Symp. on Nucl. Phys. **60**, 404 (2015).

4. Effect of breakup channel on fusion dynamics. Manjit Singh Gautam, **Neha Grover**, and Manoj K. Sharma, Page No. 27, National Conference on recent trends in nuclear physics 15-16 Feburary, (2016) AMU, Aligarh.

5. Effect of pairing strength on dynamics of ^{118}Xe nucleus formed in ^{28}Si+^{90}Zr reaction, **Neha Grover**, Gurvinder Kaur and Manoj K. Sharma, Proceedings of the DAE-BRNS Symp. on Nucl. Phys. **61**, 586 (2016).

6. Decay Analysis of ^{118}Xe* Nucleus Formed in ^{28}Si Induced Reaction, Manoj K. Sharma, **Neha Grover**, World Academy of Science, Engineering and Technology, International Journal of Physical and Mathematical Sciences Vol:3, No:5, (2016).

7. Complete and incomplete fusion dynamics of ^{9}Be induced reaction Manoj K. Sharma, **Neha Grover**, and Shivangi Gupta, Page No. 51, The International Symposium on Physics of Unstable Nuclei (2017) (ISPUN17) Halong City, Vietnam.

8. Role of projectile breakup channel on fusion of ^{7}Li + ^{152}Sm reaction, Manjeet Singh Gautama, K.Vinoda, Hitender Khatri, **Neha Grover**, and Manoj K. Sharma, Proceedings of the DAE-BRNS Symp. on Nucl. Phys. **62** , 482 (2017).

9. Alpha radioactivity of the A=110 isobars near N=Z line, Kanishka Sharma, **Neha Grover**, and Manoj K. Sharma Proceedings of the DAE-BRNS Symp. on Nucl. Phys. **62**, 246 (2017).

Contents

List of Figures

List of Tables

Abstract

The main objective of the present work is to carry out a comprehensive analysis of decay patterns of different compound systems formed in heavy ion induced reactions at low energy regime. The dynamics of both compound nucleus (CN) and non compound nucleus (nCN) decay mechanisms is studied by using the dynamical cluster-decay model (DCM), which estimates the relative probability of all the decay channels/fragments by treating them on equal footing. For CN mechanism, the DCM is applied to explore the decay paths of compound nuclei in view of complete fusion (CF) and incomplete fusion (ICF) processes. Further, the contribution of nCN component in heavy ion reactions is investigated in the form of deep inelastic collisions (DIC) and quasi fission (QF) processes. Also, the relevance of excitation energy, deformations, orientations, angular momentum, and isospin (N/Z ratio) is studied for both CN and nCN mechanisms. The thesis is organized into seven chapters, as briefly outlined below.

Chapter 1 begins with a brief relevance of nuclear physics applications to mankind. Further, it provides an overview of different nuclear reactions and corresponding decay mechanisms along with relevant examples of theoretical and experimental studies. Since the present work includes the comprehensive analysis of compound nucleus (CN) and non compound nucleus (nCN) mechanisms, the discussion related to these processes is emphasized in particular. Also, the role of excitation energy, angular momentum, deformations and orientations etc. is briefly described. In this way, this chapter introduce the general framework to address the motivation of the present work.

Chapter 2 gives the details of methodology used, the Dynamical cluster-decay model

(DCM), which is originated from the quantum mechanical fragmentation theory (QMFT). In this chapter, the DCM is explicitly discussed to address the CN decay modes (ER, IMF, HMF and fission) observed in complete fusion (CF) and incomplete fusion (ICF) processes. Besides this, the formalism for nCN mechanisms such as deep inelastic collisions (DIC) and quasi fission is also explained. To study these processes, the DCM predominantly acquire the co-ordinates η and R of QMFT and works in two phases, where in the first phase, it computes the quantum mechanical preformation probability (P_0) of fragments or clusters in the parent nucleus and the second step determines the penetrability (P)(using WKB approximation) of those clusters or fragments through the interaction barrier. The preformation probability is calculated by solving the stationary Schrödinger wave equation in mass asymmetry [η=(A_1-A_2)/(A_1+A_2)] co-ordinates. In this equation, the fragmentation potential V(η,R,T) serves as an essential input and is calculated by the summing up the binding energies, Coulomb potential, proximity potential and angular momentum dependent potential. Also, it is relevant to mention here that while going through the above mentioned process, DCM includes the effect of all essential components such as excitation energy, temperature (T), angular momentum (ℓ), deformations ($\beta_{\lambda i}$) and orientations (θ), etc. Furthermore, the exploration of neck length parameter (ΔR) and thus its relevance in barrier characteristics is also briefly discussed. Finally, the method to calculate the decay cross-sections and the emission time for both CN and nCN processes is described.

In **Chapter 3**, the dynamical aspects of reactions forming even mass isotopes of $^{118,120,122}Xe^*$ nuclei are examined using the collective clusterization approach of DCM. In reference to the experimental data, the ER cross-sections of the aforementioned nuclei formed in asymmetric reactions ($^{28}Si+^{90,92,94}Zr$) are calculated over a wide range of energy ($E_{c.m.}$≈63-93 MeV). Next, the role of excitation energy (or temperature), deformations, orientations and angular momentum etc. is investigated for the chosen reactions. In order to account for the role of deformations, the calculations are made by using spherical fragmentation as well as with the inclusion of quadrupole (β_{2i}) and hexdecapole (β_{2i-4i})-deformation within optimum and compact orientation approach respectively. Also, the

effect of isospin (N/Z ratio) on decay fragments is explored in view of the fragmentation analysis and preformation probability of ^{118,120,122}Xe* nuclei. Additionally, the role of projectile nucleus is also explored by studying the fragmentation path of ^{118}Xe* nucleus in comparison to ^{123}Ba* system. Further, the ER cross-sections are predicted for different even mass isotopes of Xe, ^{116,118,120,124}Xe.

In **Chapter 4**, the dynamics of ^{6}Li + ^{159}Tb and ^{17}F + ^{58}Ni reactions involving loosely bound beams is explored using DCM. All calculations are made for β_{2i}-deformed choice of fragments using the optimum orientation approach. In view of the loosely bound nature of projectiles (^{6}Li, ^{17}F), the main emphasis of this chapter is to explore the relative contribution of complete fusion (CF) and incomplete fusion (ICF). Thus, the comparative analysis of decay profiles associated with CF and ICF for both reactions is studied in the form of fragmentation potential, mass distribution, penetration probability and barrier modification etc. Further, the decay cross-sections corresponding to CF and ICF are calculated for both reactions in reference to the available experimental data at given energy range. Besides this, the decay paths of the nucleus formed via loosely bound (^{17}F) and tightly bound (^{16}O) projectiles are compared for better understanding of the dynamics involved. Furthermore, the role of temperature-dependent pairing strength is analyzed in terms of the binary fragmentation of the compound system, ^{75}Rb* formed in ^{17}F + ^{58}Ni reaction.

In **Chapter 5**, Decay mechanism of ^{47}V* formed in direct kinematics (^{20}Ne + ^{27}Al) is investigated within collective clusterization approach of Dynamical Cluster-decay Model (DCM). All calculations are done for quadrupole (β_{2i}-deformed) choice of fragments by taking optimum orientations over a wide range of center of mass energies ($E_{c.m.}\sim$ 83 - 125 MeV). According to the experimental evidence, there is a strong competition between Fusion fission (FF) and deep inelastic collision (DIC) in the decay of ^{47}V*, which are recognized as compound nucleus process and non compound nucleus process respectively. The decay cross sections of ^{47}V* for both FF and DIC decay modes are addressed using

DCM, and are found to be in agreement with the experimental data. Also, the behavior of fragmentation potential, preformation probability, penetrability and emission time etc. is examined, in a way to identify the most favorable isotopes contributing towards FF and DIC. It is important to mention that emitting fragments in both these decay channels maintain their homogeneity in terms of charge number, that lie in region $3 \leq Z \leq 9$. Hence, all possible isotopes contributing towards $3 \leq Z \leq 9$ are taken into consideration. Calculations of both FF and DIC are segregated on the basis of angular momentum (ℓ) windows, where $0 \leq \ell \leq \ell_{cr}$ is taken for FF and $\ell_{cr} < \ell \leq \ell_{gr}$ for DIC, as the later operates only due to the partial waves near grazing angular momentum. Additionally, the FF and DIC cross-sections are predicted at three center of mass energies ($E_{c.m.}$=93, 98, and 103 MeV).

In **Chapter 6**, The DCM is applied to study the decay of odd mass nuclei $^{215}Fr^{*}$, $^{223}Pa^{*}$, $^{227}Np^{*}$ and $^{233}Am^{*}$, which are formed in heavy ion induced reactions. The aim of this study is to investigate the decay pattern and related behavior of these heavy mass nuclei formed in four distinct reactions involving different projectiles (with mass A=18-36) induced on ^{197}Au target nucleus. Further, in order to analyze the role of deformations, the calculations are done by considering spherical choice of fragmentation as well as with inclusion of quadrupole (β_2) deformation. According to the available data, fission is the dominant decay mode for given nuclei, thus an attempt is made to investigate the effect of projectile mass in reference to fission decay patterns of the preactinide - $^{215}Fr^{*}$ nucleus and the transactinide nuclei- $^{223}Pa^{*}$, $^{227}Np^{*}$, $^{233}Am^{*}$ formed at common excitation energy, E^{*}_{CN}=60 MeV. Besides this, the shell closure effects and the role of orientation is explored, which suggest the presence of non compound nucleus process such as the quasi fission (QF) for the odd mass nuclei under consideration. For both the compound nucleus and the non-compound nucleus processes, the results obtained using DCM are found to have nice agreement with experimental observations. Furthermore, the isotopic and isobaric analysis is also worked out so as to have comprehensive idea about the dynamical

evolution of considered reactions.

Finally, **chapter 7** summarize the present work. A brief discussion on the results obtained and conclusions drawn is given in this chapter. Also, the significance and scope for the possible extension of present work is described in the end.

Chapter 1

Introduction

The origin and evolution of the universe encompass many fascinating questions such as; What is our place in the universe, how did everything started, from galaxies, stars, planets etc. and what is the possible future timeline of the universe. This evolution of universe is completely a miracle and the planet where we live is also full of wonders. Some of the greatest wonders of nature are found in the tiny world of atoms and molecules, which make up all the visible matter in the universe from the smallest soil particles to the largest stars, galaxies and planets. The atom's internal structure was an enigma for the scientists until the discovery of nucleus by Rutherford in 1911. The experiment, which proved the existence of nucleus was accomplished by Hans Geiger and Ernest Marsden under the supervision of Rutherford. Even today, this experiment is considered to be a paradigm in the series of scattering experiments. Because the discovery of nucleus pointed the way to new domain of nuclear physics and opened numerous doors for new developments like Bohr's model and Quantum theory. Thus, it is considered to be almost the real beginning of the nuclear field, due to which the Rutherford is arguably said to be the founder of this area. However, the traces of nuclear physics were first realized in 1896 via discovery of radioactivity by Becquerel and in 1898, when Curies got success in their experiment to segregate the naturally appearing element, Radium (Z = 88) from the ore. Curies demonstrated the radioactivity more distinctively by their experiment but like Becquerel,

they did not scrutinize the emission of three different types of radiation (α, β and γ) and hence they were also unable to realize the existence of nucleus inside the atom. Therefore, instead of late 19^{th} century, the beginning of the early 20^{th} century is considered to be the time of main origin of nuclear physics, when the nucleus (in 1911) was discovered. Moreover, the name (nuclear physics), itself reveals that it is the branch of physics which mainly depicts the study associated with the atomic nucleus.

According to the currently accepted picture, the compact structure of nucleus representing the core of an atom, is incorporated with closely packed two fermions termed as protons (p^+, positively charged) and neutrons (n^0, neutral). Even though, the tiny nucleus occupies a volume of dimension much smaller (around 10^{-5} times) than the atom, the mass of nucleus is equivalent to 99.9% of the atomic mass. Thus nucleus is much heavier than the electrons (e^-s; negatively charged), which revolve around it within an atom. Now, the question on the existence of nucleus with only positive charge was solved after the discovery of the strong force, which is one of the four elementary forces. These elementary forces (weak, gravitational, strong and electromagnetic) are responsible for all types of interactions in the universe from very small-sized nucleons (neutrons and protons) in the nucleus to the huge astrophysical entities such as neutron stars (gigantic nuclei). Thus to understand the dynamics involved in various nuclear reactions, nuclear forces act as an essential probe and are responsible for understanding of various nuclear properties. Numerous mathematical models were developed to interpret these extensive nuclear properties and related nuclear structure effects. The classical picture of nucleus can be viewed through Liquid drop model (LDM), which elucidated the binding energy curve, constant density and fusion-fission dynamics very well using macroscopic approach. Further, to reach the quantum mechanical part of the nucleus or to understand the microscopic properties viz. non uniform dispersal of nucleons, nuclear spectra, stability due to magic numbers of protons and neutrons, magnetic moment and angular momentum etc., the LDM approach was ameliorated by means of shell model. Thus, for better description of nuclear behavior, various models were developed such as Nilsson Model to explain de-

formations and orientations etc., Collective Model to illustrate magnetic rotation, super deformations, and vibrations etc., and the Unified model to demonstrate more realistic picture of nucleus using combined features of collective and shell model.

This great evolution of nuclear physics clearly reveals that, it incorporate all aspects of physical world from diminutive level of nuclear regime to the immensely spread of universe. In addition to elementary scientific enterprise, it is also capable of presenting various applications for the welfare of society. These applications include: cancer treatment, nuclear medicine, smoke detectors, medical diagnostic imaging techniques, security systems, supercomputers, nuclear weapons and many more. Considering these diverse and worthwhile applications of nuclear physics, continual ventures are being made to extract more benefits from this area of research. Nowadays, to decipher the mystery of various nuclear phenomenon and to acquire vital information about the forces responsible for the survival of nucleus and hence regarding its structure, nuclear reactions are considered to provide an optimum and requisite tool. Nuclear reaction is a process of striking two nuclei either centrally or peripherally to produce new fragments, and if these fragments are identical to the initial nuclei and there is no loss of kinetic energy then the mechanism is termed as the elastic collision. Further, the beauty of nuclear reactions lies in the fact that these reactions address the different segments of the nucleus at different incident energies and projectile-target combinations. As per the range of bombarding energy (E_{beam}), one may categorize the nuclear reactions in to three brackets, where the first ($E_{beam} \geq 500$ MeV/nucleon) is to emphasis on the behavior of smallest entities of nucleus (quarks, gluons etc.), second ($15 < E_{beam} < 500$ MeV/nucleon) is to deal with nucleonic interactions, and last ($E_{beam} \leq 15$ MeV/nucleon) is to accumulate the information about the nucleus either from its decay (fission, particle evaporation etc.) or from its formation via fusion of nuclei. The present work is mainly focused on the class of reactions, which fall in the lowest energy range ($E_{beam} \leq 15$ MeV/nucleon) and are generally termed as low energy nuclear reactions. Further, the mechanisms occurring in this energy range are explained in the forthcoming section.

1.1 Mechanisms of Nuclear Reactions at low energy

Ever since the initiation of nuclear reactions by Rutherford in 1919 [1], the series of numerous discoveries (viz. nuclear fission, synthesis of superheavy elements etc.) has proved that nuclear reactions have made commendable contributions in the development of nuclear physics and are still continuing. In the beginning, only nucleons (proton, neutron), $^{4}_{2}$He (alpha particle) or other light particle beams were used to effectuate the nuclear reactions. The initial breakthrough in research of nuclear reactions is only due to the invention of particle accelerator like linear accelerator (LINAC) (1929), cyclotron (1931), Van de Graaff (1931) etc. Since then, there has been stupendous evolution in heavy ion accelerators, due to which there has been a rapid progress of various techniques to accomplish nuclear reactions with more energetic and heavy (even more than $^{4}_{2}$He) beams. Heavy ions reactions (HIR) are generally referred to those reactions in which mass of the projectile is equal to or greater than the α-nucleus ($^{4}_{2}$He). These reactions exhibit different characteristics as compared to that for the reactions induced via light particle beams. The Characteristics of heavy ion reactions such as large Coulomb interaction, greater angular momentum, and smaller wavelength associated with relative motion, predominantly differentiate them from light ion induced reactions. The present work is mainly confined on the heavy ion induced reactions at low energy exhibiting various decay mechanisms. Heavy ion collisions provide many opportunities to observe various collective phenomena associated with the interactions of nuclear matter. To bring the stimulation in the study of heavy ion induced reactions, nuclear physicists always designed more challenging experiments than the previous ones which inturn provide more intense and accelerated beams of heavy ions. Initially, only Carbon, nitrogen and oxygen were the available accelerated beams but nowadays, many other HI beams such as ^{28}Si, ^{35}Cl, ^{40}Ar, ^{48}Ca, ^{64}Zn etc. are also accessible. Presently, many accelerators e.g. UNILAC (Universal Linear Accelerator, Germany), GANIL (Grand Accélérator National d'Ions Lourds, France), are available to produce highly intense and more energetic heavy ion beams, which can be used to ac-

complish heavy ion reactions. Reactions induced with heavy ion act as a perfect tool to characterise and produce new isotopes with different number of protons and neutrons. Many times, nuclei produced in such reactions are of unusual ratios of nucleons (protons, neutrons) and exist transiently (even for less than one minute) and thus make them difficult to detect. Because of such experimental situations, the study associated with heavy ion reactions becomes more challenging and vital. In addition to experiments, many theoretical (statistical and dynamical) models are also developed to understand the dynamics of such reactions and subsequent phenomena like elastic or inelastic scattering, reaction cross sections, decay of compound nuclei, and particle production etc. Present thesis work is done by using the collective clusterization approach of Dynamical Cluster-decay Model (DCM) and is mainly focused to the study of decay patterns observe in heavy ion induced reactions i.e. (i) Reactions forming compound nucleus and (ii) Reactions violating compound nucleus formation. Explanation associated with these two types of mechanisms is given below.

1.1.1 Reactions forming compound nucleus mechanism

The compound nucleus mechanism (proposed by Niels Bohr in 1936 [2]) is one of the foremost mechanisms to understand the nuclear reactions at low energy regime and is a fruitful source to extract the information about nuclear structure. This mechanism basically reveals the existence of an intermediate stage (excited compound nucleus) of the nuclear reaction, which forms due to the complete amalgamation of incident particle and target nucleus as a consequence of strong interactions between nuclear constituents. During the formation of compound nucleus (CN), energy and momentum of incident particle disperses among all the nucleons of compound nucleus immediately after the collision of incident particle and target nucleus. Further, the decay of the excited compound nucleus either by emitting light particles or via fission decay mode is considered as the final stage of the reaction. It is noticed that the de-excitation of compound nucleus could be understood via nuclear properties such as angular momentum, excitation energy, parity

etc. and in general it is independent of its formation process. This independence between the two phases (the formation and decay of CN) of the reaction mainly attributes to the quick distribution of energy between the nucleons of CN via incident particle and is the basis of the Bohr's assumption. Apart from this, the randomness of the phases of multiple compound nuclear states (excited states during the collision of two nuclei) is also considered to be responsible for the Compound nucleus to forget about the history of its formation [3]. In 1950, Ghoshal [4] took initiative for the experimental verification of Bohr independence hypothesis by analysing the behavior of same compound nucleus (^{64}Zn) formed through two different channels and provided the experimental evidence of this hypothesis. However, due to the ignorance of angular momentum distributions in Ghoshal's experiment [4], J. R. Grover and R. J. Nagle [5] denied this validation with an argument that angular momentum distributions of compound nucleus formed by different entrance channel should be identical to justify the Bohr's assumption. The questions raised on the validity of independence hypothesis of Bohr was solved by D'Auria *et al.* [6] through their experiment with two different HIRs (^{63}Cu + ^{12}C and ^{59}Co + ^{16}O) forming the same compound nucleus (^{75}Br). In this experiment, both excitation energy and angular momentum were considered to be identical for both entrance channels and the fraction of the cross-sections for protons and alpha particles emission was estimated over a wide span of energies and the obtained results validated the independence hypothesis. Further, this validation became more strong because of the similar results obtained in the experiments of same kind performed by Wong *et al.* (1970) [7], Montgomery and Porile (1970) [8], Vaz *et al.* (1972) [9] and Bisplinghoff *et al.* (1976) [10] for various compound nuclei. Since then, the research in this field is continued and many experiments are being carried out to explore more about the compound nucleus formalism. Many heavy ion beams like ^{16}O, ^{28}Si, ^{32}S, ^{24}Mg, ^{48}Ca etc. have been used to accomplish the CN mechanisms, but nowadays numerous exotic beams (^{6}He, ^{6,7}Li, ^{17}F etc.) with low breakup threshold are also available, which may shed light on some unexplored scenario of compound nucleus processes. Thus, depending upon the different types of projectiles,

compound nucleus mechanism can be broadly classified into two categories termed as: (i) Reactions with tightly bound projectiles, (ii) Reactions with loosely bound projectiles, and the explanation of these two categories is as follows:

(a) Compound nucleus reactions with tightly bound projectiles

At present, numerous heavy tightly bound beams such as ^{16}O, ^{24}Mg, ^{28}Si, and ^{32}S are available and the compound nucleus mechanism, which is predominantly seen in the reactions induced with such projectiles, is termed as complete fusion (CF). Here the CF defines that process, in which the whole projectile directly fuse with the target to form the compound nucleus. Now, the formation of compound nucleus in CF is mainly governed by the internuclear interactions comprising of long range repulsive Coulomb potential (due to electrostatic repulsions between the protons) and cohesive nuclear potential. Apart from this, the centrifugal potential (resulting due to angular momentum (ℓ) effects) also plays an important role and sum of the these three potential is termed as the total potential. However, at ℓ=0 $\hbar$, where the centrifugal potential does not contribute, the total potential is termed as the Coulomb barrier (at T=0 MeV). Further, the kinetic energy associated with the relative motion of two colliding nuclei should be high enough, either to pass over or to penetrate the Coulomb barrier to form the compound nucleus, which is possible only if the repulsive and attractive forces balance each other to bring the two nuclei in a shortest proximity distance where the coalescence between the two can occur with adequate amount of energy [11–14]. The main objective to pursue the study associated with CF is to synthesis various heavy or superheavy elements and thus to extend the periodic table. Moreover, the scrutiny of these reactions has been proven to be the best tool to comprehend the process of quantum tunneling in complex many-body systems [15] and thus provides very useful information regarding the nuclear interactions. Presently, many experimental techniques and theoretical approaches are available to investigate the direct fusion in heavy-ion induced reactions and the evolution of research in these reactions has been explained by Birkelund *et al.* [16, 17] and Back *et al.* [18]. Furthermore,

the research of this field got impetus during the last three or so decades owing to the production of several radioactive ion beams. Nowadays, besides tightly bound nuclei, various loosely bound beams such as ^{6,7}Li, ^{9}Be, ^{8}B, ^{6}He, ^{7}Be are also available and the reactions comprising of such projectiles exhibit different scenario of compound nucleus reactions. The description of weakly bound induced reactions falling under the compound nucleus mechanisms is inscribed in the forthcoming section.

(b) Compound nucleus reactions with loosely bound projectiles

In 1985, the discovery of weakly bound isotope of lithium (^{11}Li) by Tanihata *et al.* [19] led to the emergence of many new branches of nuclear reactions. However, the focus in the present section is primarily on the origin of different CN mechanisms due to weakly bound nuclei. The strange characteristics of weakly bound nuclei such as large deformations, larger radii or spatial extension, low breakup threshold, and large breakup probability are expected to influence the reaction mechanism vigorously. Owing to these distinctive traits, the collisions involving loosely bound incident beams have become one of the fascinating topics of research in low energy nuclear reactions. Extensive experimental and theoretical endeavours have been devoted to get comprehensive knowledge of such reactions [15, 18, 20–24] and are still continued to acquire more deeper insight of nuclear properties. It has been observed that fusion processes containing weakly bound projectiles are strongly affected by the couplings of colliding nuclei owing to the large breakup probability of such projectiles [21, 25–27]. As a consequence of these breakup couplings, different fusion processes such as direct complete fusion (DCF), incomplete complete fusion (ICF), and sequential complete fusion (SCF), may be introduced in the reaction mechanism [28]. The DCF represents that fusion channel, in which there is no prior excitation of the breakup channel and this process is completely homologous to the complete fusion of tightly bound projectiles. Secondly, if prior to the fusion, there is reduction in the flux of intact projectile due to its breakup in the entrance trajectory and only partial absorption of the projectile take place then this process is termed as ICF. Further, in SCF, all breakup fragments

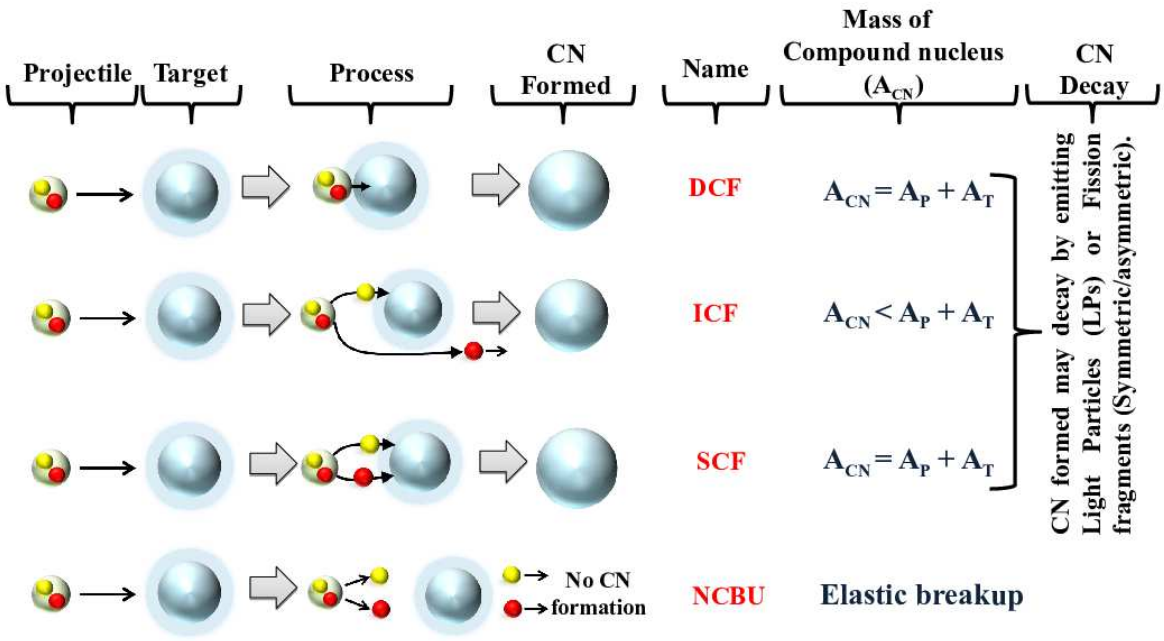

Figure 1.1 Pictorial view of different ways through which weakly bound projectile affect the formation of compound nucleus giving rise to the emergence of various processes [20].

are absorbed by the target in a sequential manner and the CN formed in this process is similar to the CN produced in DCF. For weakly bound projectile induced reactions, the sum of DCF and SCF cross-sections is termed as complete fusion. Experimentally, it is not yet possible to distinguish these two processes (DCF and SCF) though, a theoretical approach for the same has suggested in 2014 by Marta *et al* [29]. Apart from the fusion processes, weakly bound projectiles are also responsible for non capture process in which no breakup fragments are captured by the target and the process is called non capture breakup (NCBU) [15]. However, NCBU does not fall under the category of compound nucleus mechanism and may be interpreted as non compound nucleus process (nCN). The detailed description of nCN processes can be viewed in Sec. 1.1.2. The pictorial view of different possibilities in reactions induced with weakly bound projectile is given in Fig. 1.1.

Besides the formation procedure of compound nucleus, the analysis of the decay mechanism is also an essential subject to comprehend the CN mechanism more precisely. Thus,

after the formation of compound nucleus either through tightly bound or loosely bound projectiles, it is worth to discuss about the decay of compound nucleus through various modes.

(c) Decay mechanisms of compound nucleus

Ever since the finding of Bohr's hypothesis [2], many investigations have been made to perceive the comprehensive knowledge of various decay mechanisms of hot and rotating compound nuclei. In recent past, many statistical approaches were proposed to determine the decay products of compound nuclei. The first statistical hypothesis to deal with the decay of compound nucleus was developed by Bethe [30], Weisskopf and Ewing [31]. They explained the emission of neutrons and light charged particles (p, α) from an excited nucleus and were able to obtain the emission probabilities of these particles along with the cross-sections of continuum states at low excitation energies. Next, Hauser and Feshbach [32] discovered a theory for CN decay mechanism by keeping in mind the conservation of spin and parity in each state of decay. They used the quantum mechanical approach to calculate the cross-sections and emission probability between the discrete levels and hence angular momentum dependence was also included explicitly. Besides the emission of light particles, Hahn *et al.* [33] discovered the disintegration of Uranium by neutron bombardment, which was later named as fission by Meitner and Frisch in 1939 [34]. A few months after this discovery, Bohr and Wheeler [35] suggested a theoretical approach to examine the nuclear fission. Afterwards, the emission of Intermediate Mass Fragments (IMFs; $5 \leq A_2 \leq 20$) and Heavy Mass Fragments (HMFs; $21 \leq A_2 \leq \frac{A}{2}$-20) was also observed in the decay of compound nucleus by means of both experimental and theoretical approaches [36–42]. Further, the concept of multi-step reactions or decay chains was developed by Feshbach *et al.* [43] in 1980.

Subsequent to above mentioned theories for CN decay mechanisms, many statistical codes were developed to estimate the decay cross-sections of different decay modes and to extract the useful information about various nuclear properties. To determine the

evaporation residue cross-sections, statistical codes based on the theory of Hauser and Feshbach [32], such as PACE [44], CASCADE [45] etc. are most commonly used. Further, the alternative forms or the extensions of Hauser-Feshbach formalism like BUSCO code [47] for the emission of IMFs and the Extended Hauser-Feshbach Method (EHFM) [46] to analyze IMFs, HMFs, and fission in light heavy ion induced fission reaction at scission point configuration. Apart from these, GEMINI Monte Carlo statistical emission code [39] for A$\geq$100 and Transition-State Model (TSM) using saddle-point configuration [48,49] are also available for fission analysis.

Compiling the above discussion, one can clearly say that the decay of compound nucleus mainly includes four types of decay modes i.e. ER, IMFs, HMFs and fission and the appearance of these four decay modes depends mainly on the mass of compound nucleus (A_{CN}). Emission of light particles is mostly dominated (with minor contribution of IMFs) in the decay of light mass compound systems ($A_{CN}\leq$80). Further, due to the increment in Coulomb repulsion($\propto Z^2$), decay of intermediate mass compound systems ($80 < A_{CN}\leq$200) find the competition between ER and fission. For heavier compound systems ($A_{CN}>$200), the Coulomb repulsion becomes more dominant than nuclear binding energy ($\propto A^2$) hence, the decay of such systems results into fission either symmetric or asymmetric (includes HMFs) fission products. Despite the competing nature of these decay mechanisms [50, 51], the statistical approaches (mentioned above) address them through separate routes. Gupta and collaborators developed an alternative approach to these statistical methods, which is termed as Dynamical Cluster-decay Model (DCM) [52–59] and has been used in the current work. It is built on well-established Quantum Mechanical Fragmentation Theory (QMFT) [60, 61] and interestingly, all decay modes in DCM are considered on equal footing. The decay of CN in DCM is viewed as dynamical collective mass motion of preformed clusters or fragments through the interaction barrier. More details of DCM are discussed in Chapter 2. Further, the results of decay analysis of compound nuclei in both CF and ICF are presented in chapters 3 and 4 respectively.

Further, in order to get absolute knowledge of HIRs, one can not stay limited to the

aspects of only CN mechanism. Because, the formation of CN may get violated after a particular range of incident energy or due to variable mass asymmetry of the entrance channel, which may lead to the non compound nucleus (nCN) mechanisms and a brief explanation of such reactions is as follows:

1.1.2 Reaction violating compound nucleus hypothesis: non Compound Nucleus Mechanisms

In nuclear domain, the use of various colliding partners (having different shape and size) has always been a fascinating subject of research for both experimentalist and theoreticians, therefore the efforts to make this field more diverse are still continued. Depending upon the incident energy and distinct characteristics of projectile, nuclear reaction may violate the formation of compound nucleus and lead to some other mechanisms such as direct reaction and other competing non compound nucleus (nCN) processes. In direct reactions [62], only one or two nucleons of projectile interact with the one or few nucleons of target and the process occurs so rapidly that the interaction takes place only once without exciting the internal degrees of freedom in any of the interacting clusters or the rest of the nucleus. Stripping and pickup reactions are the best examples for such reactions. Further, in nCN mechanisms, the interaction between the projectile and target becomes gradually faster and the formed composite system re-separate before achieving the equilibration due to which the formation of CN is inhibited in such mechanisms. Seeing such behavior of nCN processes, one can say that the interaction time in nCN is comparatively lesser than in the CN reactions but is larger than the direct reactions or adequately prolonged to transfer the mass and energy. Present work is constrained to CN (ref. Sec. 1.1.1) and nCN mechanisms only. The composite system formed in nCN reactions retains its genesis history, which causes the emergence of entrance channel properties in the outgoing channel. Thus, CN and nCN mechanisms are much different from each other however, one similarity between the two can be observed that they provide useful information about the nuclear structure and related reaction dynamics. Some of

the well known nCN mechanisms are Deep inelastic collisions (DIC), Quasi fission (QF), fast fission (ff) and Pre-equilibrium fission (PEQ). Brief explanation of these processes is given below.

DIC is one of the important nCN mechanisms to explore. It involves the exchange of nucleons between the colliding nuclei to form a dinuclear molecular complex system (DMC), which maintains the remembrance of entrance channel and thus decays into target and projectile like fragments (TLF and PLF) to contribute towards DIC cross-sections. The composite system formed in such collisions are not fully trapped in the pocket of the nucleus-nucleus potential and hence inhibits the formation of compound nucleus. Besides the nucleonic exchange, DI collisions are also identified by the substantial damping of initial kinetic energy (K.E) and angular momentum [63]. Further, the neck degree of freedom is also an important factor to understand the DIC mechanism. The evolution of system after the neck formation may proceed towards the complete equilibration or its splitting before achieving equilibrated CN [64]. It has been observed that DIC mainly occurs at beam energy higher than the Coulomb barrier and for a particular angular momentum window between grazing collisions and capture processes [65]. Moreover, DIC is a useful tool to explore various aspects of nuclear behavior. One of the most important reason is that it is an intermediate process in compound nucleus formation and direct reaction mechanism. Next, to distinguish the DIC and fusion-fission (FF), is also an interesting topic and becomes more challenging for lighter composite systems where the elemental distributions of fragments emitted in DIC and FF are strongly overlapped [66]. Many experimental and theoretical efforts [63–67] have been devoted to differentiate these two processes and in the present thesis work, analysis of the distinction between DIC and FF in the dynamics of light composite system ($^{47}V^{*}$), is presented in chapter 5 using DCM framework. Further, the process bridging the gap between DIC and FF is termed as quasi fission (QF).

The process "quasi-fission" was first named by Swiatecki in 1980 [68]. In this process, the formed composite system disintegrates without passing through the CN configuration

owing to the fact that the composite system in such reactions does not get captured inside the true saddle point, rather it reaches the conditional saddle position [69]. In reaction mechanism terms, QF is equivalent to nucleon exchange between colliding nuclei, although it appears due to the dramatic change in the shape of the system and hence there is a formation of elongated shape composite system in QF (see Fig. 1.2), which evolves quickly towards the scission point. Further, the characteristics such as full energy relaxation, anomalously large fission fragment anisotropies and the large widths of mass asymmetry of fragments produced in outgoing channel represents the QF and the strongly depends on the entrance channel properties. The possibility of its occurrence increases drastically with the increase in sum of Coulomb interaction and rotational energy in the entrance channel, which implies that QF barrier decreases with the increment in intrinsic fusion barrier and hence the probability of composite system to achieve equilibrated CN configuration becomes negligible [70–72]. Furthermore, It has been observed that QF generally contribute in those reactions where the (i) the mean fissility (χ_m) of the colliding system is greater than 0.72, (ii) the coulomb factor ($Z_P Z_T$) surpass 1600 (where, Z_P and Z_T are the charges of projectile and target), and (iii) the mass asymmetry is below the Businaro-Gallone point [73]. However, few exceptional cases not following one or two of the above mentioned characteristics has also been noticed [74]. Besides this, the deformations and orientations of an incoming channel also play a significant role in the emergence of QF [71, 75, 76] such that the projectile colliding at "tips" of the deformed targets leads to the QF, while the collisions at "sides" result in fusion-fission (FF). Since there is a strong competition between QF and FF in many of reactions forming heavy and superheavy elements, many theoretical models and experimental techniques have been developed to estimate the contribution of both processes explicitly. However, there are still various limitations revealing the requirement of more defined theoretical approaches and new experiments [68–77]. Therefore, in the present work, an endeavour has been made to differentiate the contribution of QF and FF in the dynamics of composite systems $^{215}Fr^*$, $^{223}Pa^*$, $^{227}Np^*$, and $^{233}Am^*$ and the detailed analysis is presented in chapter 6.

Furthermore, the composite system formed in QF may evolve further and give rise to the formation of mononucleus having much higher angular momentum (ℓ) states at which the fission barrier vanishes ($\ell_{B_f=0}$). The binary decay of this mononucleus into fission like fragments at $\ell_{B_f=0}$ is termed as fast fission (ff) [78]. In Contrast to ff process, the fission barrier (B_f) in pre-equilibrium fission (PEQ) is non vanishing and it represents the fission of composite system, which is equilibrated in all degrees of freedom, but not in the K mode (projection of the total angular momentum onto the symmetry or fission axis). This non equilibration of K mode is due to inadequacy in the B_f-height to trap the system long enough. The ff and PEQ lie in between FF and QF and can be considered as the future projects within DCM framework. The pictorial representation of some nCN processes is given in Fig. 1.2. Both CN and nCN processes are explored after incorporating the

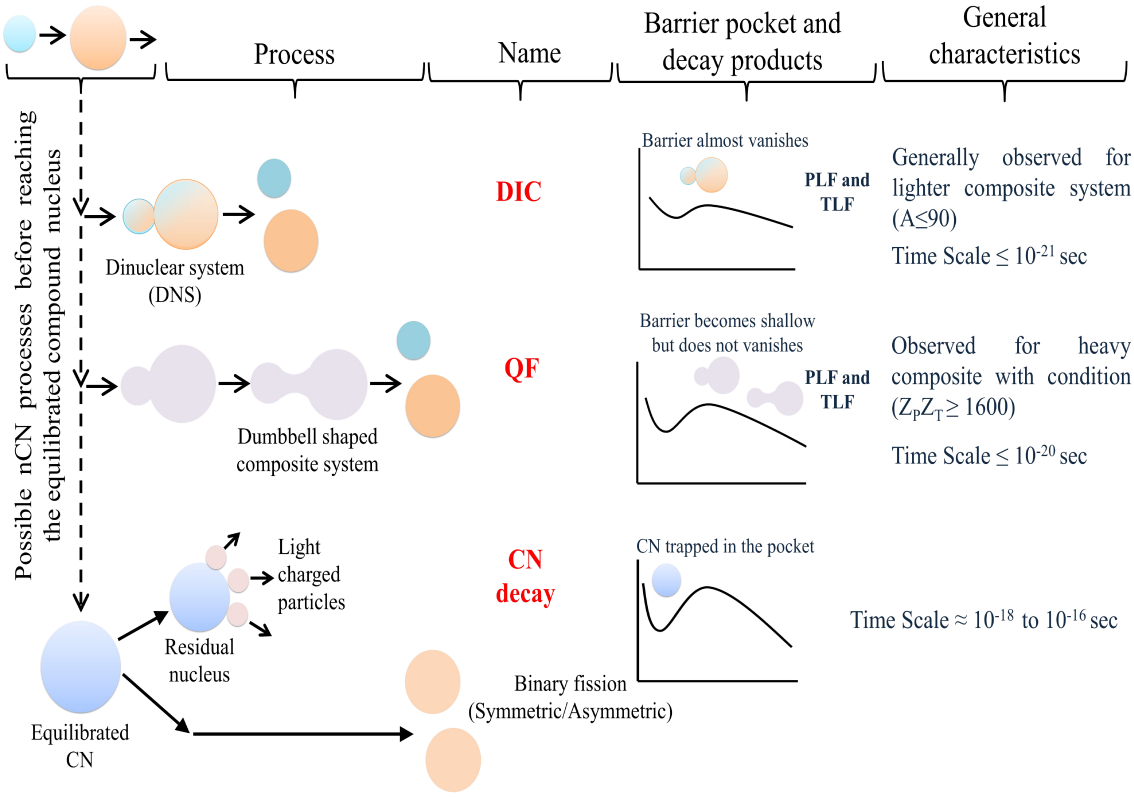

Figure 1.2 Representation of different non compound nucleus (nCN) processes (studied in present work) occurs before achieving the equilibrated compound nucleus (CN) [66, 68, 77].

deformation and orientation effects of decaying fragments and a brief account of same is

given below:

The concept of nuclear deformations was first suggested by Pauli [80] in 1924. He claimed that the hyperfine structure of energy levels of atoms and molecules is due to the electromagnetic interactions with nonspherical nuclei. Afterwards, the experimental justification of the existence of deformations was given by Schüller and Schmidt [81] by observing the quadrupole component in the hyperfine structure of nuclei. Subsequently, the role of deformations in nuclear fission was propounded by Bohr and Wheeler in 1939 [35]. Since then, the quest associated with the new deformations and their role in nuclear reactions has become one of the foremost topics for the nuclear physics community. The magnitude of nuclear deformations is decided by the internal structural properties of the nucleus, which are almost different for each nucleus. Thus, it is expected that the magnitude of deformations and the deviation of nuclear electric field from the spherical symmetry is different for each nuclei. Depending upon the nuclear properties, various sets of nuclear deformations have been observed [82]. The most frequently observed nuclear shapes are quadrupole deformation (β_2), octupole deformation (β_3) and hexadecapole deformation (β_4). Quadrupole deformed nuclei represent the lowest order of deformations and can either be prolate (elongated) or oblate (flattened) depending upon the sign of β_2 where, $\beta_2>0$ indicate the prolate configuration and $\beta_2<0$ signify the oblate shape. Octupole deformed nuclei represent the reflection asymmetric deformation with pear like shape. Further, the β_4-deformation evokes more chaotic behavior than the above mentioned deformations (β_2, β_3) and is very useful to understand the decay mechanisms of super- and hyper-deformed systems. The detailed analysis concerning the role of deformations is presented for the decay of ^{118,120,122}Xe in chapter 3 and for ^{215}Fr*, ^{223}Pa*, ^{227}Np*, and ^{233}Am* in chapter 6.

While discussing the deformations, one can not neglect the orientation degree of freedom of nuclei. Investigations regarding the role of orientations in reaction dynamics had started in the early 20^{th} century after the discovery of deformations and still continues [83–85]. It has been observed that the deformation of nuclei along with the orientation

effects strongly influence the formation and decay mechanisms of heavy ion induced reactions [84, 85]. For example, Some theoretical investigations made in the early 1980s reveal that the prolate-prolate combination of colliding nuclei with particular orientation (0^0, 180^0) is responsible for the reduction in barrier height [84]. Hence, the inclusion of deformations along with the appropriate orientation degree of freedom is essential to understand the nuclear structure and related reaction dynamics. Further, in ref. [86], the optimum (uniquely fixed) orientations are suggested for all combinations of β_2-deformed (prolate, oblate) and spherical nuclei independent of the signs $(+/-)$ of their hexadecapole deformations. The extracted optimum orientations or the results obtained are manifested by two criteria, 'optimum oriented cold fusion' and 'optimum oriented Hot fusion', where cold (elongated) fusion represent the lowest barrier height/largest interaction radius, and the reverse of it represent the case of hot(compact) fusion. The difference between the decay profiles obtained using the hot and cold fusion criteria is presented in the chapter 6.

1.2 Motivation of present work

The field of nuclear reaction dynamics is advancing rapidly and the research in this subject stands on the threshold of an exciting new era. The continual progress in the field has proved that there are no limits to its evolution, thus to expand it more, many new experimental techniques are being constructed or upgraded and more reliable theoretical models are being developed. Both experimental and theoretical groups are dependent on each other and play crucial role in explaining the nuclear reaction dynamics. The current scenario of research in this field states that noble initiative and efforts are required to understand the properties of the nucleus. In this thesis work, the Dynamical Cluster-decay Model (DCM) has been employed to study the decay paths of various compound systems via both compound and non compound nucleus mechanisms. To pursue the present work, various compound nuclei and their isotopes such as $^{47}V^*$, $^{75}Rb^*$, $^{118,120,122}Xe^*$, $^{215}Fr^*$,

^{223}Pa*, ^{227}Np*, and ^{233}Am* are considered to address the following aspects: (i) Heavy ion reaction dynamics using tightly and loosely bound projectiles and thus the comparative analysis of fragmentation process governed via CF and ICF channel is studied. (iii) The concept of nCN processes such as quasi fission (QF) and deep inelastic collision (DIC) and the competition between CN and nCN processes is explored. (iv) The relevance of reaction conditions such as temperature (T), angular momentum (ℓ), deformations (β) and orientations (θ) etc. has been worked out in reference to the different decay mechanisms. (v) Comparison of theoretical results with available experimental data and possible predictions for future. The detailed description of results extracted is presented in chapters 3 to 6.

1.3 Organization of thesis

The configuration of the thesis is as follows:

Chapter 2 describes the details of methodology used, the Dynamical cluster-decay model (DCM) [52–59] , which is based on the quantum mechanical fragmentation theory (QMFT) [60, 61]. In this chapter, firstly the brief review of QMFT is discussed. Then, the formalism of DCM along with its contributing terms such as fragmentation potential, preformation probability, penetrability, neck length parameter and decay cross-sections etc. are explained in view of compound and non compound nucleus processes. The relevant role of excitation energy, temperature (T), angular momentum (ℓ), deformations (β) and orientations (θ) is discussed. The fragmentation distribution of hot and rotating compound nuclei is explained in terms of the preformation probability (P_0) and the influence of barrier characteristics is explored via barrier penetrability calculated using WKB method. The results obtained through DCM calculations are discussed in the succeeding chapters.

In **Chapter 3**, the collective clusterization approach of DCM is applied to study the decay of compound nuclei (^{118,120,122}Xe*) formed in reactions induced with tightly bound

projectile (^{28}Si). Here, in this chapter, the role of excitation energy, deformations, and angular momentum has been investigated for ^{28}Si+^{90,92,94}Zr reactions over a wide range of energy ($E_{c.m.} \approx 63 - 93$ MeV). To investigate the role of deformations, the decay patterns of ^{122}Xe* nucleus are studied in context to the accessible experimental data [87] by using spherical, β_2- and β_4-deformed fragmentation approach. We have used the optimum and compact orientations respectively, for β_2 alone and for β_4 included, which inturn provide nice agreement with the available experimental data. The effect of isospin (N/Z ratio) of decay fragments has been explored in view of the fragmentation analysis and preformation probability of ^{118,120,122}Xe* nuclei and the role of projectile nucleus is also explored by studying the fragmentation path of ^{118}Xe* nucleus in comparison to ^{123}Ba* system. Further, the ER cross-sections have been predicted for various even mass isotopes of ^{116,118,120,124}Xe. After studying the CN mechanism for reactions with tightly bound projectile, the effect of loosely bound projectile in CN decay is explored in **Chapter 4**. Here, the dynamics of reactions induced with loosely bound projectile, ^{6}Li + ^{159}Tb and ^{17}F + ^{58}Ni is studied to investigate the effect of weakly bound beams on CN decay. Firstly, the decay cross-sections of complete fusion (CF) and incomplete fusion (ICF) are calculated for ^{6}Li + ^{159}Tb reaction in DCM framework. In addition to this, the dynamics of ^{17}F + ^{58}Ni reaction induced via a loosely bound projectile (^{17}F) is examined with respect to the experimental data [88] available at beam energies E_{beam} = 54.1 and 58.5 MeV. The calculations are done for quadrupole deformations of fragments using the optimum orientation approach. The comparison of decay outcomes of both CF and ICF is studied using various components such as fragmentation potential, mass distribution, and barrier modification. Different decay modes (ER, IMF, HMF, and fission) are compared to determine the complete fusion and incomplete fusion paths. Finally, the decay paths of the nucleus formed from loosely bound (^{17}F) and tightly bound (^{16}O) projectiles are compared. The role of temperature-dependent pairing strength is also analyzed in terms of the binary fragmentation of the compound system formed. Next, the role of non compound nucleus (nCN) processes is investigated in **Chapter 5** and **Chapter 6**.

In **Chapter 5**, the DCM is employed to investigate the competition between CN (FF) and nCN (DIC) mechanism for ^{20}Ne + ^{27}Al$\rightarrow^{47}$V* reaction over a wide span of energy (E$_{c.m.}\sim$ 83 - 125 MeV). The decay cross-sections of ^{47}V* for both FF and DIC are calculated using quadrupole (β_{2i}-deformed) choice of fragments by taking optimum orientations and are found to be in accordance with the experimental data [89]. Calculations of both FF and DIC are segregated on the basis of angular momentum windows, where $0 \leq \ell \leq \ell_{cr}$ has been taken for FF and $\ell_{cr} < \ell \leq \ell_{gr}$ for DIC, as the later operates only due to the partial waves near grazing angular momentum. In DIC, preformation probability (P$_0$) is divided equally amongst the most favoured outgoing fragments. Moreover, the behavior of fragmentation potential, preformation probability, penetrability and emission time etc. is examined, in way to identify the most favorable isotopes contributing towards FF and DIC. Further, the analysis concerning another nCN process, which bridges the gap between FF and DIC, and is termed as Quasi fission (QF), is presented in **Chapter 6**.

Here, in this chapter, DCM has been applied to study the decay of odd mass nuclei ^{215}Fr*, ^{223}Pa*, ^{227}Np* and ^{233}Am*, which are formed in four distinct reactions involving different projectiles (with mass A=18-36) strike on ^{197}Au target nucleus. According to the referred experimental data, fission is the dominant decay mode for the mentioned compound systems. Thus, the fission decay patterns of given compound system are studied at common excitation energy (E$^*_{CN}$=60 MeV). Besides this, the analysis concerning the shell closure effects and the role of orientation suggests the presence of QF in the decay of odd mass nuclei under consideration, and the possible contribution of QF is estimated. The role of deformations is investigated by considering both spherical and quadrupole (β_2) deformed choice of fragments. For both CN and the nCN processes, the results obtained using DCM are found to have nice agreement with the experimental observations [90]. Additionally, the isotopic and isobaric analysis is also carried out so as to have an extensive knowledge about the dynamics involved.

Finally **Chapter 7** presents the summary and conclusions of this work along with the

discussion concerning the scope for possible extension of the present work.

Bibliography

[1] E. Rutherford, Phil. Mag. **37**, 581 (1919).

[2] N. Bohr, Nature **137**, 344-348 (1936).

[3] Theodore J. Krieger, Ann. of Phys, **31**, 88-99 (1965).

[4] S. N. Ghoshal, Phys. Rev. **80**, 939 (1950).

[5] J. R. Grover and R. J. Nagle, Phys. Rev. **134**, B1248 (1964).

[6] J. M. D′Auria, M. J. Fluss, G. Herzog, L. Kowalski, J. M. Miller and R. C. Reedy, Phys. Rev. **174**, 1409 (1968).

[7] P. Wong, P. J. Daly, and N.T.Porile, Nucl. Phys. A **151**, 549 (1970)

[8] D. M. Montgomery, N. T.Porile, Phys. Rev. C **2**, 595 (1970).

[9] L. C. Vaz, C. C. Lu, J. R. Huizenga, Phys. Rev. C **5**, 463 (1972).

[10] J. Bisplinghoff, J. Ernst, R. Löhr, T. Mayer-Kuckuk, P. Meyer, Nucl. Phys. A **269**, 147 (1976).

[11] W. J . Swiatecki, Nucl. Phys. A **376**, 275- 291 (1982).

[12] M Beckerman, Rep. Prog. Phys. **51**, 1047-1103 (1988).

[13] M. Dasgupta, D. J. Hinde, R. D. Butt, R. M. Anjos *et al.*, Phys. Rev. Lett. **82**, 1395 (1999).

[14] Manjeet Singh, Sukhvinder, and Rajesh Kharab, Nucl. Phys. A **897**, 179-197 (2013).

[15] L.F. Canto, P.R.S. Gomes, R. Donangeloa, J. Lubian, M.S. Hussein, Physics Reports **596**, 1-86 (2015).

[16] J.R. Birkelund, L. E. Tubbs, J. R. Huizenga, J. N. De and D. Sperber, Phys. Rep. **56**, 107 (1979).

[17] J.R. Birkelund, and J. R. Huizenga, Annu. Rev. Nucl. Part. Sci. **33**, 265 (1983).

[18] B. B. Back, H. Esbensen, C. L. Jiang, and K. E. Rehm, Rev. Mod. Phys. **86**, 317 (2014).

[19] I. Tanihata, H. Hamagaki, O. Hashimoto, Y. Shida, and N. Yoshikawa, Phys. Rev. Lett. **55**, 2676 (1985).

[20] P. R. S. Gomes, J. Lubian, L. F. Canto, D. R. Otomar, *et al.* Few-Body Syst **57**, 165-176 (2016); S. Ali, T. Ahmad, K. Kumar, I. A. Rizvi, A. Agarwal, S. S. Ghugre, *et al.* Jour. of Mod. Phys. **5**, 2063-2074 (2014).

[21] L.F. Canto, P.R.S. Gomes, R. Donangelo, M.S. Hussein, Phys. Rep. **424**, 1-111 (2006).

[22] P. R. S. Gomes, I. Padron, E. Crema, O. A. Capurro, *et al.* Phys. Rev. C **73**, 064606 (2006).

[23] N. Keeley, R. Raabe, N. Alamanos, J.L. Sida, Prog. Part. Nucl. Phys. **59**, 579-630 (2007).

[24] N. Keeley, N. Alamanos, K.W. Kemper, K. Ruseka, Prog. Part. Nucl. Phys. **63**, 396-447 (2009).

[25] F. M. Nunes, I. J. Thompson Phys. Rev. C, **59**, 2652 (1999).

[26] K. Hagino, A. Vitturi, C. H. Dasso, and S. M. Lenzi, Phys. Rev. C, **61**, 037602 (2000).

[27] A. Diaz-Torres and I. J. Thompson, Phys. Rev. C, **65**, 024606 (2002).

[28] P.R. S. Gomes, J. Lubian, and L. F. Canto, Phys. Rev. C **79**, 027606 (2009).

[29] H. D. Marta, L. F. Canto, and R. Donangelo, Phys. Rev. C **89**, 034625 (2014).

[30] H. A. Bethe, Phys. Rev. **50**, 332 (1936); Rev. Mod. Phys. **9**, 69 (1937).

[31] V. WeissKopf, Phys. Rev. **52**, 295 (1937); V. WeissKopf and D. H. Ewing, Phys. Rev. **57**, 472 (1940).

[32] W. Hauser and H. Feshbach, Phys. Rev. **87**, 366 (1952).

[33] O. Hahn, F. Strassmann, Naturwissenschaften, **27**, 11 (1939); *ibid* Naturwissenschaften, **27**, 89 (1939).

[34] L. Meitner, O. R. Frisch, Nature **143**, 239 (1939).

[35] N. Bohr, J. A. Wheeler, Phys. Rev. **56**, 426 (1939).

[36] G. Bertsch, Philip J. Siemens, Phys. Lett. **126B**, 9 (1983).

[37] L. G. Sobotka, M. A. McMahan, R. J. McDonald, C. Signarbieux, *et al.*, Phys. Rev. Lett. **53**, 2004 (1984).

[38] S. J. Sanders, R. R. Betts, I. Ahmad, K. T. Lesko, S. Saini, and B. D. wilkins *et al.*, Phys. Rev. C **34**, 1746 (1986).

[39] R.J. Charity, M.A. McMahan, G.J. Wozniak, R.J. McDonald *et al.*, Nucl. Phys. A **483**, 371-405 (1988).

[40] J. Gomez del Campo, R. L. Auble, J. R. Beene, M. L. Halbert *et al.*, Phys. Rev. C **43**, 2689 (1991).

[41] K. Yuasa-Nakagawa, Y.H. Pu, S.C. Jeong, T. Mizota, Y. Futami, S.M. Lee *et al.*, Phys. Lett. B **283**, 185-188 (1992).

[42] Y. Futami, K. Yuasa-Nakagawa, T. Nakagawa, S.M. Lee, *et al.*, Nucl. Phys. A **607**, 85-104 (1996).

[43] Herman Feshbach, Arthur Kerman and Steven Koonin, Ann. of Phys. **125**, 429-476 (1980).

[44] A. Gavron, Phys. Rev. C **21**, 230 (1980).

[45] F. P*ü*hlhofer, Nucl. Phys. A **280**, 267-284 (1977).

[46] T. Matsuse, C. Beck, R. Nouicer, and D. Mahboub, Phys. Rev. C **55**, 1380 (1997).

[47] J. Gomez del Campo, J. L. Charvet, A. D'Onofrio, R. L. Auble, *et al.* Phys. Rev. Lett. **61**, 290 (1988).

[48] S. J. Sanders, A. Szanto de Toledo, and C. Beck, Phys. Rep. **311**, 487-551 (1999).

[49] L. G. Moretto, Nucl. Phys. A **247**, 211-230 (1975); S. J. Sanders, D. G. Kovar, B. B. Back, C. Beck, D. J. Henderson, R. V. F. Janssens, T. F. Wang and B. D. Wilkins, Phys. Rev. C **40**, 2091 (1989); S. J. Sanders, Phys. Rev. C **44**, 2676 (1991).

[50] H. J. Rose and G. A. Jones, Nature **307**, 245 (1984).

[51] R. K. Gupta and W. Greiner, Int. J. Mod. Phys. E **3**, 335-433 (1994).

[52] R.K.Gupta, edited by W.Greiner and R.K.Gupta, Heavy Elements and Related New Phenomenon, **Vol.II**, World Scientific, Singapore, p.536,(Chapter14) (1999).

[53] R. K. Gupta, M. Balasubramaniam, R. Kumar, N. Singh, M. Manhas, and W. Greiner, J. Phys. G: Nucl. Part. Phys. **31**, 631 (2005);R. K. Gupta, M. Manhas, and W. Greiner, Phys. Rev. C **73**, 054307 (2006).

[54] R. K. Gupta, in *Cluster in Nuclei*, Lecture Notes in Physics 818, **Vol. I**, edited by C. Beck (Springer-Verlag, Berlin), p. 223, (2010).

[55] G. Kaur and M. K. Sharma, Nucl. Phys. A **884**, 36 (2012); G. Kaur, N. Grover, K. Sandhu, and M. K. Sharma, Nucl. Phys. A **927**, 232 (2014).

[56] G. Sawhney, G. Kaur, M. K. Sharma, and R. K. Gupta Phys. Rev. C **88**, 034603 (2013).

[57] N. Grover, I. Sharma, G. Kaur and Manoj K. Sharma, Nucl. Phys. A **959**, 10-26 (2017).

[58] M. Singh Gautam, N. Grover, and Manoj K. Sharma, Eur. Phys. J. A **53**: 12 (2017).

[59] N. Grover, K. Sandhu, and Manoj K. Sharma, Nucl. Phys. A **974**, 56-71 (2018)

[60] J Maruhn and W Greiner, Z. Phys. **251**, 431 (1972); R K Gupta, W Scheid and W Greiner, Phys. Rev. Letts. **35**, 353 (1975).

[61] R. K. Gupta, M. K. Sharma, S. Singh ,R. Nouicer and C. Beck, Phys. Rev. C **56**, 3242 (1997); R. K. Gupta, M. K. Sharma, N. V. Antonenko and W. Scheid, J. Phys. G: Nucl. Part. Phys. **25** L47 (1999); M. K. Sharma, R. K. Gupta and W. Scheid, J. Phys. G: Nucl. Part. Phys. **26**, L45 (2000).

[62] S. T. Butler, Phys. Rev. **80**, 1095 (1950); S. T. Butler, Proc. R. Soc. Lond. A, **208**, 559-579 (1951); G. R. Satchler, J. A. Spiers, Proc. Phys. Soc. London A **65**, 980 (1952); N. Austern, S. T.Butler, H. McManus,Phys. Rev. **92**, 350 (1953); J.R. Oppenheimer, M. Phillips, Phys. Rev. **48**, 500 (1935).

[63] Klaus Dietrich, Christiane Leclercq-Willain, Ann. Physics **109**, 41-85 (1977);J R Birkelund, H Freiesleben, *et al.*, Phys. Rev. C **26**, 1984 (1982); W. U. Schroder and J. R. Huizenga, in Damped Nuclear Reactions, Treatise on Heavy-ion Science, edited by D. A. Bromley (Plenum Press, New York, 1984), **Vol. 2**, p. 115; T. Mikhailova *et al.*, Rom. Journ. Phys. **52**, 875-893, Bucharest, (2007).

[64] A Sandulescu, H Scutam and W Scheid, J. Phys. A: Math. Gen. **20**, 2121-2131 (1987); C. E. Aguiar, V. C. Barbosa, L. F. Canto, and R. Donangelo, Phys. Rev. C **38**, 541 (1988).

[65] S. Ayik, D. Shapira, B. Shivakumar, Phys. Rev. C, **38**, 2610 (1988).

[66] C. Beck, B. Djerroud, *et al.*, Z. Phys. A **343**, 309 (1992); A. Dey, C. Bhattacharya, S. Bhattacharya *et al.*, Phys. Rev. C **75**, 064606 (2007).

[67] K. Siwek-Wilczyñska, J. Wilczyñski, Nucl. Phys. A **264**, 115-131 (1976); P. A. Gottschalk and M. Westrom, Phys. Rev. Lett. **39**, 20 (1977); C. M. Ko, D. Agassi, and H. A. Weidenm Ller, Annals of Physics **117**, 237-267 (1979); N. V. Sen *et al.* Phys. Rev. C **22**, 6 (1980); D. Shapira, D. DiGregorio, *et al.*, Phys. Rev. C **28**, 1148 (1983); C Bhattacharya, K. Mullick et al. Phys. Rev. C **66**, 047601 (2002); A. Dey, C. Bhattacharya, S. Bhattacharya *et al.*, Phys. Rev. C **76**, 034608 (2007).

[68] W. J. Swiatecki, Phys. Scr. **24**, 113-122 (1981).

[69] K. Thomas, R. Davies, and Arnold J. Sierk, Phys. Rev. C **31**, 915 (1985); Ch. Ngô, Prog. Part. Nucl. Phys. **16**, 139 (1986).

[70] G. Fazio, G. Giardina, G. Mandaglio, and R. Ruggeri *et al.*, Phys. Rev. C **72**, 064614 (2005).

[71] S. Bhattacharya, A. Chaudhuri, T.K. Ghosh, K. Banerjee *et al.*, EPJ Web of Conferences **86**, 00004 (2015).

[72] R. G. Thomas, D. J. Hinde, D. Duniec, F. Zenke, *et al.*, Phys. Rev. C **77**, 034610 (2008).

[73] J. P. Blocki et al., Nucl. Phys. A **459**, 145 (1986); P. Armbruster, Annu. Rev. Nucl. Part. Sci. **50**, 411 (2000); S. Bjornholm and W. J. Swiatecki, Nucl. Phys. A **391**, 471 (1982); A. Saxena, A. Chatterjee, R. K. Choudhury, S. S. Kapoor, and D. M.

Nadkarni, Phys. Rev. C **49**, 932 (1994); L. M. Pant, A. Saxena, R. K. Choudhury, and D. M. Nadkarni, Phy. Rev. C **54**, 2037 (1996).

[74] S. Appannababu, S. Mukherjee, N. L. Singh, P. K. Rath, *et al.*, Phys. Rev. C **80**, 024603 (2009); A. C. Berriman, D. J. Hinde, R. D. Butt, *et al.*, AIP Conf. Proc. **610**, 608 (2002); R. Sagaidak, A. Yu. Chizhov, I.M. Itkis, *et al.*, AIP Conf. Proc. **853**, 114 (2006); T. K. Ghosh, K. Banerjee, C. Bhattacharya *et al.*, Phys. Rev. C **79**, 054607 (2009); R. G. Thomas, D. J. Hinde, D. Duniec, *et al.*, Phys. Rev. C **77**, 034610 (2008); E. Prasad, K. M. Varier, R. G. Thomas, *et al.*, Phys. Rev. C **81**, 054608 (2010); R. Rafiei, R. G. Thomas, D. J. Hinde, *et al.*, Phys. Rev. C **77**, 024606 (2008); H. Q. Zhang, C. L. Zhang, and C. J. Lin, *et al.*, J. Phys. Conf. Ser. **282**, 012013 (2011); G. N. Knyazheva, E. M. Kozulin, R. N. Sagaidak, *et al.*, Phys. Rev. C **75**, 064602 (2007).

[75] D. J. Hinde, C. R.Morton, M. Dasgupta, J. R. Leigh, J. C. Mein, and H. Timmers, Nucl. Phys. A **592**, 271 (1995).

[76] D. J. Hinde, M. Dasgupta, J.R. Leigh, J.P. Lestone, J.C. Mein, C.R. Morton, J.O. Newton, and H. Timmers, Phys. Rev. Lett. **74**, 1295 (1995).

[77] R. Yanez, W. Loveland, J. S. Barrett, and L. Yao *et al.*, Phys. Rev. C **88**, 014606 (2013); M. G. Itkis, A. A. Bogachev, I. M. Itkis, G. N. Knyazheva, N. A. Kondratiev *et al.*, Int. J. Mod. Phys. E, **16**, 957-968 (2007).

[78] C. Grégoire, C. Ngo and B. Remaud, Nucl. Phys. A **383**, 39220 (1982); R.K.Choudhury and R.G.Thomas, Jour. of Phys.: Conf. Ser. **282**, 012004 (2011); Giovanni Fazio, Giorgio Giardina *et al.*, Mod. Phys. Lett. A **20**, 391-405 (2005).

[79] V. S. Ramamurthy and S. S. Kapoor, Phys. Rev. Lett. **54**, 178 (1985); V. S. Ramamurthy and S. S. Kapoor, Phys. Rev. C **32**, 2182 (1985); D. Naderi, Phys. Rev. C **90**, 024614 (2014); R Tripathi, S Sodaye and K Sudarshan, Pramana J. Phys. **85**, 315-322 (2015).

[80] W. Pauli, Naturwiss. 12, **741** (1924).

[81] T. Schüller and T. Schmidt, Z. Phys. 92, 148 (1934); 94, 457 (1935).

[82] W. Nazarewicz, Progress in Part. and Nucl. Phys. **28**, 307 (1992); W. Nazarewicz and I. Ragnarsson, in: CRC Handbook on Nuclear Decay Modes, 1993.

[83] H. S. W. Massey, Ph.D., Trans. Faraday Soc. **31**, 556 (1935); J. A. Spiers, Nature **161**, 807 (1948); S. H. Hanauer, *et al.* Phys. Rev. **124**, 1512 (1961); J. J. Grob, *et al.*, Phys. Rev. B **11**, 3273 (1975); J. Reinhardt, *et al.* Z. Phys. A - Atoms and Nuclei **303**, 173-188 (1981); Daniel Kikoa, *et al.* Phys. Review C **84**, 054907 (2011).

[84] A J Baltz and B F Bayman, Phys. Rev. C **26**, 1969 (1982); M Münchow , D Hahn and W Scheid, Nucl. Phys. A **388**, 381 (1982); M J. Rhoades-Brown , V E. Oberacker, M Seiwert and W Greiner, Z. Phys. A **310**, 287 (1983); M. Seiwert , W Greiner , V. Oberacker and M J. Rhoades-Brown, Phys. Rev. C **29**, 477 (1984); N. Malhotra and R K Gupta, Phys. Rev. C **31** 1179 (1985).

[85] V. Yu. Denisov and W. Nörenberg, Eur. Phys. J. A **15**, 375-388 (2002); Yu. Ts. Oganessian, V. K. Utyonkov, *et al.* Phys. Rev. C **70**, 064609 (2004); V. I. Zagrebaev, Yu. Ts. Oganessian, *et al.* Phys. Rev. C **73**, 031602(R) (2006); V. Zagrebaev and W. Greiner Phys. Rev. C **78**, 034610 (2008).

[86] Raj K Gupta, M Balasubramaniam *et al.* J. Phys. G: Nucl. Part. Phys. **31**, 631-644 (2005).

[87] S. Kalkal, S. Mandal, N. Madhavan et. al. Phys. Rev. C **81**, 044610 (2010); J. O. Newton, C. R. Morton, M. Dasgupta et. al. Phys. Rev. C **64**, 064608 (2001).

[88] M. Mazzocco, C. Signorini, D. Pierroutsakou, T. Glodariu *et al.* Phys. Rev. C **82**, 054604 (2010).

[89] A. Dey, C. Bhattacharya, S. Bhattacharya, T. K. Rana, S. Kundu, K. Banerjee, S. Mukhopadhyay, S. R. Banerjee, D. Gupta, and R. Saha Phys. Rev. C **75**, 064606 (2007).

[90] R. Yanez, W. Loveland, J. S. Barrett, and L. Yao et al Phys. Rev. C **88**, 014606 (2013).

Chapter 2

Methodology

2.1 Introduction

The key objective of this work is to explore various decay mechanisms and thus to interpret related features such as fragment mass distribution, potential energy surfaces, penetration probability etc. The nuclear reaction dynamics provides a great connection between the experimental and theoretical frontiers, where the unforeseen outcomes of experiments consistently prompt the advancement of theory, and theoretical developments propel the experimental efforts by predicting new phenomena. The theoretical approaches play very important role to interpret the experimental data. Further, an explicit understanding of decay mechanisms demands new challenges in theory, which require high performance computing facilities and advanced scientific codes. Considering the vital specifications, many efforts have been made to understand the decay mechanisms and many are still in progress. In this context, various theoretical models were originated for better understanding of such mechanisms. Initially, only statistical models were used to understand the decay properties, but later on, some (non-statistical) approaches were also established to interpret the dynamics of nuclear systems. In the present thesis work, the collective clusterization approach of Dynamical Cluster-decay Model (DCM) [1–13] has been applied to examine the decay mechanisms and associated dynamical aspects. DCM is originated

from the well-known dynamical (or quantum mechanical) fragmentation theory [14–21], which is briefly discussed in Sec. 2.2. Compared to other statistical models, the main advantage of using DCM is that it estimates the relative probability of all the decay channels by treating them on equal footing. Thus, in DCM, all decay channels are considered as the dynamical collective mass motion of preformed fragments through the interaction barrier. Further details of DCM and its components are described in forthcoming sections.

A brief discussion of quantum mechanical fragmentation theory (QMFT) is presented in Sec. 2.2. Further, the formalism of DCM using QMFT is discussed in Sec. 2.3 followed by the discussion of its components, fragmentation potential in Sec. 2.4, preformation probability (P_0) in Sec. 2.5, penetrability (P) in Sec. 2.6 and the neck length parameter (ΔR) and barrier lowering property in Sec. 2.7. Finally, the decay cross sections in DCM are presented in Sec. 2.8.

2.2 Brief Review of Quantum mechanical fragmentation theory

The QMFT is based on Two Center Shell Model (TCSM), which uses the collective mass transfer and gives the unified description of two body channels in both fusion and decay processes. In QMFT, the average two body potential is computed using macro-microscopic method of Strutinsky [22], which successfully describes both cold and hot fusion reaction dynamics. Here, the fragments are considered to be born prior (pre-born) to the decay of compound system, thus offers the quantum mechanical concept of probability to explore the role of shell effects in decay process. The collective coordinates included in the QMFT are as follows:

(i)The relative separation coordinate R between the two nuclei or fragments (or, equivalently, the length parameter $\lambda = L/2R_0$, where L is length and R_0 is radius of an equivalent spherical nucleus).

(ii) The deformation co-ordinates $\beta_{\lambda i}$ (λ=2,3,4... and i=1,2) of the colliding nuclei.

(iii) The orientation degrees of freedom $\theta_i (i = 1, 2)$ of the deformed nuclei.

(iv)The azimuthal angle ϕ between the principal planes of the two colliding nuclei.

(v)The neck parameter ε, defined by the ratio $\varepsilon = E_0/E'$ for the interaction region $R < R_1 + R_2$ (R_i (i=1, 2) is the radius of the two nuclei). Here E_0 is the actual height of the barrier and E' is fixed barrier of the two center oscillator. $\epsilon = 0$ corresponds to a broad neck formation however, $\epsilon = 1$ shows that the neck is fully squeezed in, corresponding to the asymptotic region ($R > R_1 + R_2$).

(vi) Mass and charge fragmentation co-ordinates [14–16], which for binary fragmentation are defined as:

$$\eta_A = \frac{A_1 - A_2}{A_1 + A_2}; \qquad \eta_Z = \frac{Z_1 - Z_2}{Z_1 + Z_2}; \tag{2.1}$$

Here η_A, and η_Z are respectively the mass, and charge asymmetry coordinates. The domain of η-values is $0 \leq |\eta| \leq 1$ and thus it allows QMFT to give collective explanation of all phenomena ranging from few nucleon transfer to complete fusion and symmetric to super-asymmetric decay of compound system. Furthermore, by using the collective coordinates of QMFT and their velocities, the collective Hamiltonian can be defined as:

$$H = K(\mathbf{R}, \beta, \varepsilon, \eta, \eta_Z; \dot{\mathbf{R}}, \dot{\beta}, \dot{\varepsilon}, \dot{\eta}, \dot{\eta}_Z) + V(\mathbf{R}, \beta, \varepsilon, \eta, \eta_Z). \tag{2.2}$$

Here, "K" and "V" corresponds to the kinetic and potential energy respectively, and β refers to $\beta_{\lambda i}$ (i=1,2; λ=2,3,4...). For the potential $V(\eta, \eta_Z, R)$, minimized in the η_Z co-ordinate, the Schrödinger wave equation in terms of mass parameters η and relative separation co-ordinate R can be noted as:

$$H(\eta, R)\psi(\eta, R) = E(\eta, R)\psi(\eta, R) \tag{2.3}$$

with the Hamiltonian,

$$H(\eta, R) = K(\eta) + K(R) + K(\eta, R) + V(\eta) + V(R) + V(\eta, R) \tag{2.4}$$

To proceed further, the coupling term of the kinetic energy $K(\eta, R)$ (proportional to the $\frac{\partial^2}{\partial\eta\partial R}$) is overlooked here due to very small coupled cranking masses ($\mathrm{B}_{R\eta} \ll (B_{RR}B_{\eta\eta})^{1/2}$ and $\mathrm{B}_{R\eta_Z} \ll (B_{RR}B_{\eta_Z\eta_Z})^{1/2}$) [14,15]. Same is applicable for the coupling term of potential energy ($V(\eta, R)$). Therefore, in the decoupled approximation [21], the Hamiltonian of the Schrödinger equation (2.3) is written as follows:

$$H = \underbrace{-\frac{\hbar^2}{2\sqrt{B_{\eta\eta}}}\frac{\partial}{\partial\eta}\frac{1}{\sqrt{B_{\eta\eta}}}\frac{\partial}{\partial\eta} - \frac{\hbar^2}{2\sqrt{B_{RR}}}\frac{\partial}{\partial R}\frac{1}{\sqrt{B_{RR}}}\frac{\partial}{\partial R}}_{\text{Kinetic energy term}} + \underbrace{V(\eta)+V(R)}_{\text{Potential energy term}} \tag{2.5}$$

The mass parameters B_{ij}, working as an important input of the kinetic energy term in above Eq. (2.5) explain the dynamical aspects in QMFT. These mass parameters (B_{ij}) can either be obtained by using the Asymmetric Two-Center Shell Model ($ATCSM$) wave functions in cranking formula or by using the classical hydrodynamical model of Kröger and Scheid [23], where the later approach is more simplified and also give nice agreement with the microscopic cranking calculations. Further, the static properties of nuclear system can be described by using the potential energy term of above Hamiltonian Eq. (2.5). Therefore, both kinetic and potential energy components play an important role in complete understanding of reaction mechanism.

For decoupled Hamiltonian (shown in 2.5), Schrödinger wave equation (Eq. (2.3)) can be separated for the two co-ordinates η and R as follows,

$$\left[-\frac{\hbar^2}{2\sqrt{B_{\eta\eta}}}\frac{\partial}{\partial\eta}\frac{1}{\sqrt{B_{\eta\eta}}}\frac{\partial}{\partial\eta} + V(\eta)\right]\psi^{\nu}(\eta) = E^{\nu}_{\eta}\psi^{\nu}(\eta) \tag{2.6}$$

and

$$\left[-\frac{\hbar^2}{2\sqrt{B_{RR}}}\frac{\partial}{\partial R}\frac{1}{\sqrt{B_{RR}}}\frac{\partial}{\partial R} + V(R)\right]\psi^{\nu}(R) = E^{\nu}_{R}\psi^{\nu}(R) \tag{2.7}$$

with

$$\psi(\eta, R) = \psi(\eta)\psi(R) \qquad and \qquad E = E_{\eta} + E_{R} \tag{2.8}$$

The states $\psi^{\nu}(\eta)$ are the vibrational states in the potential $V(\eta)$ and are labelled by the quantum numbers $\nu = 0, 1, 2, ...$ The calculations in the DCM are made using Eq. (2.6) in η co-ordinate. The formalism of DCM using QMFT is explained below.

2.3 DCM formalism based on QMFT

DCM [1–13] has been used to investigate the decay paths of various nuclear systems in all mass regions (light, medium, heavy and superheavy) of periodic table over a wide range of beam energy. It has successfully explained both compound and non compound

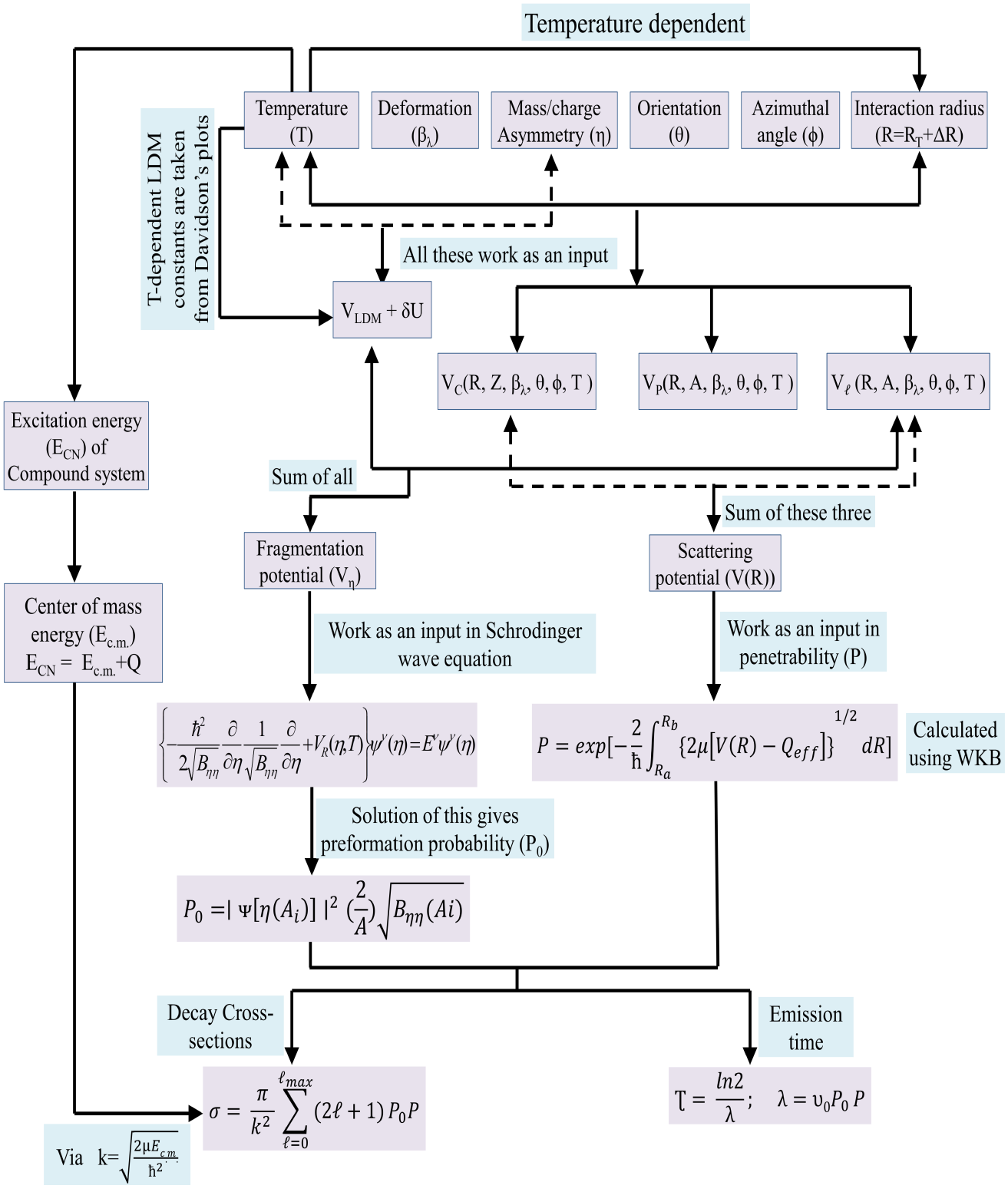

Figure 2.1 A Schematic diagram presenting the formalism of dynamical cluster-decay model.

nucleus mechanisms with the inclusion of all essential components such as excitation energy, temperature (T), angular momentum (ℓ), deformations ($\beta_{\lambda i}$) and orientations (θ), etc. Before explaining the detailed formalism of DCM, a brief review of it is presented through a schematic diagram in Fig. 2.1

In the present thesis work, DCM is explicitly applied to address the CN decay modes (ER, IMF, HMF and fission), observed in complete and incomplete fusion processes. Besides this, the contribution of nCN mechanisms such as deep inelastic collisions (DIC) and quasi fission has also been examined. To study all these processes, DCM predominantly acquires the co-ordinates η and R of QMFT, where "η" characterize the nucleon-division (or exchange) between outgoing fragments, and "R" is used to describe the transfer of kinetic energy of incident channel ($E_{c.m.}$) to internal excitation (total excitation or total kinetic energy, TXE or TKE) of the outgoing channel and this energy transfer can be defined by the following equation.

$$\begin{aligned} E^{*}_{CN} &= E_{c.m.} + Q_{in} \\ &= \mid Q_{out} \mid + TKE(T) + TXE(T) \end{aligned} \tag{2.9}$$

The E^{*}_{CN} in above equation represents the excitation energy of compound nucleus and can also be inscribed in terms of temperature through a semi-empirical statistical formula [24] as follows:

$$E^{*}_{CN} = \frac{A_{CN}}{a}T^2 - T \tag{2.10}$$

where "a" represents the level density parameter and may vary from "8 to 11" depending upon the mass of the compound nucleus (A_{CN}). Further, the Q_{in} in Eq. (2.9) symbolizes the entrance channel Q-value and is obtained using the binding energy (B.E) relation Q_{in}=$B_1 + B_2 - B_{CN}$, where B_i (i=1,2) and B_{CN} represent the binding energies of colliding nuclei and compound nucleus respectively. Next, the center of mass energy ($E_{c.m.}$) of CN can be calculated using the projectile energy E_{beam} as follows:

$$E_{c.m.} = \frac{A_T}{A_{CN}}E_{beam} \tag{2.11}$$

For an ICF process, we assume that the E_{beam} is equally distributed among all its nucleons, and if A^P symbolize the mass number of the projectile before break-up and E/A is the energy per nucleon, then the energy of the initial projectile (before breakup) is given as follows:

$$E_{Projectile} = \frac{E}{A} \times A^P \tag{2.12}$$

Assuming that the velocity of the ejectile is the same as that of the original projectile, the energy of the ejectile particle of mass A^E can be obtained as follows:

$$E_{Ejectile} = \frac{E}{A} \times A^E \tag{2.13}$$

Accordingly, the energy of the part of projectile [13] that hits the target in the ICF is given as follows:

$$E_{ICF}^{beam} = \underbrace{\frac{E}{A} \times A^P}_{E_{projectile}} - \underbrace{\frac{E}{A} \times A^E}_{E_{ejectile}} \tag{2.14}$$

After obtaining the E_{CN}^{*} and $E_{c.m.}$, DCM is used to explore fragmentation process in two phases, where in first phase, it computes the quantum mechanical preformation probability (P_0) of fragments or clusters in the parent nucleus and the second step determines the penetrability (P) of those clusters or fragments through the interaction barrier. The preformation probability, defining the first part of DCM is computed by solving the stationary Schrödinger wave equation Eq. (2.6), in which the fragmentation potential V(η,R,T) serves as an essential input. The description of V(η,R,T) is given in Sec. 2.4 followed by the discussion of preformation probability in Sec. 2.5.

2.4 The Fragmentation Potential $V(\eta)$

The expression for fragmentation potential (or collective potential energy) is given as follows:

$$\begin{aligned} V(\eta,R,T) &= -\sum_{i=1}^{2} B_i(A_i,Z_i,\beta_{\lambda i},T) + V_c(R,Z_i,\beta_{\lambda i},\theta_i,\phi,T) \\ &+ V_p(R,A_i,\beta_{\lambda i},\theta_i,\phi,T) + V_\ell(R,A_i,\beta_{\lambda i},\theta_i,\phi,T) \end{aligned} \tag{2.15}$$

It is evident from the above Eq. (2.15) that V(η,R,T) facilitates to understand the combine effect of all potentials on fragments and thus assists in evaluating the relative stability of decaying fragments. The charges Z_i (i=1,2) of outgoing fragments are fixed by minimizing the potential V(η) in the η_Z coordinate at each η-value. Next, the orientation angle ($0^0 \leq \theta_i \leq 180^0$) represents that angle, which axis of collision makes with the symmetry axis in an anti-clockwise direction [25]. The orientations of deformed nuclei can either be in same plane (coplanar; $\phi = 0^0$) or in different plane (non-coplanar; $\phi \neq 0^0$), however the present work is focused to coplanar orientations only. Further, the internuclear distance (R) at which the fragmentation potential for deformed and oriented nuclei is computed, is given as:

$$R = R_1 + R_2 + \Delta R \tag{2.16}$$

with $R_i(\alpha_i$,T) as,

$$R_i(\alpha_i,T) = R_{0i}(T)[1 + \sum_{\lambda} \beta_{\lambda i} Y_\lambda^{(0)}(\alpha_i)] \tag{2.17}$$

and

$$R_{0i}(T) = [1.28A_i^{1/3} - 0.76 + 0.8A_i^{-1/3}] \times (1 + 0.0007T^2) \tag{2.18}$$

Here, α_i in Eq. (2.17) represents the angle between radius vector ($R_i(\alpha_i)$) and symmetry axis of the colliding nuclei in clockwise direction.

In Eq. (2.15), $B_i(A_i, Z_i, \beta_{\lambda i}, T)$) symbolizes the binding energies of two fragments. In present work, the experimental values of B_i's are taken from the table [26] given by Audi *et al.* and wherever, the experimental B_i's are not available, the theoretical estimates provided by Möller *et al.* [27] are employed. As per Strutinsky renormalization method [22], the binding energies comprise both the macroscopic (liquid drop) and the microscopic (shell correction) parts and can be written as:

$$B(T) = \underbrace{V_{LDM}(T)}_{\text{liquid drop part}} + \underbrace{\delta U exp\left(-\frac{T^2}{{T_0}^2}\right)}_{\text{shell corrections}} \tag{2.19}$$

The T dependent $V_{LDM}(T)$ in above Eq. (2.19) is taken from Davidson *et al.* [28], which follows the "semi-empirical mass formula" of Seeger [29], and is defined as:

$$\begin{aligned} V_{LDM}(A,Z,T) &= \alpha(T)A + \beta(T)A^{\frac{2}{3}} + \left(\gamma(T) - \frac{\eta(T)}{A^{\frac{1}{3}}}\right)\left(\frac{I^2 + 2 \mid I \mid}{A}\right) \\ &\quad + \frac{Z^2}{R_0(T)A^{\frac{1}{3}}}\left(1 - \frac{0.7636}{Z^{\frac{2}{3}}} - \frac{2.29}{[R_0(T)A^{\frac{1}{3}}]^2}\right) + \delta(T)\frac{f(A,Z)}{A^{\frac{3}{4}}} \end{aligned} \tag{2.20}$$

where, $I = a_a(Z-N); a_a = 1.0$ and $f(A,Z)$=(-1,0,1) for even-even, even-odd, and odd-odd nuclei, respectively. The fixed values of α, β, γ and η at T=0 were calculated by Seeger [29] for all even-even nuclei and 488 odd-A nuclei accessible at that time and the values are: $\alpha(0) = -16.11\text{MeV}, \beta(0) = 20.21\text{MeV}$, $\gamma(0) = 20.65\text{MeV}, \eta(0) = 48.00\text{MeV}$ with the pairing energy constant $\delta(0) = 33.0\text{MeV}$ [30]. Later on, these constants of V_{LDM}(T=0) were re-fitted to obtain the experimental binding energies given by Audi *et al.* in 1995 [1,2,31] and 2003 [3,26], where shell corrections were obtained from the empirical formula of Myers and Swiatecki [32]. T-dependence was included in reference to Davidson *et al.* [28]. Further, it is important to note that the T-dependence in pairing energy constant ($\delta(T)$) was modified by the Bansal *et al.* [33] using QMFT based model [34]. According to Davidson *et al.*, the coefficient of pairing energy term ($\delta(T)$) in liquid drop binding energy converges to zero for T> 1.5 MeV because of which the odd-even effect vanishes at higher temperature. However, Bansal *et al.* suggested significant values of $\delta(T)$ even at temperatures higher than 1.5 MeV, which means that the magnitude of modified pairing coefficient decreases slowly with temperature as compared to that for Davidson analysis. The comparison of results obtained using the $\delta(T)$ values of Davidson *et al.* and Bansal *et al.* is discussed in chapter 2.

The second term of Eq. (2.19) corresponds to the microscopic shell corrections, which play a significant role in calculating the nuclear masses, because the nuclear masses estimated by using the smooth liquid drop formula show large deviations with respect to the experimental values. Hence, to acquire the complete description of binding energies, the

consideration of shell corrections is essential along with the liquid drop part of energy. However, at higher excitation energies, the shell corrections are expected to dissipate exponentially (with T_0=1.5 MeV). Further, due to the inadequacy of shell model in light mass region, the description of binding energy with shell corrections (along with V_{LDM}) shows some limitations. Therefore, the combined macro-microscopic estimations of Möller *et al.* [27] are catalogued for $Z \geq 8$ only. Further, the alternative empirical formula of Myers and Swiatecki [32] is also not adequate for light nuclei ($Z \leq 16$). Thus to obtain better description, Gupta and collaborators have refined this empirical method to give the shell corrections for the light as well as heavy mass region, i.e, $1 \leq Z \leq 118$ [2, 3]. Other components (Coulomb (V_C), Proximity (V_P), and centrifugal (V_ℓ)) of fragmentation potential are discussed in the following sub-sections.

2.4.1 The Coulomb potential (V_C)

Coulomb potential (V_C) signifies the presence of repulsive force between the two interacting nuclei, appearing due to their charges and acts along the line joining them. The expression for V_C of two spherical interacting nuclei is defined as

$$V_c = \frac{Z_1 Z_2 e^2}{R} \tag{2.21}$$

To include the effect of deformations and orientations, different expressions have been proposed by different authors [35–38]. In DCM, for the interaction of two deformed and oriented nuclei, V_C is given as:

$$V_c(Z_i, \beta_{\lambda i}, \theta_i, T) = \frac{Z_1 Z_2 e^2}{R(T)} + 3 Z_1 Z_2 e^2 \sum_{\lambda, i=1,2} \frac{R_i^\lambda(\alpha_i, T)}{(2\lambda+1) R(T)^{\lambda+1}} Y_\lambda^{(0)}(\theta_i) \left[\beta_{\lambda i} + \frac{4}{7} \beta_{\lambda i}^2 Y_\lambda^{(0)}(\theta_i)\right] \tag{2.22}$$

where $Y_\lambda^{(0)}(\theta_i)$ symbolizes the spherical harmonics function and for R_i refer Eq. (2.17).

2.4.2 The Nuclear Proximity Potential ($\mathbf{V}_P$)

When the two interacting nuclei attain very small proximity distance, which is comparable to their surface thickness ($\approx 2fm$), or when a compound system is about to separate into two fragments, then the two surfaces confront each other across a small crevice. The additional forces acting at this distance are termed as proximity forces and the corresponding potential is called the nuclear proximity potential. In above situation, the surface energy term alone is not enough and thus the inclusion of proximity potential becomes desirable.

Theory for proximity forces was originally proposed by Deryagin in 1934 [39]. It was later reviewed and modified by Blocki *et al.* [40] in 1977. The equation for proximity potential of spherical nuclei using Blocki's pocket formula is defined as:

$$\begin{aligned} V_P(s_0) &= f(sh., geo.)\Phi(s_0) \\ &= 4\pi\bar{R}\gamma b\Phi(s_0). \end{aligned} \tag{2.23}$$

Where $\overline{R}$ symbolize the mean curvature radius of spherical reaction partners and can be written as:

$$\overline{R} = \frac{R_1 R_2}{R_1 + R_2} \tag{2.24}$$

γ is the specific nuclear surface tension given by

$$\gamma = 0.9517 \left[1 - 1.7826 \left(\frac{N-Z}{A}\right)^2\right] MeV fm^{-2} \tag{2.25}$$

The surface diffuseness (b) in Eq. (2.23) is inscribed as:

$$b = \left[\pi/2\sqrt{3}\ln 9\right]_{t_{10-90}} \tag{2.26}$$

t_{10-90} in above equation represents the thickness of that surface, where the density profile varies from 90% to 10%.

The universal function $\Phi(s_0)$ in Eq. (2.23) does not depend upon the shapes of nuclei or the geometry of nuclear system and can be written as a function of minimum separation distance s_0 as follows:

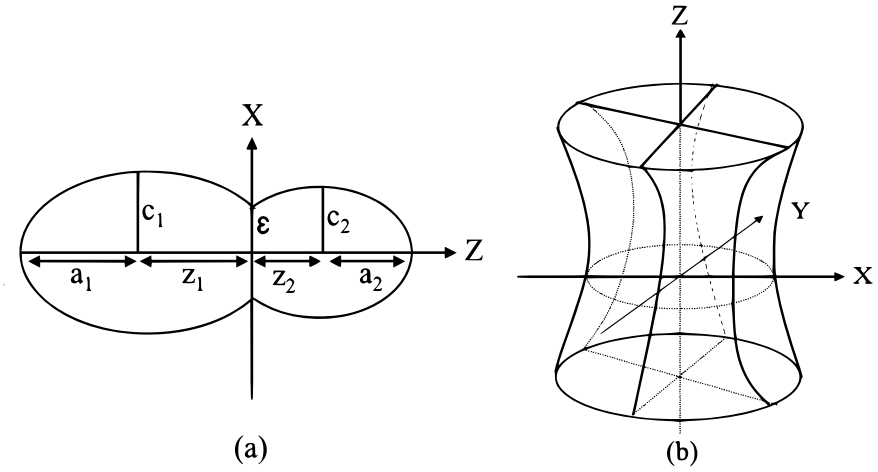

Figure 2.2 (a) Pictorial representation of nuclear shapes formed in two center shell model (TCSM). (b) Schematic representation of a hyperboloid of revolution in one sheet [25].

$$\Phi(s_0) = \begin{cases} -\frac{1}{2}(s_0 - 2.54)^2 - 0.0852(s_0 - 2.54)^3 \\ -3.437exp(-\frac{s_0}{0.75}) \end{cases} \tag{2.27}$$

respectively, for $s_0 \leq 1.2511$ and $s_0 \geq 1.2511$, where negative s_0 represents the overlap region, zero signify touching configuration and its positive values corresponds to the formation of neck between the interacting nuclei.

Apart from the spherical nuclei, the nuclear proximity potential can also be defined for hot deformed nuclei [25, 35] and is defined as:

$$V_p(A_i, \beta_{\lambda i}, \theta_i, T) = 4\pi\bar{R}(T)\gamma b(T)\Phi(s_0(T)) \tag{2.28}$$

Here, the $\bar{R}$ for deformed and oriented nuclei is taken from [25].

Next, the temperature dependent surface diffuseness b(T) is inscribed as:

$$b(T) = \acute{a}(1 + 0.009T^2) \tag{2.29}$$

where, $\acute{a}$ symbolize the diffuseness parameter and in DCM it is taken as 0.99.

The minimum separation s_0 [25] between two deformed and oriented nuclei (for definite value of R), is given as:

$$s_0 = R - R_1 - R_2 \tag{2.30}$$

For R_i (i=1, 2), refer Eq. (2.17).

The proximity potential (V_P) defined in Eq. (2.28) is suitable for $s_0 \geq 0$ only. However, the interactions with $s_0 < 0$ are also possible. In such interactions, two nuclei overlap each

other (see Fig. 2.2(a)). In this case, the system adjusts its shape parameters in such a way that two interacting nuclei form a single indented body like single hyperboloid of one sheet with a hyperboloidal crevice, as shown in Fig. 2.2(b). For such systems (s_0 <0), Gupta and collaborators [43, 44] proposed an expression of V_P based on the Blocki's theory [40] and is given as

$$V_P(s_0) = \pi\gamma b^2 \Phi_1(s_0 = 0) \frac{(c_1^2 + c_2^2 - 2\epsilon^2)}{(z_1^2 + z_2^2)} \tag{2.31}$$

where $\Phi_1(s_0 = 0)$=-2.0306 is the first moment of the universal function Φ at $s_0 = 0$. The shape parameters (c_i, z_i and ϵ) are marked in Fig. 2.2(a).

2.4.3 The Centrifugal Potential (V_ℓ)

Owing to the rotational motion of nuclei, the coriolis or centrifugal forces start emerging in a direction away from the rotational axis. Such forces play significant role in the nuclear interactions and the potential signifying their presence is termed as the centrifugal potential (V_ℓ), which is mainly governed by the angular momentum (ℓ). In nuclear interactions, the orbital angular momentum of the entrance channel is transferred into internal degrees of freedom of the fragments. This transfer is induced by the frictional forces between two nuclei (sliding on each other) and can pass through different stages, where the initial stage of sliding nuclei on each other represents the non-sticking configuration. In the next stage, nuclei start rolling due to viscous force originated during the sliding process. Later on, the rolling process is slowed down by rolling friction, after which the nuclei sticks and start rotating rigidly in a sticking configuration [45]. The limiting value of angular momentum in sticking configuration is greater than that of in non-sticking configuration [3].

The expression of centrifugal potential is given as

$$V_\ell(R, A_i, \beta_{\lambda i}, \theta_i, T) = \frac{\hbar^2 \ell(\ell + 1)}{2I(T)} \tag{2.32}$$

Here, I represents the moment of inertia (MOI), which is different for sticking and non-sticking configuration. The expressions of MOI for both the configurations are as follows:

(a) Sticking moment of inertia (I_S)

$$I_s(T) = \mu R^2 + \frac{2}{5}A_1 m R_1^2(\alpha_1, T) + \frac{2}{5}A_2 m R_2^2(\alpha_2, T). \tag{2.33}$$

(b) Non-sticking moment of inertia (I_{NS})

$$I_{NS}(T) = \mu R^2 \tag{2.34}$$

where, $\mu(= \frac{A_1 A_2}{A_1+A_2}m)$ and m in above equation represents the reduced mass and nucleon mass respectively. R and R_i are defined in Eq. (2.16) and (2.17) respectively. In experiments, the ℓ-value is computed using the non-sticking moment of inertia [3, 46]. However, in DCM calculations, it has been observed that I_S choice of MOI is more appropriate owing to the use of proximity potential (Neck-length surface $\Delta R \leq$ 2 fm) [46]. Therefore the sticking limit has been used to pursue the present thesis work.

After discussing the essential inputs used in Schrödinger wave equation, the solution of it in the form of preformation probability P_0 is described in following Sec. 2.5.

2.5 Preformation Probability (P_0)

The preformation probability, P_0 is an essential component in the DCM as it imparts the structural information of outgoing fragments that is otherwise missing in statistical models. After solving the Eq. (2.6) at fixed R=R_a, one can calculate the probability of formation of fragment (mass (or charge) distribution) at compound nuclear stage and is read as:

$$P_0 \propto |\psi^{\nu}(\eta)|^2 \tag{2.35}$$

where, η in above equation symbolizes the mass asymmetry and can be replaced with η_Z (charge asymmetry) to find the charge distribution of decaying fragments. ν represents the vibrational states of a compound system. The lowest value of ν(=0) indicates the ground state processes such as spontaneous fission or cluster decay, where the higher value of ν(=1,2,3,.....) signify the excited state decay processes. For lowest vibrational state (ν=0; T=0), the mass (or charge) distribution yield, when scaled to a particular mass (say A_2) of one of the fragments ($d\eta = \frac{2}{A}$), is given by:

$$P_0 = |\psi_R^{(0)}(A_2)|^2 \frac{2}{A}\sqrt{B_{\eta\eta}(A_2))} \tag{2.36}$$

Next, to find the preformation probability for excited state decays (ν=1,2,3,.....) or to include the effect of temperature on potential V and masses B_{ij}, the Boltzmann like occupation of excited states is given as

$$|\psi(\eta)|^2 = \sum_{\nu=0}^{\infty} |\psi^{\nu}(\eta)|^2 \exp\left(-\frac{E_{\eta}^{\nu}}{T}\right) \tag{2.37}$$

Further, it is important to mention that we are considering here the directly measurable quantity, the mass (or charge) asymmetry, which works dynamically as mass (or charge) transfer coordinate. Thus, the calculated yields $P_0(A_i)$ (or $P_0(Z_i)$) could be directly comparable with experiments. Further, for ICF mechanism, P_0 is calculated via same procedure but for the reduced compound nucleus (see Fig. 2.3). Additionally, for nCN processes, the preformation factor is treated differently. Since, nCN processes such as DIC and QF strongly retain the memory of entrance channel, thus for such processes, P_0 is considered unity and is distributed equally among the most probable target and projectile like fragments (observed in fragment mass distribution). A schematic diagram presenting the formalism of DCM for ICF and nCN mechanisms is presented in Fig. 2.3.

2.6 Penetration Probability P

Penetration probability P (referring to R-motion) is an essential ingredient to understand the nuclear dynamics and can be calculated using the WKB approximation [47]. The expression of penetrability P for the decay of compound system is given as

$$P = exp[-\frac{2}{\hbar}\int_{R_a}^{R_b}\{2\mu[V(R) - Q_{eff}]\}^{1/2}dR] \tag{2.38}$$

The limits of integral from R_a to R_b signify that the penetration of fragment through the interaction barrier starts at R_a (first turning point) and terminates at R_b (see Fig. 2.4). Q_{eff} represents the effective Q-value of the decay process. V(R) is the scattering potential and for each η-value in excited state decay, it is calculated as follows:

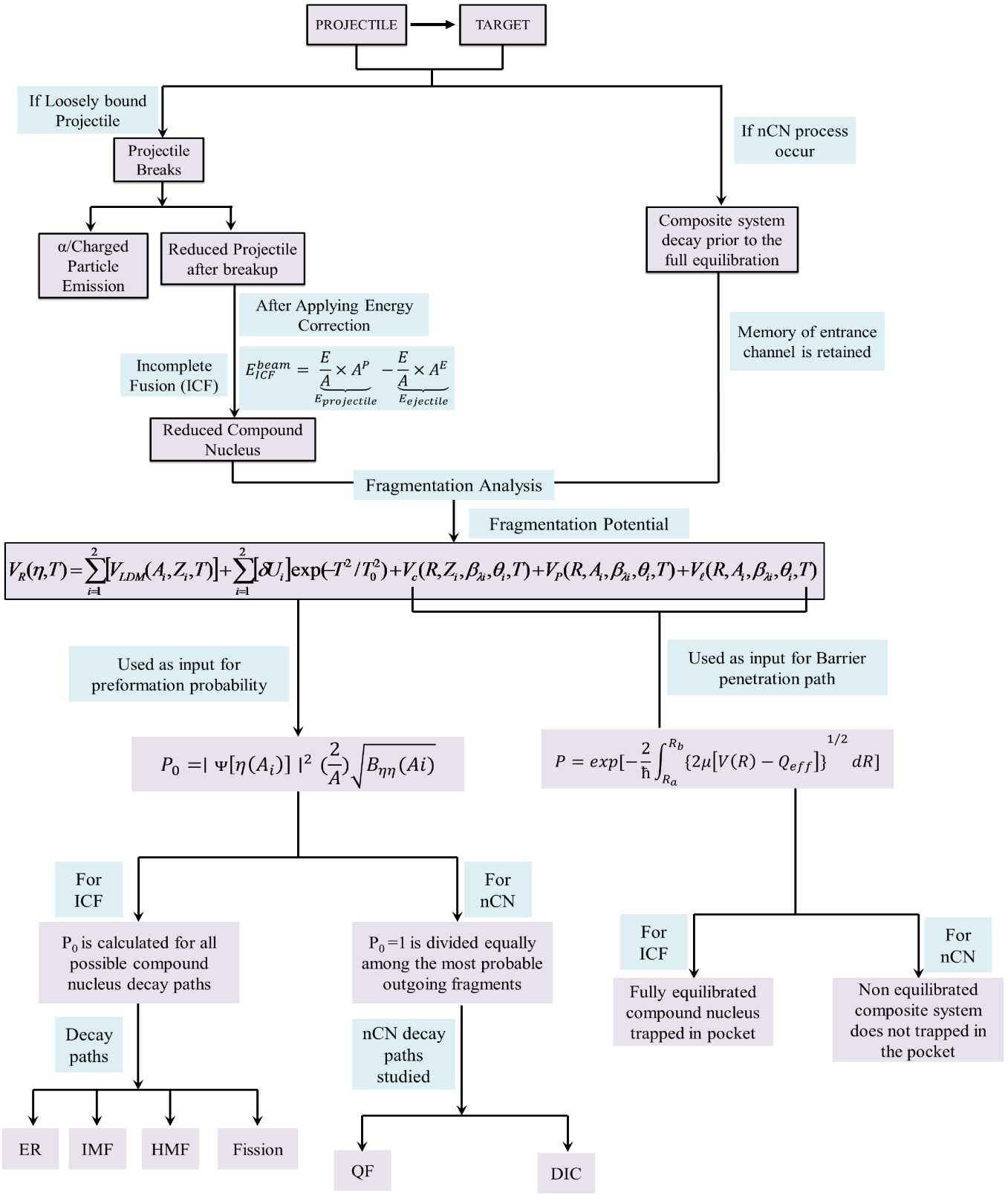

Figure 2.3 A Schematic diagram presenting the formalism of dynamical cluster-decay model for ICF and nCN processes.

$$V(R,\ell,T) = V_c(R,Z_i,\beta_{\lambda i},\theta_i,\phi,T) + V_p(R,A_i,\beta_{\lambda i},\theta_i,\phi,T) + V_\ell(R,A_i,\beta_{\lambda i},\theta_i,\phi,T) \quad (2.39)$$

where, V_C, V_P and V_ℓ are the Coulomb (Eq. (2.22)), proximity (Eq. (2.28)) and centrifugal potential (Eq. (2.32)) respectively. Since in DCM, the single penetration path is adopted (see Fig. 2.4), thus the scattering potential (at inner (R_a) and outer (R_b) radii) for the decay of hot and rotating compound system with total excitation energy TXE of decaying fragments, satisfy the condition given as follows

$$V(R_a,\ell) = V(R_b,\ell) = Q_{eff}(T) = TKE(T) \quad (2.40)$$

Next, the inner radius or the first turning point R_a is given as

$$R_a = R_1(\alpha_1,T) + R_2(\alpha_2,T) + \Delta R(T) = R_t(\alpha,T) + \Delta R(T). \quad (2.41)$$

where, the radius vector R_i can be seen in Eq. (2.17), and $\Delta R(T)$ is the neck-length parameter that incorporates the neck formation effects and allow us to define the barrier lowering (ΔV_B) effect in DCM. Both ΔR and ΔV_B are discussed in the following Section.

2.7 Neck length parameter (ΔR) and barrier lowering property of DCM

The neck formation is one of the essential degrees of freedom in nuclear dynamics. During the fragmentation of compound system, the ways of evolving a neck play a vital role in characterizing the decay outcomes such as mass, charge, and kinetic energy of outgoing fragments. In DCM, following the TCSM, the neck formation effects are consolidated through neck length parameter (ΔR) [43, 48, 49], which is alike to that used in both the

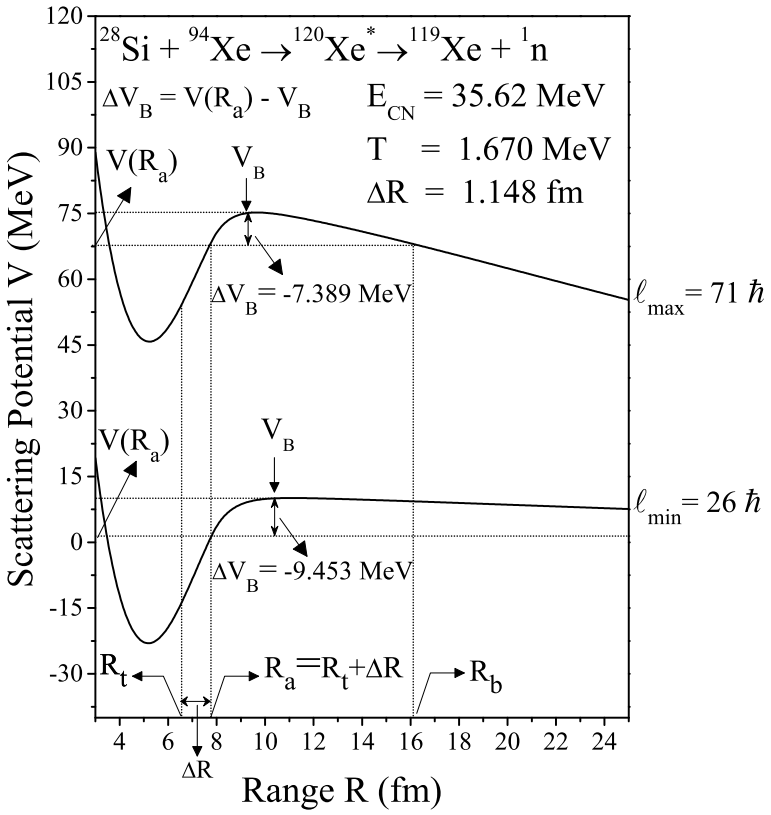

Figure 2.4 The variation of scattering potential as a function of range R for the decay of $^{120}Xe^{*}$ system.

scission-point [50] and saddle-point [51,52] statistical fission models. The optimization of ΔR for the best fit of experimental data enables us to interpret the first turning point (R_a)(Eq. (2.41)) of the barrier penetration (referring to actually used barrier height) and thus introduce the index of barrier lowering (ΔV_B) in DCM (see Fig. 2.4). For each ℓ-value, ΔV_B represents the difference between V(R_a,ℓ) and $V_B(\ell)$ as follows

$$\Delta V_B(\ell) = V(R_a, \ell) - V_B(\ell). \tag{2.42}$$

where, V(R_a,ℓ) (actually used barrier) is the potential at first turning point, R_a and $V_B(\ell)$ is the barrier height. Note that ΔV_B is negative for all ℓ-values since the actually used barrier is effectively lowered. The magnitude of ΔV_B decreases with increase in angular momentum, ℓ (see Fig. 2.4) and energy (discussed in subsequent chapters). It is relevant to mention here that ΔV_B in DCM, works as an appropriate tool to explain the sub barrier fusion hindrance, which might occur due to the facts such as weakly or

halo nature of projectile, shell structure of projectile and target, or due to the presence of some competing direct or non-compound nucleus process. This in-built property of barrier lowering at sub barrier energies lowers the barrier without modifying the depth of potential pocket.

2.8 Decay Cross-sections and emission time of decaying fragments

In DCM, the decay cross sections are calculated by applying the partial wave analysis (PWA), which has proved to be one of the most acceptable methods to estimate the cross-sections theoretically. In this method, the partial contributing cross-sections can be further divided into other contributing parts, according to which one can define the total reaction cross-section (σ_R) as the sum of cross-sections contributing due to all possible processes. In DCM, by applying the PWA, the decoupled approximation to η- and R-motions is used to define the decay cross-sections as follow [1, 2]:

$$\sigma = \sum_{\ell=\ell_{min}}^{\ell_{max}} \sigma_\ell = \frac{\pi}{k^2} \sum_{\ell=\ell_{min}}^{\ell_{max}} (2\ell+1) P_0 P; \qquad k = \sqrt{\frac{2\mu E_{c.m.}}{\hbar^2}} \tag{2.43}$$

where, $\mu = [A_1 A_2/(A_1 + A_2)]m$ is the reduced mass, and ℓ_{min} and ℓ_{max} are the minimum and maximum angular momentum respectively. This ℓ-window may split in to two parts in the presence of deep inelastic collisions (a nCN process).

For CN process, the ℓ-window contributing towards decay is $0 \leq \ell \leq \ell_{cr}$ and for DIC, it is $\ell_{cr} \leq \ell \leq \ell_{gr}$ where, ℓ_{cr} represents critical angular momentum and ℓ_{gr} (ℓ_{max} for DIC) is grazing angular momentum. This approximation of angular momentum is similar to the sharp cut off approximation used in statistical-models which is found to give reasonable results with very small value of the width parameter $\Delta\ell$ (i.e. 1-2 $\hbar$) as shown in [51].

ℓ_{cr} is that (critical) value of angular momentum above which compound nucleus for-

mation is not possible and the expression for ℓ_{cr} is given as

$$\ell_c = R_a\sqrt{2\mu[E_{c.m.} - V(R_a, \eta_{in}, \ell = 0)]}/\hbar, \tag{2.44}$$

Next, the grazing angular momentum (ℓ_{gr}) is the limit of partial wave above ℓ_{cr}-value upto which there might be the contribution of some nCN (non compound nucleus) peripheral collisions. For current work, the values of ℓ_{gr} are calculated using equation no.(11) of [53] as shown below:

$$[\ell_{gr}(\ell_{gr}+1)]^{\frac{1}{2}} = 0.22R[\mu(E_{c.m.} - V_C)]^{\frac{1}{2}} \tag{2.45}$$

Here, μ, $E_{c.m.}$ and V_C represent reduced mass, center of mass energy and Coulomb energy respectively.

Besides an important input in the calculation of cross sections, P_0 and P also serve as an input to measure the emission time of decaying fragment in outgoing channel, which reads as:

$$\tau_{\frac{1}{2}} = \frac{ln2}{\lambda}, \quad \lambda = \nu_0 P_0 P \tag{2.46}$$

here, λ is decay constant and ν_0 is the impinging frequency calculated using:

$$\nu_0 = \frac{velocity(v)}{R_0} = \frac{(2E_2/\mu)^{\frac{1}{2}}}{R_0} \tag{2.47}$$

The R_0 used in above equation represents the radius of composite system and E_2=$\frac{1}{2}\mu v^2$ is the kinetic energy of the emitted fragments.

The results extracted through DCM calculations are discussed in the forthcoming chapters.

Bibliography

[1] R. K. Gupta, R. Kumar, N. K. Dhiman, M. Balasubraniam, W. Scheid, and C. Beck, Phys. Rev. C **68**, 014610 (2003).

[2] M. Balasubraniam, R. Kumar, R. K. Gupta, C. Beck, and W. Scheid, J. Phys. G **29**, 2703 (2003).

[3] B. B. Singh, M. K. Sharma, and R. K. Gupta, Phys. Rev. C **77**, 054613 (2008).

[4] R. K. Gupta, M. Balasubraniam, R. Kumar, D. Singh, and C. Beck, Nucl. Phys. A **738**, 479c (2004). R. K. Gupta, M. Balasubramaniam, R. Kumar, D. Singh, C. Beck, and W. Greiner, Phys. Rev. C **71**, 014601 (2005).

[5] B. B. Singh, M. K. Sharma, R. K. Gupta, and W. Greiner, Int. J. Mod. Phys. E **15**, 699 (2006).

[6] S. Kanwar, M. K. Sharma, B. B. Singh, R. K. Gupta, and W. Greiner, Int. J. Mod. Phys. E **18**, 1453 (2009). S. K. Arun, R. Kumar, and R. K. Gupta, J. Phys. G: Nucl. Part. Phys. **36**, 085105 (2009).

[7] M. K. Sharma, S. Kanwar, G. Sawhney, R. K. Gupta, and W. Greiner, J. Phys. G: Nucl. Part. Phys. **38**, 055104 (2011); D. Jain, R. Kumar, M. K. Sharma, and R. K. Gupta, Phys. Rev. C **85**, 024615 (2012).

[8] M. K. Sharma, G. Sawhney, R. K. Gupta, and W. Greiner, J. Phys. G: Nucl. Part. Phys. **38**, 105101 (2011). M. K. Sharma, G. Sawhney, S. Kanwar, and R. K. Gupta, Mod. Phys. Lett. A **25**, 2022 (2010).

[9] G. Sawhney and M. K. Sharma, Eur. Phys. J. A **48**, 57 (2012). M. K. Sharma, S. Kanwar, G. Sawhney, and R. K. Gupta, Phys. Rev. C **85**, 064602 (2012);G. Sawhney, R. Kumar, and M. K. Sharma Phys. Rev. C **86** (2012) 034613.

[10] M. Kaur and M. K. Sharma, Phys. Rev. C **85**, 054605 (2012). M. Kaur, M. K. Sharma and Raj K. Gupta, Phys. Rev. C **86**, 064610 (2012).

[11] M. Kaur and Manoj K. Sharma, International Conference On Recent Trends in Nuclear Physics-2012, published in AIP conf. proc. **1524**, pp.151-154 (2013).

[12] K. Sandhu, M. K. Sharma, and R. K. Gupta, Phys. Rev. C **85**, 024604 (2012). G. Kaur and M. K. Sharma, Nucl. Phys. A **884**, 36 (2012). G. Kaur and M. K. Sharma, Phys. Rev. C **87**, 044601 (2013).

[13] G. Kaur, N. Grover, K. Sandhu and M. K.Sharma Nucl. Phys. A **927**, 232 (2014).

[14] J. Maruhn and W. Greiner, Phys. Rev. Lett. **32**, 548 (1974).

[15] R. K. Gupta, W. Scheid, and W. Greiner, Phys. Rev. Lett. **35**, 353 (1975).

[16] H. J. Fink, W. Greiner, R. K. Gupta, S. Liran, J.H. Maruhn, W. Scheid, and O. Zohni, in Proceedings of Int. Conf. on Reaction between Complex Nuclei, Nashville, Vol. **II** (North-Holland Pub.Co.) p. 21 (1974).

[17] S. Yamaji, W. Scheid, H. J. Fink, and W. Greiner, Z. Phys. A **278**, 69 (1976); S. Yamaji, W. Scheid, H. J. Fink, and W. Greiner, J. Phys. G: Nucl. Phys. **2**, L189 (1976); S. Yamaji, K. H. Ziegenhain, H. J. Fink, W. Greiner, and W. Scheid, J. Phys. G: Nucl. Phys. **3**, 1283 (1977).

[18] R. K. Gupta, A. Săndulescu, and W. Greiner, Z. Naturforsch. **32a**, 704 (1977); R. K. Gupta, C. Pirvulescu, A. Săndulescu, and W. Greiner, Z. Phys. A **283**, 217 (1977); Sovt. J. Nucl. Phys. **28**, 160 (1978); R. K. Gupta, Z. Physik. A **281**, 159 (1977).

[19] A. Săndulescu, H. J. Lustig, J. Hahn, and W. Greiner, J. Phys. G: Nucl. Phys. **4**, L279 (1978); H. J. Lustig, J. A. Maruhn, and W. Greiner, J. Phys. G: Nucl. Phys. **6**, L25 (1980).

[20] A. Săndulescu, R. K. Gupta, W. Scheid, and W. Greiner, Phys. Lett. B **60**, 225 (1976). R. K. Gupta, A. Săndulescu, and W. Greiner, Phys. Lett. B **67**, 257 (1977); Rev. Roum. Phys. **23**, 51 (1978).

[21] R. K. Gupta, IANCAS Bull. (India), **6**, 2 (1990).

[22] V. M. Strutinsky, Nucl. Phys. A **95**, 420 (1967).

[23] H. Kröger and W. Scheid, J. Phys. G **6**, L85 (1980).

[24] K. J. LeCouteur and D. W. Lang, Nucl. Phys. **13**, 32 (1959).

[25] R. K. Gupta, N. Singh, and M. Manhas, Phys. Rev. C **70**, 034608 (2004).

[26] G. Audi, A. H. Wapstra and C. Thiboult, Nucl. Phys. A **729**, 337 (2003).

[27] P. Möller, J. R. Nix, W. D. Myers, and W. J. Swiatecki, At. Data Nucl. Data Tables **59**, 185 (1995).

[28] N. J. Davidson, S. S. Hsiao, J. Markram, H. G. Miller, and Y. Tzeng, Nucl. Phys. A **570**, 61c (1994).

[29] P. A. Seeger, Nucl. Phys. **25**, 1 (1961).

[30] S. DeBenedetti, Nuclear Interactions (New York: book Published by Wiley & Sons) (1964).

[31] G. Audi and A. H. Wapstra, Nucl. Phys. A **595**, 4 (1995).

[32] W. Myers and W. J. Swiatecki, Nucl. Phys. **81**, 1 (1966).

[33] M. Bansal, Raj Kumar, and Raj K. Gupta, Journal of Physics: Conference Series **321**, 012046 (2011).

[34] R. K. Gupta, S. K. Arun, R. Kumar, and Niyti, Int. Rev. Phys. (IREPHY) **2**, 369 (2008).

[35] R. K. Gupta, M. Balasubramaniam, R. Kumar, N. Singh, M. Manhas, and W. Greiner, J. Phys. G: Nucl. Part. Phys. C **31**, 631 (2005).

[36] M. Münchow, D. Hahn and W. Scheid, Nucl. Phys. A **388**, 381 (1982).

[37] M. J. Rhoades-Brown, V. E. Oberacker, M. Seiwert and W. Greiner, Z. Phys. A **310**, 287 (1983).

[38] C. Y. Wong, Phys. Rev. Lett. **31**, 766 (1973).

[39] Deryagin, Kolloid Z. **69**, 155 (1934).

[40] J. Blocki, J. Randrup, W. J. Swiatecki, and C. F. Tsang, Ann. Phys. (NY) **105**, 427 (1977).

[41] A. Gray, Modern Differential Geometry of Curves and Surfaces with Mathematica, 2nd Edition, CRC Press, Boca Raton, p.89 (1997).

[42] M. Seiwert, W. Greiner, V. Oberacker, and M.J. Rhoades-Brown, Phys. Rev. C **29**, 477 (1984).

[43] S. Kumar and R. K. Gupta, Phys. Rev. C **55**, 218 (1997).

[44] N. Malhotra and R. K. Gupta, Phys. Rev. C **31**, 1179 (1985).

[45] P. Glassel, R. S. Simon, R. M. Diamond, R. C. Jared, I. Y. Lee, L. G. Moretto,J. O. Newton, R. Schmitt and F. S. Stephens, Phys. Rev. Lett. **38**,7 (1977); L. G. Moretto and G. J. Wozniak Ann. Rev. Nucl. Part. Sci. **34**, 189-245 (1984).

[46] S. Kailas (private communication).

[47] G. Wentzel, Z. Phys. **38**, 518 (1926); H. A. Kramers, Z. Phys. **39**, 828 (1926); L. Brillouin, Compt. Rend. Hebd. Seances Acad. Sci. **183**, 24 (1926).

[48] H. S. Khosla, S. S. Malik, and R. K. Gupta, Nucl. Phys. A **513**, 115 (1990).

[49] R. K. Gupta, S. Kumar, and W. Scheid, Int. J. Mod. Phys. E **6**, 259 (1997).

[50] T. Matsuse, C. Beck, R. Nouicer, and D. Mahboub, Phys. Rev. C **55**, 1380 (1997).

[51] S. J. Sanders, D. G. Kovar, B. B. Back, C. Beck, D. J. Henderson, R. V. F. Janssens, T. F. Wang, and B. D. Wilkins, Phys. Rev. C **40**, 2091 (1989).

[52] S. J. Sanders, Phys. Rev. C **44**, 2676 (1991).

[53] H. V. Klapdor, H. Reiss and G. Rosner, Nucl. Phys. A **262**, 157-188 (1976).

Chapter 3

Decay of Xe-isotopes formed in reactions induced via ^{28}Si projectile

3.1 Introduction

During last few decades, extensive amount of research has been carried out to explore the heavy-ion reactions (HIRs), as they form a promising tool in understanding nuclear structure and associated reaction dynamics. Besides this, another reason of exploring such reactions is to attain new elements/isotopes using heavy ion beams and hence widen the scope of existing periodic table. However, despite of vigorous research carried out in this domain, numerous queries still persist which drive us to deeply explore the behavior of nuclei involved in heavy ion reactions and to interpret the exotic nuclear phenomena exhibited by them. Consequently, one seeks to examine various factors which play a crucial role in studying the dynamics of such reactions and with continuous attempts, it has been endowed that the nature of projectile and target nuclei are of significant importance to address the overall description of nuclear behavior involved. Apparently, in recent years with subsequent advancement in technology, the exploration of such reactions has been considerably influenced due to the availability of heavy-ion accelerators capable of providing heavy projectile beams involving wide range of incident energy. Hence, the

dynamics of reactions involving heavy ion beams incident on different target nuclei provide an unambiguous tool for further understanding in this direction. It is noteworthy that the properties of nuclei may vary drastically with the addition or removal of each nucleon and hence the decay analysis of nuclear isotopes is of huge relevance and importance.

In view of this, the present chapter aims at addressing the decay cross-sections of Xe isotopes formed in heavy ion reactions. In context to the experimental findings [1, 2], the decay profiles of the ^{118,120,122}Xe nuclei formed via asymmetric reactions, ^{28}Si+^{90,92,94}Zr, have been examined using the dynamical cluster-decay model (DCM) [3–12]. The cross-sections have been calculated over an extensive range of center of mass energy ($E_{c.m.}$) varying from 63.3-93.5 MeV. The Xe isotopes studied here are of considerable interest, because in one of the previous work using DCM, the dynamics of ^{112}Xe* formed in nearly symmetric reaction, i.e ^{58}Ni+^{54}Fe was examined at relatively higher energies [13]. Hence it was of extreme interest to understand the dynamics of various isotopes of Xe formed via asymmetric reaction partners over a varied range of incident energies. Also, it may be noted that ^{28}Si beam is a stable projectile beam having N=Z and the target nucleus, Zr is semi-magic with respect to the number of protons, specifically the ^{90}Zr nucleus has closed neutron shell (N=50). As employed for many other nuclei, the statistical approach has also been used to study the behavior of Xe nucleus formed in different heavy ion reactions and certain discrepancies between the predictions of statistical models and the experimental studies have been observed [14].

In the present work, an endeavour has been made to carry out systematic decay analysis of Xe isotopes in framework of DCM. Evidently, in heavy ion reactions (involving projectiles heavier than alpha particles), the deformations are found to play an important role and such effects are analyzed here in context of the dynamics of Xe isotopes. In order to examine the role of deformations, the decay patterns have been examined for spherical fragmentation as well as with the incorporation of quadrupole (β_{2i}) and hexdecapole (β_{2i-4i})-deformation within optimum and compact orientation approach respectively. Additionally, the role of excitation energy (or temperature), is investigated to understand

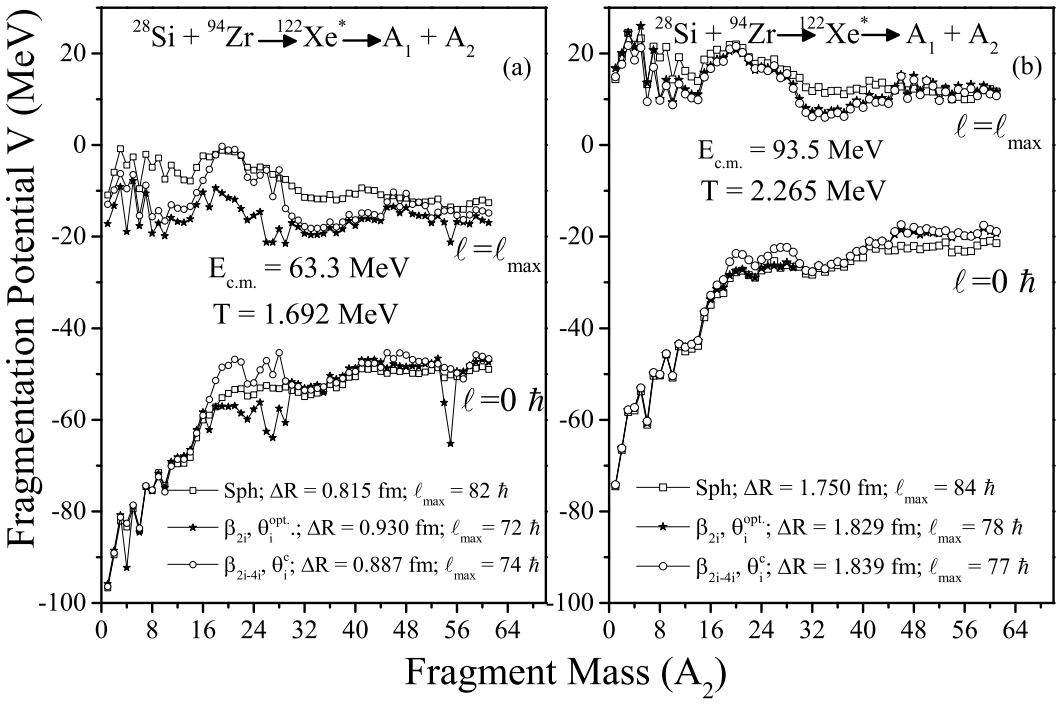

Figure 3.1 Fragmentation potential as a function of fragment Mass (A_2) for the decay of ^{122}Xe* nucleus at (a) $E_{c.m.}$ = 63.3 MeV and (b) $E_{c.m.}$ = 93.5 MeV, plotted for spherical, $\beta_{2i}^{opt.}$ (static-β_{2i} with optimum orientations) and β_{2i-4i}, θ_i^c (static-β_{2i-4i} with compact orientations) deformed choice of fragments.

the dynamics of ^{28}Si + ^{90,92,94}Zr reaction. Also, the isotopic dependence (N/Z ratio) of decay fragments has been explored for ^{118,120,122}Xe* nuclei. Moreover, the role of projectile mass has been examined by carrying out the comparative analysis of decay paths of ^{118}Xe* and ^{123}Ba* nuclei at common energy ($E_{c.m}$=75 MeV). The decay cross sections are also predicted at extreme energies for ^{118,120}Xe* isotopes and for neighboring ^{116,124}Xe* isotope at four common energies, $E_{c.m.}$=72, 73, 75 and 76 MeV. This work is published in [15].

The present chapter is arranged as follows. The calculations and results obtained are presented in Sec. 3.2. The conclusions drawn are summarized in Sec. 3.3.

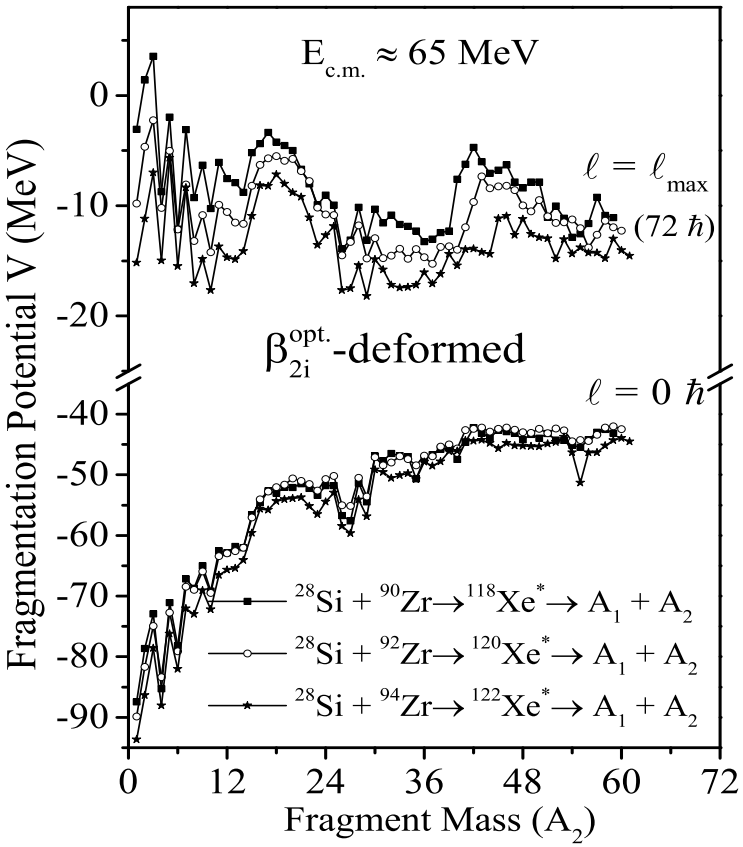

Figure 3.2 The effect of isospin (N/Z ratio) and angular momentum studied through variation of potential energy surfaces as a function of fragment mass at common center of mass energy, $E_{c.m.}$=65 MeV for $\beta_{2i}^{opt.}$-deformed (static-β_{2i} with optimum orientations) choice.

3.2 Calculations and Results

In this section, the decay study of the ^{118,120,122}Xe* nuclei, formed in the ^{28}Si+^{90,92,94}Zr reactions is discussed over a wide span of center-of-mass energy varying from $E_{c.m.}$= 63.3 - 93.5 MeV, which covers both sides of Coulomb barrier. The fusion cross sections under study are noticed to have a contribution from evaporation residue (ER; A≤4) alone, while the fission contribution is negligible. Initially, an attempt is made to investigate the influence of deformations on the decay of Xe isotopes formed in Si induced reaction. Also, the relative fragmentation behavior of three isotopes of Xe is discussed besides making some predictions for future verification. It has been observed that the effect of

deformation is prominent for the heaviest isotope under study, i.e. $^{122}Xe^{*}$ as it shows shape transition from prolate to oblate [16]. In view of this, the role of deformations is studied for $^{28}Si+^{94}Zr$ reaction using the (i) spherical fragmentation, (ii) quadrupole deformations (β_{2i}) within the optimum orientation approach [17] and (iii) deformation effects up to the hexadecapole (β_{2i-4i}) with the compact orientation approach [18].

Fig. 3.1 depicts the fragmentation potential plotted as a function of fragment mass (A_2) for extreme values of angular momentum at the lowest and highest energies. It is worth mentioning that the fragmentation potential works as an essential input in the Schrodinger wave equation to calculate the preformation probability and hence the decay cross-sections. From Fig. 3.1(a), it is observed that at minimum ℓ-value, except for some intermediate mass fragments (IMF; $5 \leq A \leq 20$) and heavy mass fragments (HMF), the structure of fragmentation potential is almost identical for all three choices of fragments and their magnitude almost fold over each other. However, the variation of potential energy surface attained at $\ell = \ell_{max}$ indicates that, the effect of deformation depends upon the associated angular momentum. On comparing the fragmentation path attained at higher ℓ-values, it is observed that for the quadrupole deformed approach, the magnitude of fragmentation potential is lower for all the contributing fragments as compared to that for the spherical approach. Evidently, apart from few IMFs and HMFs fragments, the fragmentation potential for hexadecapole (β_{2i-4i}) deformation overlays that of quadrupole deformation. Further, analyzing the variation of fragmentation potential plotted in Fig. 3.1(b), it is observed that at higher energy, i.e. $E_{c.m.}$=93.5 MeV, the fragmentation potential is higher in magnitude as compared to lower energy. In other words, with increase in energy, the magnitude of fragmentation potential also increases. On the other hand, the difference in magnitude of fragmentation potential for all three approaches is very small. Also, it is observed that after incorporating the quadrupole and hexadecapole deformations, the change in structure appears at lowest energy in form of minor fluctuations in the IMF and HMF region and starts disappearing with increase in energy. However, at both the energies, the overall structure of fragmentation potential is

near symmetric. It is worth noting that in DCM, the minimum fragmentation potential signifies the maximum preformation probability (P_0) and hence represents the most favorable decay mode. In view of this, the results ahead have been discussed by considering quadrupole deformed approach, as contribution of higher multipole deformations is not very significant for considered reactions.

After investigating the deformation and angular momentum effects for ^{122}Xe* nucleus, the dynamics involved in the decay of three different isotopes of Xe, i.e ^{118,120,122}Xe* is analysed. To examine the effect of isospin (N/Z-ratio), the fragmentation potential and mass distribution of ^{28}Si+^{90}Zr, ^{28}Si+^{92}Zr, and ^{28}Si+^{94}Zr reactions is analyzed at comparable center of mass energies, $E_{c.m.} \sim$ 65.0 and 89.0 MeV. Fig. 3.2 depicts the variation of fragmentation potential V (A_2) as a function of light fragment mass for all the three systems at extreme ℓ-values and lowest center of mass energy ($E_{c.m.} \sim$ 65.0) in reference to [1]. From the figure, it is noticed that the behavior of fragments is different at extreme ℓ-values. Moreover, this figure emphasizes that light particles are preformed strongly at lower ℓ-values whereas, fission fragments starts approaching at higher ℓ-values. At lower ℓ, it is observed that there is marginal difference in the magnitude of fragmentation path while going from ^{118}Xe* to ^{120}Xe* and ^{122}Xe*, however, the same gets wider at higher angular momentum. The magnitude of potential energy surface at ℓ=ℓ_{max} is slightly higher for the lightest isotope, ^{118}Xe* and decreases with addition of neutrons, being minimum for ^{122}Xe*. This trend of fragmentation potential observed for isotopes of Xe is found to be almost similar to that obtained for isotopes of neighboring Ba nucleus [19]. The minimum magnitude of fragmentation potential for ^{122}Xe* signifies that amongst all three isotopes, the decay probability is relatively more for the ^{122}Xe* as compared to ^{118}Xe*. This behavior may be attributed to the presence of ^{90}Zr* target nucleus (semi-magic, Z=40 and neutron magic, N=50) as compared to semi magic target nucleus, ^{94}Zr* (Z=40). The effect of shell closure and the presence of deformed target nucleus has also been observed earlier for the ^{150,158}Tb* nuclei [20]. To further analyze the effect of isospin (N/Z ratio), the mass distribution for these nuclei is plotted in Fig.

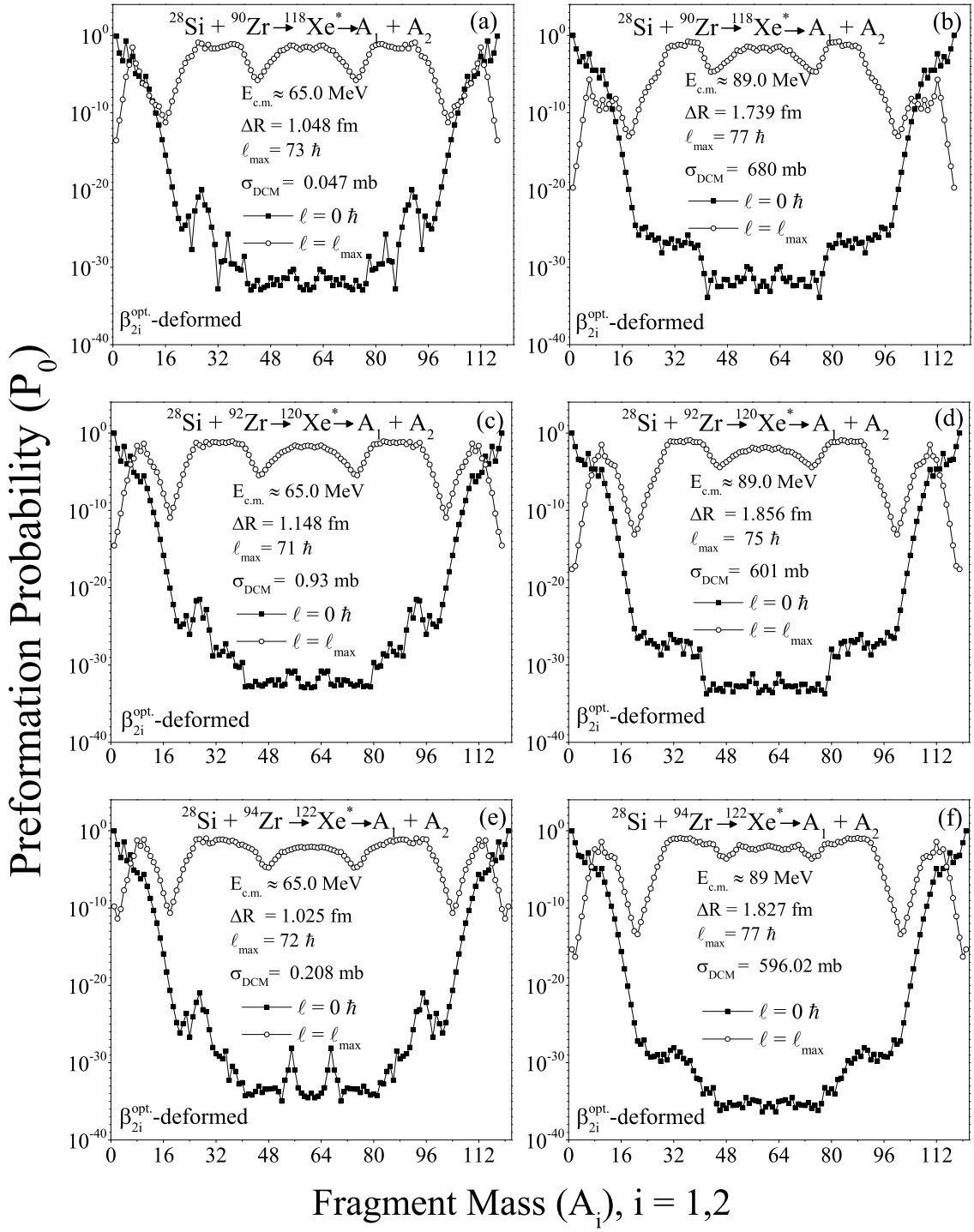

Figure 3.3 The mass distribution of the fragments for the decay of (a,b) ^{118}Xe*, (c,d)^{120}Xe*, (e,f) ^{122}Xe* nuclei for the use of $\beta_{2i}^{opt.}$-deformed (static-β_{2i} with optimum orientations) and at extreme ℓ-values.

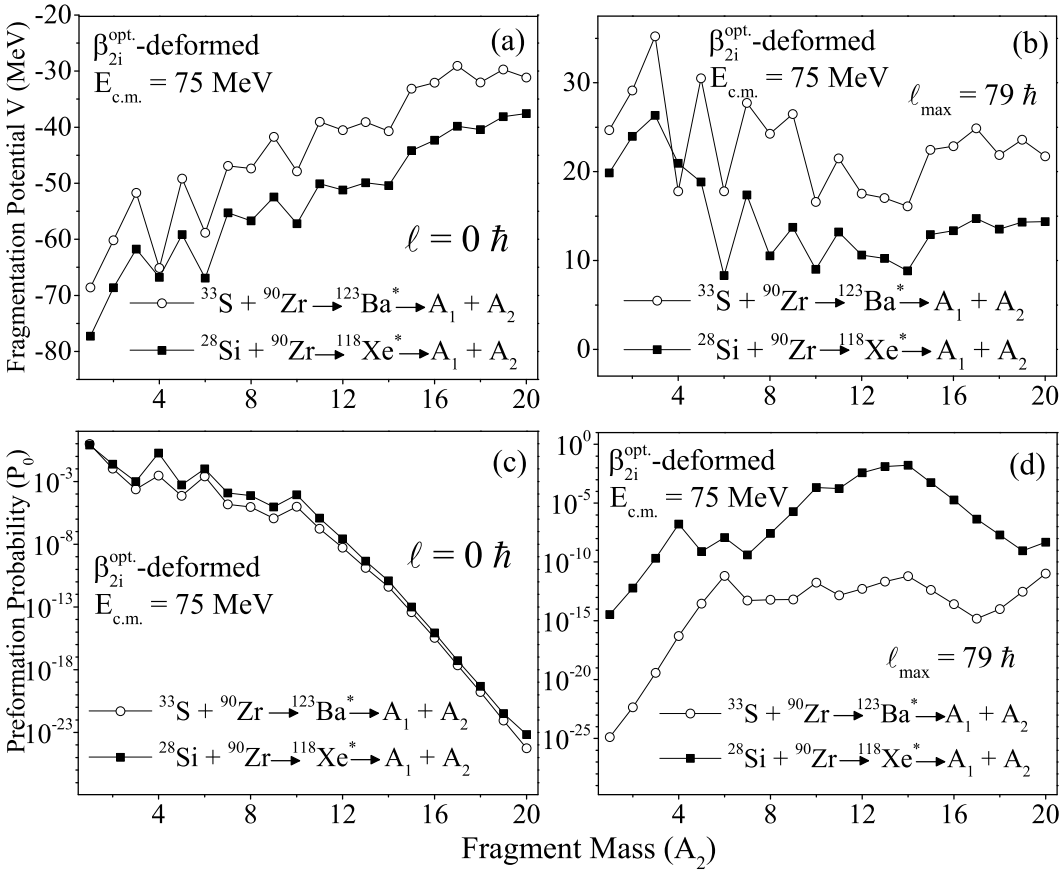

Figure 3.4 The variation of (a,b) fragmentation potential, (c,d) Preformation probability as a function of fragment mass (A_2) for ^{123}Ba* and ^{118}Xe* nuclei plotted at $E_{c.m}\sim$75 MeV for the use of $\beta_{2i}^{opt.}$-deformed (static-β_{2i} with optimum orientations) choice of fragmentation.

3.3, where the role of shell closure and isospin of the decaying Xe compound systems is examined.

Fig. 3.3, illustrates the variation of preformation probability P_0 as a function of fragment mass A_i (i=1,2 stand for heavy and light fragments), for ^{118,120,122}Xe* nuclei at two comparable energies, $E_{c.m.} \sim$ 65.0 and 89.0 MeV, plotted for extreme ℓ-values. At both energies and extreme ℓ, the magnitude of preformation probability is highest for ^{122}Xe* nucleus and is lowest for ^{118}Xe*. This observation is harmonious with that obtained earlier for the variation of fragmentation potential. At higher ℓ-value, although the magnitude is different, yet the mass distribution is near symmetric for all Xe isotopes. Hence, it may be said that independent of the mass of compound nucleus and the energy involved, the fragment mass distribution is found to be near symmetric for all three nuclei. Evidently, at highest energy the region of symmetric distribution is slightly pronounced for the heav-

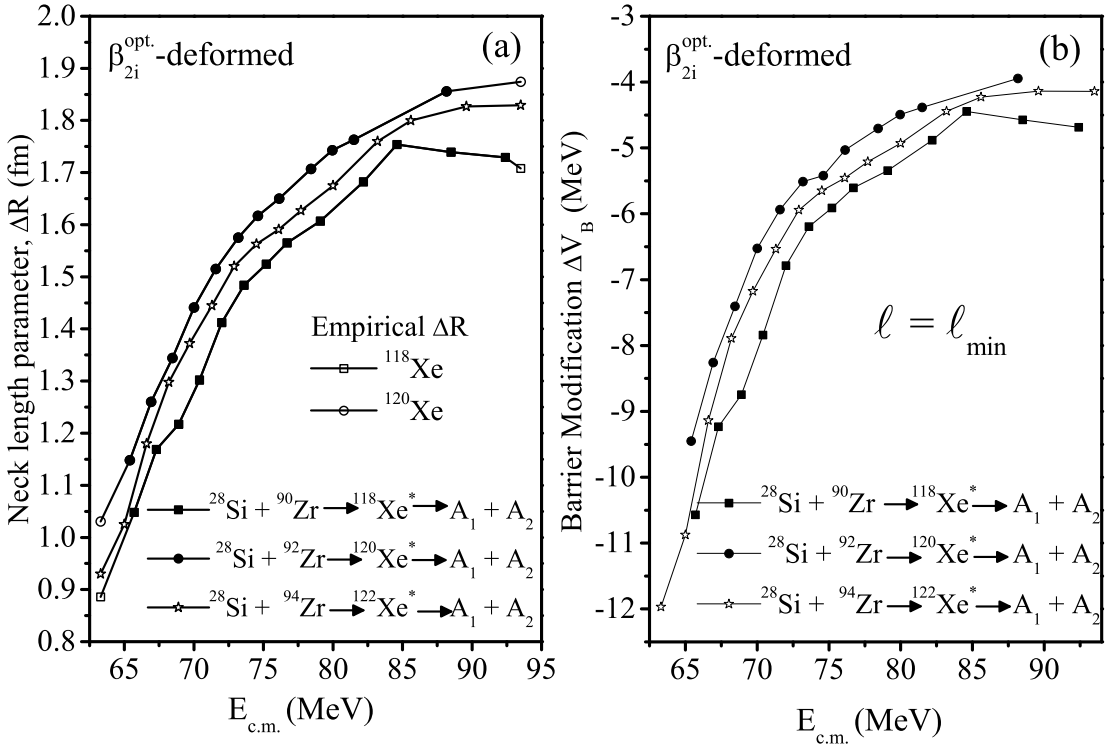

Figure 3.5 Variation of (a) neck length parameter (ΔR) (b) barrier modification (ΔV_B) plotted for minimum ℓ-value as a function of center of mass energy ($E_{c.m.}$) for the decay of three isotopes ^{118,120,122}Xe* for $\beta_{2i}^{opt.}$-deformed (static-β_{2i} with optimum orientations) approach.

iest isotope, ^{122}Xe* as compared to ^{118}Xe* nucleus. Further, at lower angular momentum, a substantial change in fragment distribution is noticed on going from minimum to maximum energy. In Fig. 3.3, showing the mass distribution obtained at ℓ=0$\hbar$, on comparing panel (a,c,e) with panel (b,d,f), it is observed that at lower ℓ, for each isotope, prominent peak is evident around A_1∼90, which eventually diminish or vanish on increasing the center of mass energy from $E_{c.m.}$= 65.0 to 89.0 MeV. However, no such peaks occur at higher angular momentum. A deep insight of panel (a,c,e) of Fig. 3.3 reveals that the fine structure effects obtained around A_1=90,92,94 and complementary light mass fragments are the most prominent for the ^{118}Xe* isotope. The presence of these peaks may be attributed to the presence of shell closure effect. Specifically, the fluctuations around A_1= 90, 92, 94 for ^{118}Xe*, ^{120}Xe* and ^{122}Xe* nuclei respectively, seem to signify the role of shell effects in dynamics of reaction under consideration. For ^{118}Xe*, the peak around A_1= 90

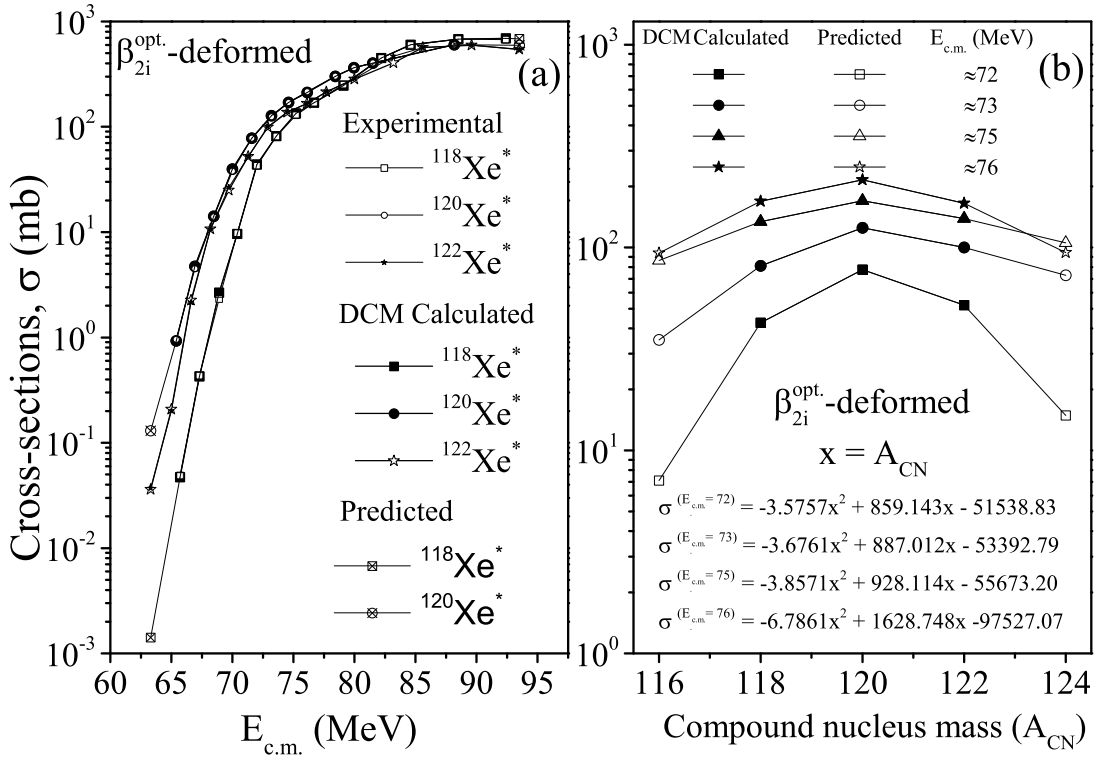

Figure 3.6 (a) DCM calculated evaporation residue (ER) decay cross-sections for ^{118,120,122}Xe* isotope, plotted as a function of center of mass energy ($E_{c.m.}$) compared with experimental data [1, 2], Also shown are the predicted cross sections for ^{118,120}Xe* isotopes at extreme energies (open crossed square and open crossed circle)(b) The cross sections predicted for ^{116}Xe and ^{124}Xe isotope by using the calculated cross sections attained at four common energies.

originates due to the presence of ^{90}Zr target nucleus having neutron shell closure N=50. Similarly, the peaks attained at A_1= 92, 94 may be associated to ^{92,94}Zr target nucleus, which are semi-magic due to proton number, Z=40. Thus, it may be said that the shell effects (magic shells) are noticed to play a crucial role in the fragment mass distribution for ^{28}Si+^{90,92,94}Zr reactions at lower energies and angular momentum. On the other hand, no such preformed peaks are observed at higher energy and angular momentum. It is pertinent to inscribe here that in the earlier work [21], similar effects were observed in the decay of ^{202}Pb* where, the appearance of such asymmetric peak was related with the likelihood of some competing mechanism.

So far, the role of deformations and related orientations degree of freedom has been

examined in context of ^{122}Xe*. Besides this, the effect of iso-spin on the dynamics of even mass Xe isotopes has been explored by carrying out comparative analysis of all three nuclei, i.e. ^{118,120,122}Xe*. Also, the shell closure effect and the role of magic and semi-magic target nuclei are addressed so far. Pursuing the study further, it is aimed to examine the role of projectile nucleus by carrying out comparative study of ^{28}Si+^{90}Zr$\rightarrow$^{118}Xe$^{*}\rightarrow$ A$_1$+ A$_2$ and ^{33}S+^{90}Zr$\rightarrow$^{123}Ba$^{*}\rightarrow$ A$_1$+ A$_2$ reactions at a common center-of mass energy $E_{c.m.}$ $\sim$ 75 MeV. The ER cross-sections for ^{123}Ba* nucleus have been calculated in context to experimental data of L. Corradi *et.al.* [22]. The comparative study of ^{118}Xe* and ^{123}Ba* nuclei may reveal some interesting aspects, so far as the dynamics of these reactions is concerned. Figs.3.4 (a,b) depict the fragmentation potential at extreme ℓ- values respectively, while Figs.3.4 (c,d) show the preformation probability plotted at both ℓ, explicitly for the light particles and intermediate mass fragments for the use of quadruple deformed approach at $E_{c.m.}$=75 MeV. From Figs.3.4 (a,b), it is observed that for ^{118}Xe* and ^{123}Ba* nuclei, at both ℓ-values, the alpha cluster structure is prominent for light mass fragments but tends to diminish with increase in mass. Similar results were also noticed earlier in the study involving neutron deficient Xe and Ba nuclei [19, 23]. Further analysis of ℓ-dependence is carried out in Figs.3.4 (c,d) which shows the preformation probability P_0 as a function of fragment mass. At lower angular momentum, corresponding to increasing fragmentation, the probability of fragments is found to decrease with increase in mass. This further confirms the fact that, at lower ℓ, the light particles have maximum contribution towards the decay cross-sections.

Next, for an extensive analysis of the decay profiles of all the three ^{118,120,122}Xe* isotopes, the ER decay cross sections are estimated in the framework of DCM. Fig. 3.5(a) shows the variation of neck-length parameter as a function of center of mass energy, ranging from $E_{c.m.}$ = 63.3 to 93.5 MeV across the barrier. The ER decay cross-sections are estimated by optimizing the neck-length parameter ΔR, that possibly gives a measure of the time-scale at which the reaction occur. It is noticed that, ΔR increases with increase of center of mass energy, being highest for ^{120}Xe* and lowest for ^{118}Xe*. Note that dif-

ferent ΔR's for the isotopes mean that they evolve differently, subject to the nature of dynamics of compound nucleus formed. The magnitude of ΔR is lowest for the lightest nucleus ^{118}Xe*, which indicate that ER emission occurs relatively at later instant for this isotope formed in the reaction involving magic target ^{90}Zr having neutron shell closure (N=50), as compared to the heavier isotopes ^{120,122}Xe*, which are formed using the semi magic target nuclei (^{90,92}Zr). This observation is consistent with those drawn from Fig. 3.2 and Fig. 3.3, which illustrates that due to the presence of spherical shell closure at ^{90}Zr nucleus, decay probability of ^{118}Xe* is least as compared to ^{120,122}Xe*. Also, two extreme ($E_{c.m.}$ = 63.3 and 93.5 MeV) center of mass energies given for ^{122}Xe* nucleus are used as reference here to estimate the evaporation residue path of ^{118,120}Xe* nuclei and hence to predict the cross-sections at these extreme energies as depicted in Fig. 3.6(a) ahead.

Interestingly, the concurrence of DCM calculations with the experimental data at below barrier energies is related with the barrier modification or barrier lowering effect which is an in-built property of DCM, that enters through neck-length parameter ΔR. Thus, to extend this analysis, ΔV_B is plotted for the 1n decay channel of ^{118,120,122}Xe* isotopes for the deformed choice of fragments in Fig. 3.5(b). This figure clearly shows that at a given energy, the ΔV_B is least for ^{120}Xe* followed by ^{122}Xe* and ^{118}Xe* and thus follows a trend similar to that observed for the variation of ΔR for all three isotopes. Apparently, no direct influence of isospin (N/Z ratio) is noticed. This might be due the fact that experiments for ^{120}Xe* and ^{118,122}Xe* nuclei were executed independently and possess different magnitude of cross sections. It is noticed that the magnitude of ΔV_B decreases with increase in center of mass energy. Hence, one may say that large barrier modification is required at lower energies, which in-turn accounts for the fair concurrence of DCM based results with experimental data.

Table 3.1 The evaporation residue (ER) decay cross-sections of ^{118,120,122}Xe* nuclei formed in ^{28}Si + ^{90,92,94}Zr reactions calculated using DCM for quadrupole (β_{2i}; i=1, 2) deformed choice of fragments at given energie span, compared with the experimental data [1, 2]. Also, the angular momentum and neck length parameter values are inscribed.

	^{118}Xe*					^{120}Xe*					^{122}Xe*				
S. No.	$E_{c.m.}$ (MeV)	ℓ_{max} ($\hbar$)	ΔR (fm)	σ_{DCM} (mb)	$\sigma_{Exp.}$ (mb)	$E_{c.m.}$ (MeV)	ℓ_{max} ($\hbar$)	ΔR (fm)	σ_{DCM} (mb)	$\sigma_{Exp.}$ (mb)	$E_{c.m.}$ (MeV)	ℓ_{max} ($\hbar$)	ΔR (fm)	σ_{DCM} (mb)	$\sigma_{Exp.}$ (mb)
1	63.3	73	0.880	0.001	–	63.3	71	1.030	0.130	–	63.3	72	0.930	0.033	0.037
2	65.7	73	1.048	0.047	0.049	65.4	71	1.148	0.930	0.960	65.0	72	1.025	0.208	0.201
3	67.3	74	1.169	0.427	0.435	66.9	71	1.260	4.740	4.490	66.6	72	1.180	2.257	2.160
4	68.9	75	1.217	2.660	2.317	68.4	71	1.344	14.14	14.00	68.2	75	1.298	10.67	10.70
5	70.4	75	1.302	9.604	9.770	70.0	72	1.441	39.77	38.00	69.7	75	1.372	24.92	26.57
6	72.0	75	1.412	43.90	42.60	71.5	74	1.515	77.89	77.80	71.3	76	1.445	52.12	52.07
7	73.6	76	1.484	83.60	81.18	73.1	74	1.575	127.2	125.0	72.9	76	1.520	99.10	100.2
8	75.2	76	1.524	134.0	129.2	74.6	74	1.617	170.2	170.0	74.5	76	1.563	136.9	138.8
9	76.7	76	1.565	169.9	169.1	76.1	74	1.650	212.0	216.0	76.1	76	1.591	166.3	165.4
10	79.1	76	1.607	246.5	251.5	78.4	74	1.707	301.9	302.0	77.7	76	1.627	214.6	216.0
11	82.2	76	1.682	450.5	450.3	79.9	74	1.743	364.8	365.0	80.0	77	1.675	283.2	285.6
12	84.6	76	1.754	600.1	599.0	81.5	74	1.763	401.8	404.0	83.2	77	1.760	464.0	467.7
13	88.5	77	1.739	680.0	680.1	88.2	75	1.856	601.0	603.0	85.6	77	1.800	564.8	565.0
14	92.4	77	1.729	690.0	674.3	–	–	–	–	–	89.6	77	1.827	596.0	599.2
15	93.5	75	1.698	600.0	–	93.5	75	1.874	595.2	–	93.5	78	1.829	545.0	542.0

In Fig. 3.6(a), the value of calculated ER decay cross sections for ^{118,120,122}Xe isotopes (filled symbols) has been plotted as a function of center of mass energy. Evidently, the cross sections at given energy range are minimum for ^{118}Xe* and maximum for ^{120}Xe* while those of ^{122}Xe* lie in between. The cross sections for these nuclei are also tabulated in Table 3.1. This table clearly reveals that the DCM calculated cross-sections find nice agreement with the experimental data at all given energies. It can also be seen from Table 3.1 that the ΔR as well as ℓ_{max}-value increase with an increase in the energy. Further, Fig. 3.6(b) illustrates the variation of cross sections for ^{118,120,122}Xe at four common center of mass energies i.e. $E_{c.m} \sim 72$, 73, 75 and 76 MeV. Following the trend at these energies, the ER decay cross sections for the neighboring isotopes, ^{116}Xe* and ^{124}Xe* (open symbols) have been obtained through polynomial fitting (equation shown in Fig. 3.6(b)), which may be verified in future experiments.

3.3 Summary

In summary, the ER decay cross-sections of ^{118,120,122}Xe* are studied. Initially, the influence of deformations is examined for ^{122}Xe* by studying the behavior of fragmentation potential at two extreme energies. It has been observed that the barrier characteristics and potential energy surfaces get influenced with the incorporation of quadrupole deformations (β_{2i}) and hexadecapole (β_{2i-4i}) deformations. This effect of deformations is relatively more significant at lower energy as compare to higher energies. Further, the isotopic analysis has been carried out for ^{118,120,122}Xe* isotope by examining the variation of fragmentation potential and preformation probability (P_0) at two comparable energies ($E_{c.m} \sim 65.0$ and 89.0 MeV). The behavior of potential energy surfaces reveals that the ER decay probability is more for ^{122}Xe* formed through ^{28}Si + ^{94}Zr as its fragmentation potential possess least magnitude as compare to ^{118}Xe*. This may be attributed to the presence of spherical magic target nucleus (^{90}Zr) having neutron shell closure (N=50). The mass distribution is found to be near symmetric for all isotopes. Additionally, the

role of projectile beam has been examined in context to $^{118}Xe^{*}$ and $^{123}Ba^{*}$ nuclei by changing the projectile ^{28}Si with ^{33}S. It is observed that for either of the nuclei, the light fragments are more favored at minimum ℓ-value and the effect of projectile is nearly congruent for the ER decay study. The neck length parameter used to fit the ER decay cross section is found to increase with increase in energy and hence barrier lowering parameter decreases with increase in energy which show that lesser barrier modification is required at higher energies which in turn accounts for the fair agreement with the experimental data. Finally, the cross-sections for $^{118,120}Xe^{*}$ isotopes have also been predicted at extreme energies, $E_{c.m.}$=63.3 and 93.5 MeV using the DCM. In addition to this prediction, the cross sections for neighboring isotopes of Xe i.e. $^{116,124}Xe^{*}$ are predicted at four (nearly common) center of mass energies, which may be verified by future experiments.

After analyzing the decay mechanisms of compound nuclei formed using the tightly bound projectile(s) involving complete fusion process, it will be of further interest to examine the CN decay for the reactions comprising of loosely bound projectiles. The dynamics of such reactions and thus the comparative analysis of complete fusion (CF) and incomplete fusion (ICF) components is presented in the next chapter.

Bibliography

[1] S. Kalkal, S. Mandal, N. Madhavan et. al. Phys. Rev. C **81**, 044610 (2010).

[2] J. O. Newton, C. R. Morton, M. Dasgupta et. al. Phys. Rev. C **64**, 064608 (2001).

[3] R. K. Gupta, M. Balasubramaniam, R. Kumar, D. Singh, C. Beck, Nucl. Phys. A **738**, 479 (2004).

[4] R. K. Gupta, S. K. Arun, R. Kumar, and M. Bansal, Nucl. Phys. A **834**, 176c (2010).

[5] M. Kaur, M. K. Sharma, and R. K. Gupta, Phys. Rev. C **86**, 064610 (2012); K. Sandhu, G. Kaur and M. K. Sharma, Nucl. Phys. A **921**, 114 (2014).

[6] M. K. Sharma and R. K. Gupta, Phys. Rev. C **85**, 024604 (2012).

[7] G. Kaur, and M. K. Sharma, Phys. Rev. C **87**, 044601 (2013).

[8] G. Sawhney, G. Kaur, M. K. Sharma, and R. K. Gupta, Phys. Rev. C **88**, 034603 (2013).

[9] R. Kumar, K. Sandhu, M. K. Sharma, and R. K. Gupta, Phys. Rev. C **87**, 054610 (2013) .

[10] K. Sandhu, M. K. Sharma, A. Kaur, and R. K. Gupta, Phys. Rev. C **90**, 034610 (2014).

[11] A. Kaur, G. Kaur, and M. K. Sharma, Nucl. Phys. A **941**, 152 (2015).

[12] N. Grover, G. Kaur, and M. K. Sharma, Phys. Rev. C **93**, 014603 (2016).

[13] M. Kaur and M. K. Sharma, Eur. Phys. J. A **50**, 61 (2014).

[14] N. Arunachalam and K. Hangovan, Phys. Rev. C **55** 129 (1995).

[15] N. Grover, I. Sharma, G. Kaur, Manoj K. Sharma Nucl. Phys. A **959**, 10-26 (2017).

[16] W. Nazarewicz, Joint Institute for heavy ion research, Holified heavy ion research facility, P.O. Box 2008, Oak Ridge, Tennessee 37831, USA (1991).

[17] R. K. Gupta, M. Balasubramaniam, R. Kumar, N. Singh, M. Manhas, W. Greiner, J. Phys. G : Nucl. Part. Phys. **31**, 631 (2005);

[18] R. K. Gupta, M. Manhas, W. Greiner, Phys. Rev. C **73**, 054307 (2006).

[19] M. Kaur, R. Kumar, and M. K. Sharma, Phys. Rev. C **85**, 014609 (2012).

[20] G. Kaur and M. K. Sharma, Phys. Rev. C **87**, 044601 (2013).

[21] A. M. Stefanini et al., Eur. Phys. J. A **23**, 473 (2005); S. Kanwar, M. K. Sharma, B. B. Singh, R. K. Gupta, and W. Greiner, Int. J. Mod. Phys E **18**, 1453 (2009).

[22] L. Corradi, S.J. Skorka, U. Lenz, K.E.G. Liibner, P.R. Pascholati, *et.al.*, Z. Phys. A - Atomic Nuclei **334**, 55-72 Zeitschrift, (1990).

[23] S. Kumar, D. Bir, and R. K. Gupta, Phys. Rev. C **51**, 1762 (1995).

Chapter 4

Decay analysis of compound nuclei formed via loosely bound projectiles, ^{6}Li and ^{17}F

In the previous chapter, the decay of compound nuclei (^{118,120,122}Xe*) formed in CF process was explored using DCM [1–9] framework. The relevance of excitation energy, deformations, orientations and angular momentum was studied in reference to the decay of Xe isotopes. Additionally, the effect of N/Z ratio was also explored in view of the fragmentation analysis and mass distribution of decaying fragments. Next, to extend this study, the present chapter aims to explore the CN mechanisms observed in the reactions induced via loosely bound projectiles. Here, in this chapter, the main emphasis is to explore the incomplete fusion (ICF) contribution and to compare the decay profiles of compound nuclei formed in CF and ICF processes for intermediate and light mass region of compound systems. To pursue with it, the dynamics of ^{6}Li+^{159}Tb and ^{17}F+^{58}Ni reactions is studied using DCM in context to the experimental data of [10] and [11] respectively. The decay analysis of these reactions in DCM framework is published in [12, 13]. This chapter provides a brief description of reactions induced with loosely bound projectiles in Sec. 4.1. Further, the calculations and results attained for the decay mechanism of ^{6}Li+^{159}Tb and

^{17}F+^{58}Ni reactions are presented in Sec. 4.2.1 and Sec. 4.2.2 respectively. Finally, the summary and conclusions are drawn in Sec. 4.3.

4.1 Introduction

Collisions induced by the projectiles having a tightly bound core with one or two loosely bound nucleons in the periphery were of much interest in recent years [14–30]. Projectiles with this behavior belong to the class of loosely bound or halo nuclei. These nuclei are exceptionally different from the nuclei that lie near the valley of stability [15]. The unique properties of halo or loosely bound nuclei such as diffused density and low breakup threshold make them advantageous to obtain a deeper insight of breakup and transfer processes. Furthermore, the halo nuclei because of their much more anomalous properties and exotic nature have attracted more attention in recent past. Besides this, stable weakly bound nuclei (e.g., ^{6,7}Li,and ^{9}Be), which acquire qualitatively similar characteristics to those of halo nuclei, are also of considerable interest. This is because it is much easier to perform experiments with stable weakly bound nuclei as they are much more intense than the presently available radioactive beams [16]. Additionally, because of the higher breakup probability, weakly bound projectiles dissociate into smaller fragments under the combined influence of repulsive Coulomb and attractive nuclear interaction. Because of this breakup, various processes other than the direct complete fusion (DCF) become apparent. Here the DCF refers to the process where the whole projectile directly amalgamates with the target. The processes due to the breakup are non-capture breakup (NCBU) where no fragment collides with the target, incomplete fusion (ICF) that includes the collision of only one part of the projectile with the target, and sequential complete fusion (SCF) where the fragments of projectile fuse with the target sequentially [16]. The above mentioned structural effects of weakly bound nuclei provide an anomalous scenario, which in turn helps to understand the dynamics involving such projectiles. Apart from these peculiarities, such kinds of nuclei are also responsible for the suppression or enhancement

of the fusion cross-sections. Various theoretical predictions result in the conflicting statement with regard to the enhancement or suppression of fusion cross-section, due to the breakup channel at both above and below barrier energies [17–25]. The reactions such as ^{9}Be + ^{208}Pb [26], ^{6}Li + ^{96}Zr [27], ^{6,7}Li + ^{144}Sm, ^{16,17}O + ^{144}Sm [28], ^{17}F + ^{208}Pb [15], ^{6}He + ^{209}Bi [29], and ^{6}He + ^{238}U [30] show suppression at the above-barrier and enhancement at the below-barrier energies. Furthermore, It has also been observed that the less breakup threshold or loosely bound nature of projectile is responsible for the enhancement of reaction cross-sections (σ_R) but not the total fusion cross-sections [11]. Here, the total fusion refers to the sum of complete fusion (CF) and incomplete fusion (ICF), whereas the reaction cross-section is the sum of cross-sections resulting from all possible processes. These anomalies make scientists curious to explore more about the reactions involving such exotic nuclei, so many efforts have been made to produce more and more such beams. Moreover, many research articles and review papers are published on similar topics [14, 31–37].

In view of above, the DCM has been utilized to examine the decay mechanisms of compound nuclei formed in reactions involving loosely bound bound projectiles. The present chapter mainly deals with the decay profiles associated with CF and ICF processes for ^{6}Li (S_α ≈1.473 MeV) and ^{17}F (S_P=0.600 MeV) induced reactions, where S_α and S_P are separation energies of alpha and proton respectively.

4.2 Calculations and results

4.2.1 Decay analysis of ^{6}Li+^{159}Tb reaction

In ^{6}Li + ^{159}Tb reaction, the projectile (^{6}Li) has low breakup threshold energy equivalent to 1.47 MeV, due to which it splits in the entrance channel and thereby reduces the amount of incoming flux towards fusion, which consequently results in the possibility of ICF process. Thus, in this section, the ER cross-sections produced through CF and ICF processes for ^{6}Li + ^{159}Tb reaction are calculated in context to the recent experimental

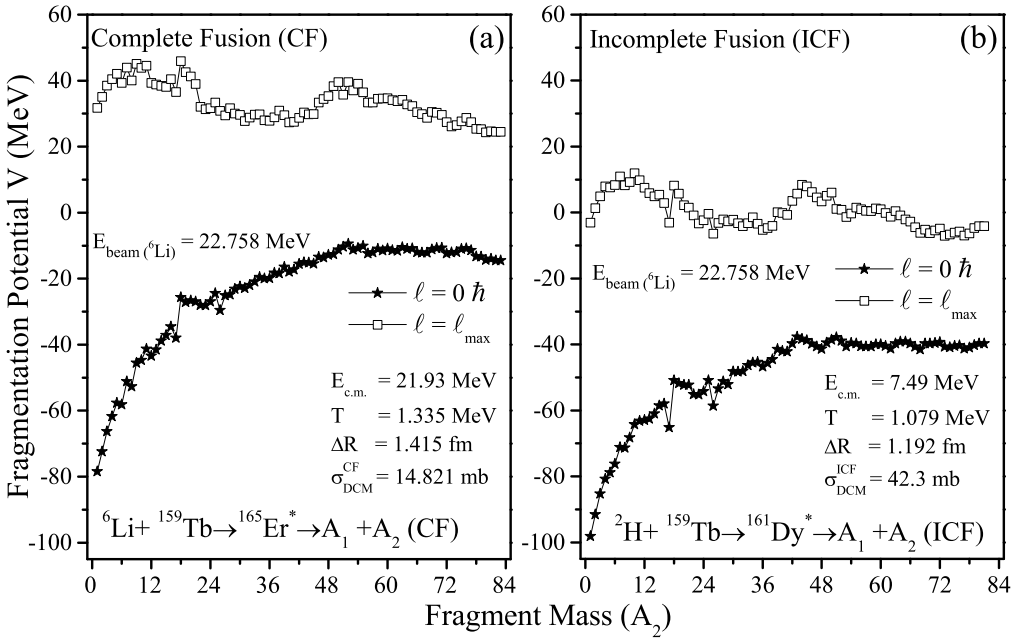

Figure 4.1 Fragmentation potential as a function of fragment mass (A_2) for (a) Complete fusion (CF), (b) Incomplete fusion (ICF) using β_{2i}-deformed choice of fragments.

data [10]. Further, the decay patterns for both CF and ICF processes are examined via fragmentation potential and preformation probability. According to the experimental analysis [10], ^{6}Li breaks into alpha (^{4}He) and deuteron (^{2}H) and the probability of fusion of ^{2}H with ^{159}Tb is more as compare to the alpha particle (^{4}He) [10]. Thus, the channel ^{2}H + ^{159}Tb is considered as an ICF channel. Also, it is pertinent to mention here that the calculations for the ICF decay are made after appropriate energy correction as per Eq. (2.14) of chapter 2. The results obtained are discussed ahead.

Firstly, to investigate the decay profile of compound nuclei formed through CF (^{165}Er*) and ICF (^{161}Dy*) channel, the fragmentation behavior and thus the comparative contribution of energetically favored fragments is analysed along with the angular momentum effects. Fig. 4.1 depicts the fragmentation potential which acts as an input to the Schrödinger equation to compute the preformation probability (P_0) and hence the cross-sections for β_{2i}-deformed choice of fragmentation. It is evident from Fig. 4.1 that the structure of potential energy surfaces of ICF does not change much with respect to the

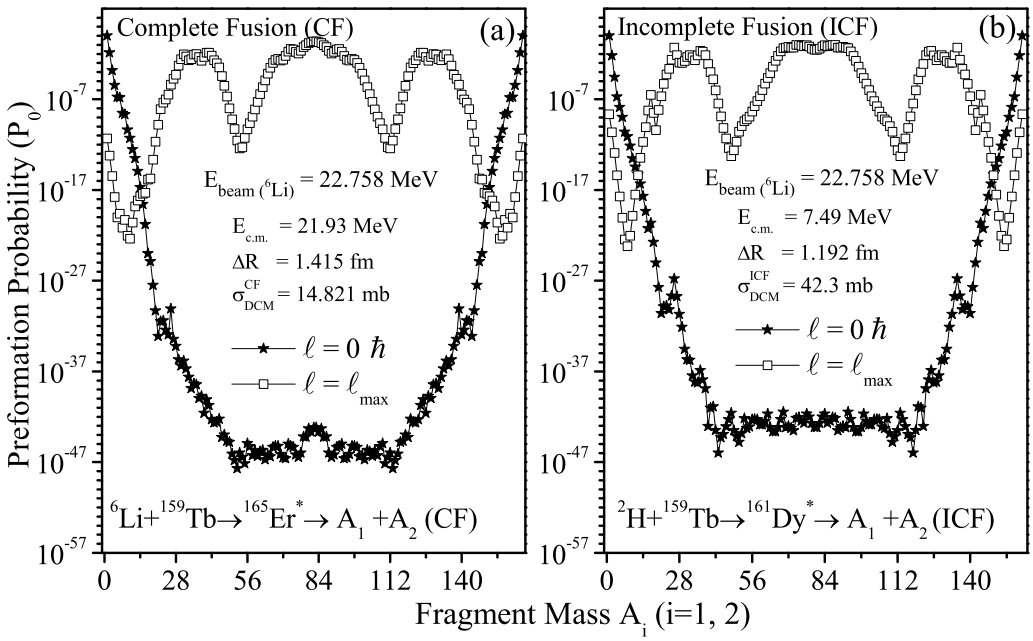

Figure 4.2 Preformation probability (P_0) as a function of fragment mass (A_i) for (a) Complete fusion (CF), (b) Incomplete fusion (ICF) using β_{2i}-deformed choice of fragments.

CF except for some minor change in HMF and fission region. Next, the insight of decay pattern and structural aspects can also be understood from the preformation curve as depicted in Fig. 4.2. This figure shows the variation of preformation probability as a function of fragment mass for both CF and ICF, where Fig. 4.2 (a) shows the preformation profile for CF and (b) represents the same for ICF. Fig. 4.2 clearly reveals that for both processes, the probability of evaporation residue is higher at ℓ=0$\hbar$ in comparison to that at ℓ=ℓ_{max}. Furthermore, the preformation profile looks similar for both processes exhibiting triple humped structure. However, analogous to structure of potential energy surfaces (see Fig. 4.1), the preformation curve also exhibit minor difference in HMF and fission region. Similar results have been obtained at highest energy (not shown here).

Next, the DCM calculated cross-sections for both processes are shown in Fig. 4.3(a). According to the experimental observations, the complete fusion evaporation residue (ER) results due to the neutron contribution from 2n to 5n and incomplete fusion ER have neutron contribution from 1n to 3n. Both CF and ICF cross sections are addressed

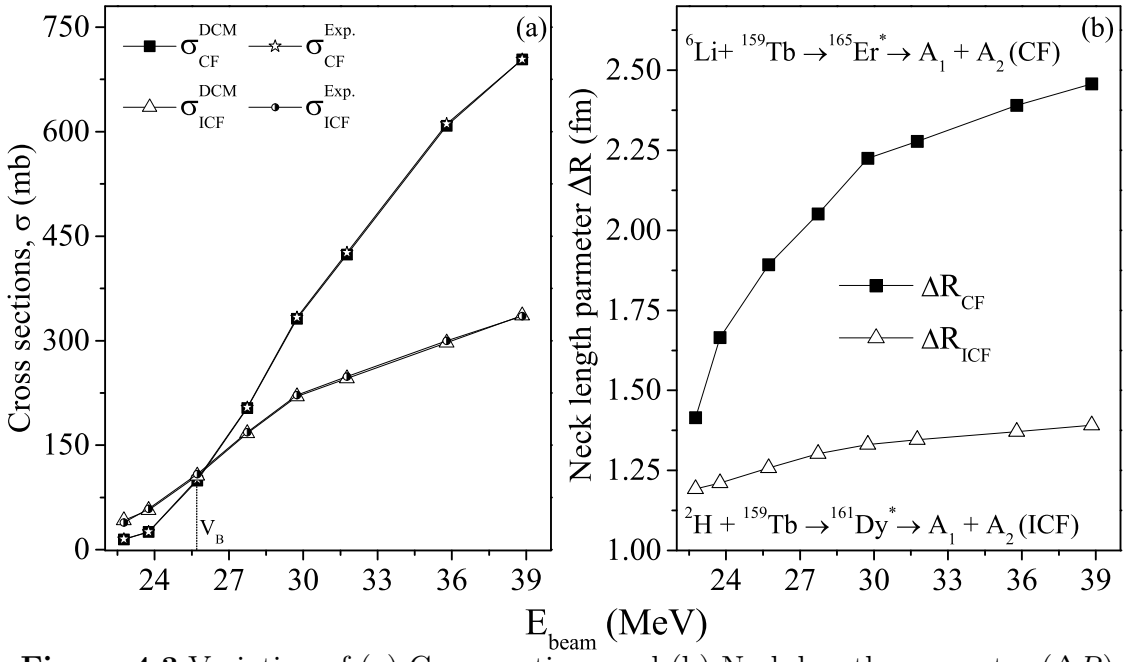

Figure 4.3 Variation of (a) Cross-sections and (b) Neck length parameter (ΔR) as a function of incident energy (E_{beam}) for both CF and ICF

accordingly. Fig. 4.3(a) clearly reveals that the cross-sections determined using DCM are in nice accordance with the experimental data [10]. Further, it can be noticed from the figure that at below barrier energies, the contribution of ICF cross-sections is higher than that of the CF. This might be owing to the contribution of some transfer processes at sub-barrier energies [10]. The cross-sections in DCM are estimated by using one fitting parameter that is neck length parameter (see Eq. (2.16) of chapter 2). Fig. 4.3(b) depicts the variation of neck length parameter (ΔR) as a function of initial beam energy (E_{beam}) for both CF and ICF channels. It is clearly visible from Fig. 4.3(b) that ΔR increases with the increase in energy for complete fusion, where ΔR is much higher 2.457 fm at highest energy (38.84 MeV) as compare to 1.415 fm for lowest energy (22.76 MeV). Similar observation can be seen for ICF. However, the magnitude of ΔR for ICF process is much lower as compared to that for CF process. This is possibly due to the smaller size of the composite system formed in ICF. Further, to extend this analysis, DCM has also been applied to study the ^{17}F+^{58}Ni reaction forming relatively lighter mass compound nucleus. The discussion relating the dynamics of CF and ICF component of ^{17}F+^{58}Ni reaction is

presented in the following section Sec. 4.2.2.

4.2.2 Dynamics of ^{17}F+^{58}Ni reaction via CF and ICF processes

In ^{17}F+^{58}Ni reaction, the projectile (^{17}F) shows exotic characteristics. It has been observed that the first excited state of ^{17}F show halo behavior [38] however, the ground state of the same shows loosely bound characteristics with the proton separation energy equal to 0.600 MeV [11]. It is pertinent to inscribe here that in the present work, the ground state of ^{17}F is considered to explore the dynamics of ^{17}F+^{58}Ni reaction. Now, the breakup of ^{17}F at sufficiently large distance reduces the Coulomb barrier of the remaining core ^{16}O, which results in the enhancement of reaction cross-sections due to possible involvement of other competing processes. As a result, the study of ^{17}F as a projectile provides a unique opportunity to explore the changes in cross-sections around the Coulomb barrier. Here, an effort is made to examine the dynamics of ^{17}F + ^{58}Ni reaction in the framework of dynamical cluster-decay model (DCM) [1–9]. The reaction is analyzed at two beam energies of ^{17}F (E_{beam} = 54.1 and 58.5 MeV) in context to the recent experimental data [11]. The beam energies of ^{17}F are corrected for ICF according to Eq. (2.14) of chapter 2, and thus, one can extract the appropriate center-of-mass energy for both CF and ICF channels using Eq. (2.11) of chapter 2. It is important to inscribe here that CF cross-sections are determined by deducting the inelastic, breakup, and stripping cross-sections from the total reaction cross-sections. Next, the comparison of the decay profile associated with CF and ICF channel is performed in the DCM framework. This decay profile may include components like fragmentation path, preformation probability, and barrier modification. Furthermore, the temperature of the selected reaction at energies used in the present analysis is greater than 1.5 MeV, and according to Davidson *et al.* [39], the pairing constant ($\delta(T)$) approaches to zero at T>1.5 MeV. However, Bansal *et al.* [40] suggested that $\delta(T)$ vanishes at much higher temperature. Thus, the role of the pairing constant(δ) is explored by comparing the decay paths resulting from the calculations at $\delta(T) \neq 0$ [40] and $\delta(T) = 0$ [39]. The present section is divided into two subsections: Sec. 4.2.2(a) presents the comparison of CF and ICF and Sec. 4.2.2(b) describes the role of

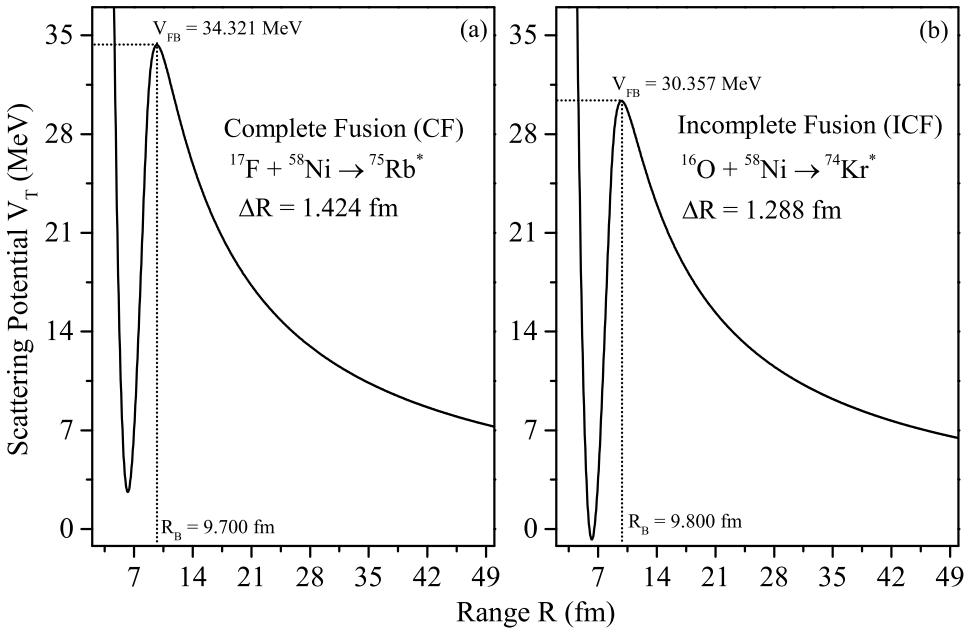

Figure 4.4 Variation in scattering potential V_T (sum of V_P and V_C) as a function of range R (fm) exhibiting the fusion barrier for (a) Complete fusion (b) Incomplete fusion at $E_{beam}(^{17}F)$=54.1 MeV.

pairing coefficient.

4.2.2(a) Comparison of CF and ICF processes

First, the comparison of CF (^{17}F+^{58}Ni→^{75}Rb*) and ICF (^{16}O+^{58}Ni→^{74}Kr*) channel is carried out to understand the fusion barriers (FBs) associated with them. Fig. 4.4(a) and (b) shows the FB for CF and ICF channels, respectively. This scattering potential is estimated at $\ell = 0\hbar$, which means that it represents the summation of the Coulomb and proximity potentials. Fig. 4.4 shows that there is a decrease in the barrier height for ^{16}O+^{58}Ni→^{74}Kr* (ICF) channel, which is due to the decrease in the magnitudes of Coulomb and proximity potentials in this channel. As the partial projectile (^{16}O) collides with the target in ICF, it will acquire a comparatively lesser Coulomb potential. Furthermore, the neck (ΔR) is smaller in ICF channel than in the CF channel, which in turn reduces the proximity potential; hence, the magnitude of barrier height for ^{16}O+^{58}Ni→^{74}Kr* (ICF) is lesser than that for ^{17}F+^{58}Ni→^{75}Rb* (CF) reaction. Moreover, the barrier po-

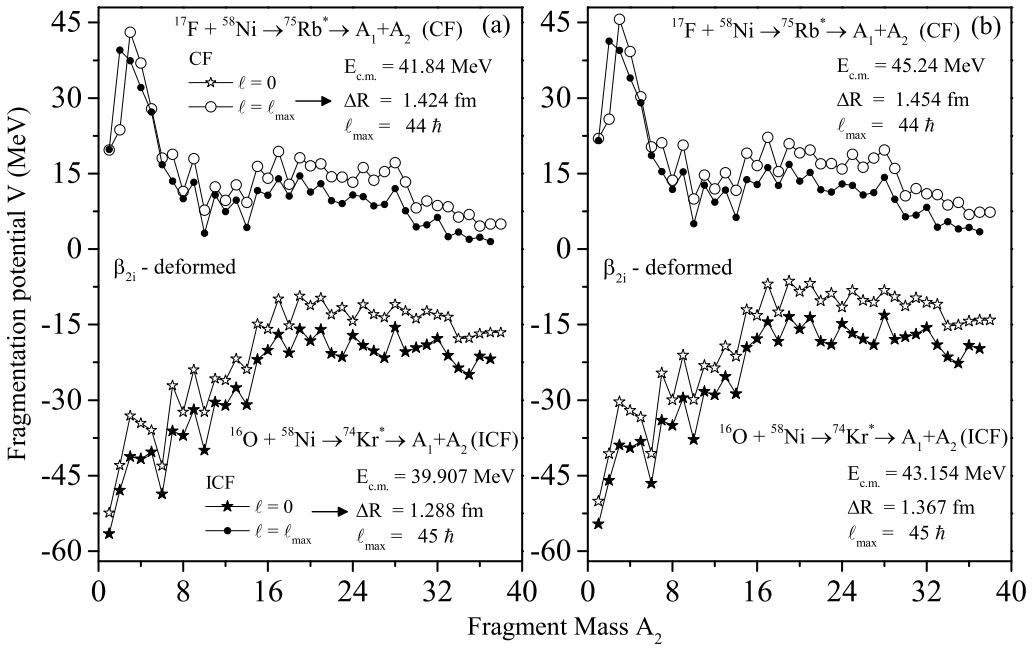

Figure 4.5 Fragmentation potential exhibited as a function of fragment mass (A_2) at two beam energies of ^{17}F (a) E_{beam}=54.1 MeV and (b) 58.5 MeV for CF and ICF by including β_{2i}-deformed choice of fragments using the optimum orientation approach.

sition increases for the ICF channel from 9.7 to 9.8 fm, which seems to suggest that the interaction is slightly more stronger in CF than in ICF. Further, to examine the difference between their decay profiles, the variation in the fragmentation potential, $V(A_2)$, attributing both CF and ICF for all possible fragments in the outgoing channel is shown in Fig. 4.5. This figure illustrates $V(A_2)$ for the decay of both compound nuclei formed in the CF and ICF at two extreme values of angular momentum and beam energies for ^{17}F (E_{beam} = 54.1 and 58.5 MeV) by including the β_{2i}-deformation effects in both CF and ICF. The main purpose to analyze the fragmentation behavior in Fig. 4.5 is to examine the potential for various mass regions such as ER, IMF, HMF, and fission so that the comparative dynamics of CF ($^{17}F+^{58}Ni \rightarrow ^{75}Rb^{*}$) and ICF ($^{16}O+^{58}Ni \rightarrow ^{74}Kr^{*}$) processes be analysed. Further, it is worthwhile to inscribe that the lower fragmentation potential of the fragments leads to the higher probability for their decay. In Fig. 4.5, open and filled symbols represent the decay of compound nucleus formed in the CF and ICF channels, respectively. "Stars" represent $V(A_2)$ at the minimum ℓ-value and "circles" represent the

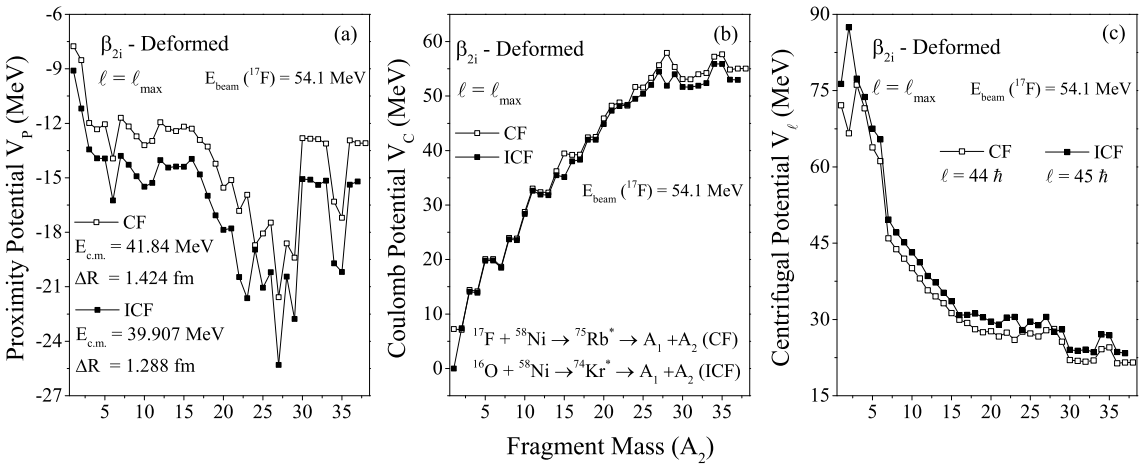

Figure 4.6 Comparison of CF and ICF processes based on the components of fragmentation potential: (a) proximity potential (V_P), (b) Coulomb potential (V_C), and (c) centrifugal potential (V_ℓ) at $E_{beam}(^{17}F)$=54.1 MeV.

$V(A_2)$ at the maximum ℓ-value. Fig. 4.5(a) and (b) shows the fragmentation behavior at the minimum and maximum energies, respectively. From the effect of incident energy, it is clearly evident that both the structure of potential energy surfaces and the magnitude of fragmentation potential do not change much as a function of beam energy. Further from the comparison of CF and ICF, it is clearly visible from the figure that the structure of the decay profile in both cases is not much different; however, the magnitude of $V(A_2)$ is influenced significantly. At ℓ=0 $\hbar$, the magnitude of fragmentation potential for $^{74}Kr^*$ (formed in ICF) is lower than that for $^{75}Rb^*$ (formed in CF) for all fragments. Similar results are obtained at the maximum angular momentum except for the ER region, i.e., $V(A_2)$ for a fragment having mass (A_2 =1) possesses the same potential for both the compound nuclei formed in the CF and ICF, whereas a fragment having A_2 =2 acquires a much lower value of $V(A_2)$ in the case of CF path. This observation indicates that the probability of ER formation in CF should be more than that from ICF, which is analyzed further in Fig. 4.8. Another finding from the Fig. 4.5 is that at $\ell = 0$ $\hbar$, ER has the minimum fragmentation potential, which is reversed at higher ℓ-values. Now, the proximity potential (V_P), Coulomb potential (V_C), and the centrifugal potential (V_ℓ) provide three important inputs to the fragmentation potential as evident from Eq. (2.15)(chapter 2).

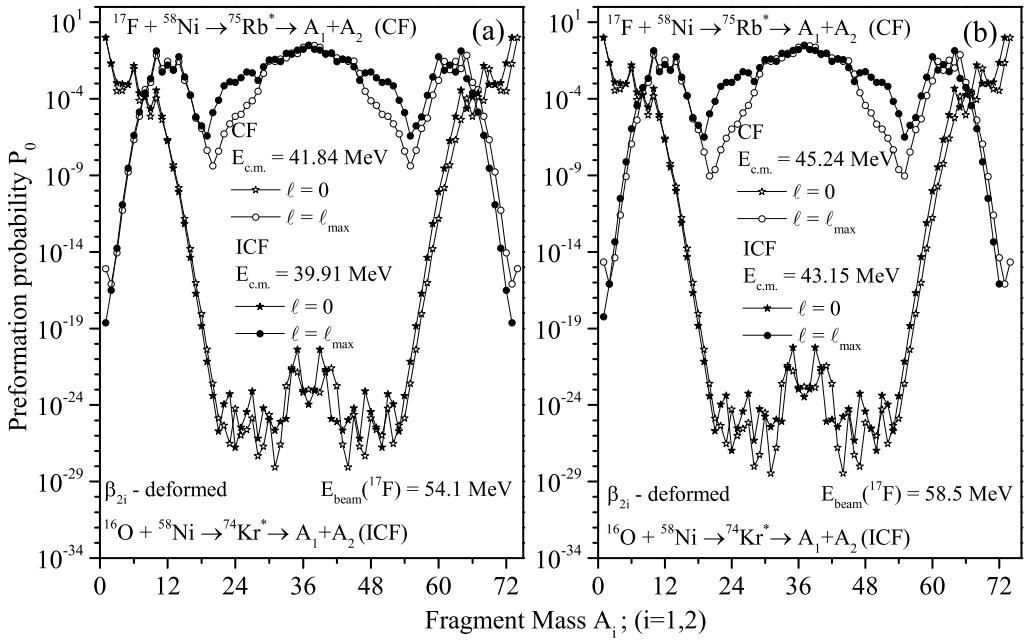

Figure 4.7 Comparison of mass distribution of the fragments for complete and incomplete fusion channels at two beam energies of ^{17}F (a) E_{beam}=54.1 MeV and (b) 58.5 MeV.

Thus, it would be interesting to examine the comparison of CF and ICF in terms of these potentials. Fig. 4.6 illustrates the variation in the (a) proximity potential (b) Coulomb potential, and (c) centrifugal potential with fragment mass (A_2) for both CF and ICF. It is clearly visible from Fig. 4.6(a) that the magnitude of proximity potential is lower for the ICF case than that for the CF case. The proximity potential depends on the distance of the closest approach, and in the DCM, ΔR represents the same. Hence, V_P is directly related to the neck length parameter (ΔR), which is smaller in the ICF case; thus, the proximity potential is lesser for the ICF than for the CF case. The Coulomb potential for the decaying fragments in both channels is presented in Fig. 4.6(b), which directly depends on the charge, deformations, and orientations of the emitting fragments [refer Eq. (2.22) of chapter 2]. It can be seen from the figure that V_C increases with the increase in charge and hence with mass. It is clearly visible from the figure that upto $A_2 \leq 14$, V_C almost overlaps for both channels except for the fragment with $A_2 = 1$. This is because the fragment with $A_2 = 1$ is ^{1}H in CF and ^{1}n in ICF, which leads to a higher value of V_C for $A_2 = 1$ in the case of CF. Further, at $A_2 > 14$, the magnitude of V_C for the fragments

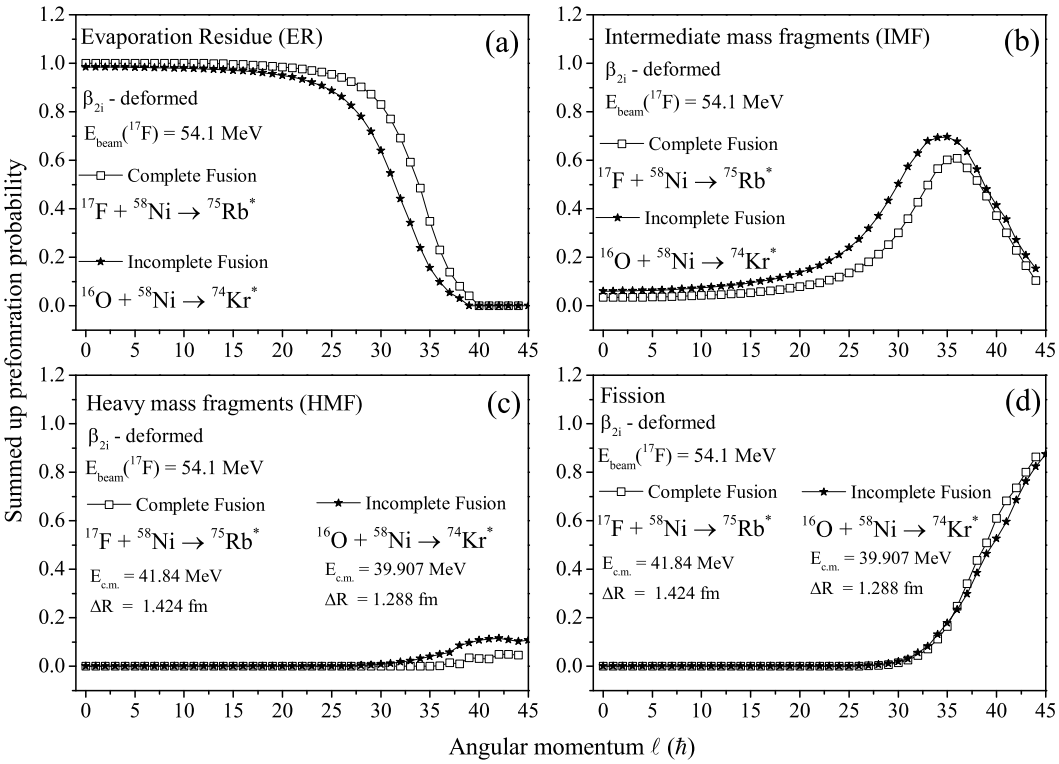

Figure 4.8 Summation of the preformation probabilities of all possible decay modes: (a) evaporation residue (ER), (b) intermediate mass fragments (IMFs), (c) heavy mass fragments (HMFs), and (d) fission, varying as a function of angular momentum (ℓ) for both CF and ICF channels at a lower beam energy of ^{17}F (E_{beam}=54.1 MeV).

emitted in the CF is higher, which is due to the higher charge and thus more Coulomb repulsion of the fragments in this case. The centrifugal potential (V_ℓ) is presented in Fig. 4.6(c). One can clearly see from the figure that V_ℓ decreases with the increase in mass. Further, it is observed that the centrifugal potential is higher for the fragments emitting from the system formed in the ICF channel. The reason for this higher magnitude of V_ℓ in the case of ICF is directly related to the angular momentum, which is greater for the ICF; hence, the outgoing fragments in the ICF case acquire more centrifugal potential.

After the above discussion on the behavior of fragmentation potential and its components, we intend to understand the behavior of preformation probability, which is calculated as a stationary solution of the Schrödinger wave equation (see Eq. (2.6) of chapter 2), in which the fragmentation potential serves as an essential input. Thus, to investigate further the preformation probability P_0 of all fragments in both CF and ICF cases is plotted in Fig. 4.7 at the same energy and angular momentum, where $V(A_2)$ is examined

Table 4.1 The DCM-calculated cross-sections for evaporation residue (ER), intermediate mass fragments (IMFs), heavy mass fragments (HMFs), and fission along with the ΔR, angular momentum, center-of-mass energy, and temperature. The ER cross-sections are compared with the experimental data [11].

S. No.	$E_{c.m.}$ (MeV)	Temp. (MeV)	ℓ ($\hbar$)	ΔR (fm)	σ_{DCM} at $\Delta R \simeq \Delta R^{ER} - 0.5$ σ_{ER} (mb)	σ_{IMF} (mb)	σ_{HMF} (mb)	$\sigma_{Fission}$ (mb)	$\sigma_{Exp.}$ (mb)	%age of $\sigma_{IMF+HMF+Fission}$
Complete Fusion (CF)										
1	41.84	2.326	44	1.424	428	0.259	1.45×10^{-5}	0.122	425	0.089%
2	45.24	2.415	44	1.454	455	0.234	1.34×10^{-5}	0.095	453	0.072%
Incomplete Fusion (ICF)										
1	39.91	2.254	45	1.288	10.6	0.0166	2.72×10^{-7}	3.66×10^{-3}	11.1±0.7	0.2%
2	43.15	2.343	45	1.367	13.6	0.0137	1.95×10^{-7}	2.80×10^{-3}	14.2±0.9	0.12%

in Fig. 4.5. Fig. 4.7 shows the same results for P_0 as obtained in Fig. 4.5 for $V(A_2)$, that is, there is no effect of incident energy on the preformation distribution as well. It can also be seen from the figure that the decay of compound nucleus formed in both CF and ICF possesses near-symmetric mass distribution in the fission region. However, the difference between CF and ICF is clearly evident in the region ($18 \leq A_2 \leq 30$), as the fragments lying in this region seem to be more probable for the ICF case than for the CF case.

Fig. 4.8 demonstrates the summation of the preformation probabilities as a function of angular momentum for all four regions ER, IMF, HMF, and fission in panels (a), (b), (c), and (d), respectively, at $E_{beam}(^{17}F) = 54.1$ MeV. One may clearly see from Fig. 4.8(a) that for both CF and ICF, the probability of emission of ER is almost consistent and maximum for a particular ℓ-window ($0 \leq \ell \leq 20\hbar$) and then decreases gradually and becomes almost negligible at $\ell \geq 40\hbar$. Further, it is higher in CF than in ICF. Second, the summation of the preformation probabilities for IMF region is presented in Fig. 4.8(b). The figure illustrates that ΣP_0 is approximately zero up to $\ell \approx 20\hbar$ and then attains the maximum value at $\ell = 35\hbar$ before reducing to zero at about 45 $\hbar$. By comparing Fig. 4.8(a) and (b), it can be affirmed that the ER region is more probable than that of the IMF for both the processes at lower ℓ-values and that the IMF dominates at higher

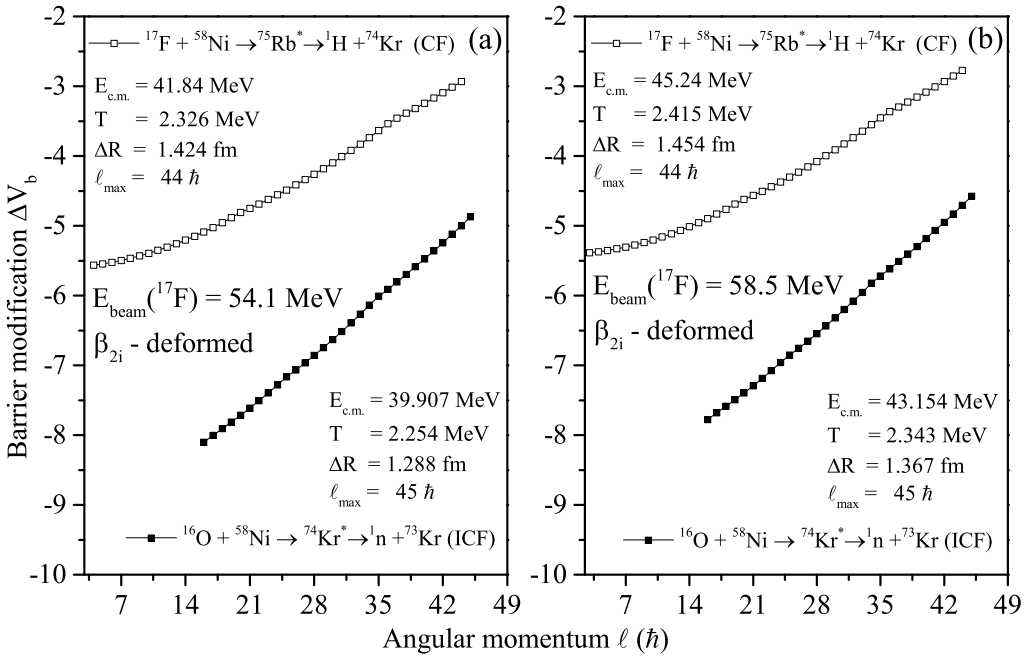

Figure 4.9 Comparison of complete and incomplete fusion in terms of barrier modification for the most probable fragment at two given energies for β_{2i}-deformed choice of fragments using the optimum orientation approach.

ℓ-window. Furthermore, panel (c) of Fig. 4.8 shows the contribution of HMF from the decay of compound systems formed in CF and ICF channels. It can be observed from the figure that the contribution of HMF is negligibly small at all ℓ-values. Finally, ΣP_0 for the fission region is plotted in panel (d) of Fig. 4.8, which clearly depicts that there is no distinction between the fission regions of CF and ICF paths similar to their HMF regions. The probability of fission contribution towards the decay channel is negligible up to $\ell \approx 30\hbar$, after which it increases at higher ℓ-values. Concluding the analysis of Fig. 4.8, one may say that ER is the most dominant decay mode among the four possibilities considered here.

Furthermore, the cross-sections for CF and ICF are estimated by optimizing the neck length parameter (ΔR) "the only parameter of DCM" and are tabulated in Table 4.1 along with other essential components. It is clearly observed from the table that the DCM computed cross-sections are in good agreement with the experimental data [11]. It is also essential to note here that the experimental ER cross-sections shown in the

second last column in the upper half of the Table 4.1 are extracted from Table II of ref. [11] by subtracting the inelastic, breakup, and stripping cross-sections from the total reaction cross-sections. The cross-sections for IMF, HMF, and fission are addressed at $\Delta R \simeq (\Delta R^{ER} - 0.5) fm$, because these decay modes are supposed to occur at slower pace as compared to ER. The negligible values of cross-sections for IMF, HMF, and fission regions confirm that ER is the most dominant decay mode. Furthermore, the ΔR used to attain σ_{ICF} is lesser than that to attain σ_{CF}. It may be because the ER cross-sections in the case of ICF are much smaller than in the case of CF. The neck length parameter is also an essential parameter to decide the appropriate barrier modification (ΔV_B) for the decay of compound nucleus. To extend the analysis concerning the comparison of CF and ICF, ΔV_B, which is an inbuilt barrier lowering parameter of DCM, is scrutinized as a function of angular momentum and shown in Fig. 4.9 at two energies for the most probable channel of ER. It is clearly visible from the figure that the magnitude of ΔV_B reduces with the increase in angular momentum for both the channels (CF and ICF). By comparing Fig. 4.9(a) and (b), one may notice that the effect of energy on barrier modification is similar to that of angular momentum on it. Hence, lesser barrier modification is required at higher energies and ℓ-values. This observation is in accordance with a previous study performed using the DCM [2]. Moving toward the comparison of CF and ICF, a lesser barrier modification is required for CF than that for ICF. The neck length parameter is also higher for CF than that for ICF, thus one may conclude that a lower neck leads to a higher barrier modification and vice versa. In addition to the comparative study on the CF and ICF processes, an attempt is made to study the dynamics of ^{17}F+^{58}Ni$\rightarrow^{75}$Rb* and ^{16}O+^{58}Ni$\rightarrow^{74}$Kr* reactions at common reduced center-of-mass energy ($E_R \approx 1$ MeV) [41]. According to Mazzoccoa *et al.* [11, 42] and Strano *et al.* [43], the comparison of reduced reaction cross-sections ($\sigma_R/(A_p^{1/3}+A_t^{1/3})^2$) shows moderate enhancement for ^{17}F+^{58}Ni as compared to that for ^{16}O+^{58}Ni reaction. In the present work, only ER cross-sections are considered as they are the dominant contributor toward σ_R. The data of the cross-sections for ^{16}O- and ^{17}F- induced reactions is taken

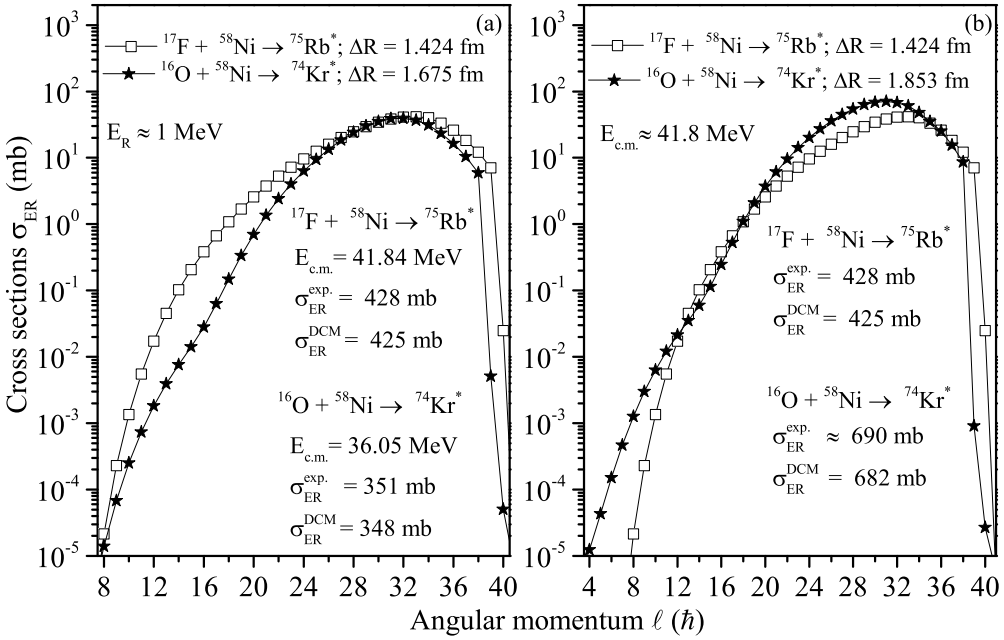

Figure 4.10 Variation of evaporation residue (ER) cross-sections as a function of angular momentum for ^{17}F+^{58}Ni→^{75}Rb* and ^{16}O+^{58}Ni→^{74}Kr* at (a) common reduced center-of-mass energy [E_R=$E_{c.m.}$($A_p^{1/3}$+$A_t^{1/3}$)/(Z_pZ_t.)] equivalent to 1.0 MeV and (b) common center-of-mass energy ($E_{c.m.}$ ≈ 41.84 MeV).

from [44,45] and [11], respectively. Fig. 4.10(a) shows the ER cross-sections of compound nuclei formed via ^{17}F and ^{16}O projectiles striking on the target (^{58}Ni) at common reduced center-of-mass energy E_R [=$E_{c.m.}$($A_p^{1/3}$+$A_t^{1/3}$)/(Z_pZ_t.)]. This figure depicts that the estimated ER channel cross-sections are larger in magnitude for ^{17}F(loosely bound)+^{58}Ni reaction for the majority of ℓ-states. The larger cross-sections for ^{17}F based reaction are possibly due to the higher center-of-mass energy ($E_{c.m.}$=41.84 MeV) than $E_{c.m.}$ (= 36.05 MeV) for ^{16}O-induced reaction. It has been further observed that a slight increase in the center-of-mass energy for ^{16}O+^{58}Ni→^{74}Kr* reaction (say 1 MeV) reverses the trend, making the ER cross-sections for ^{74}Kr* larger than those for ^{75}Rb* nucleus. This might be due to the loosely bound nature of ^{17}F projectile, which suppress the CF cross-sections of ^{17}F+^{58}Ni reaction. Also, the ER cross-sections of both compound nuclei ^{75}Rb* (formed through ^{17}F+^{58}Ni) and ^{74}Kr* (formed through ^{16}O+^{58}Ni) are plotted as a function of the angular momentum at common center-of-mass energy ($E_{c.m.}$ ≈ 41.8 MeV) in Fig. 4.10(b). The figure clearly depicts that the contribution of ER cross-sections become

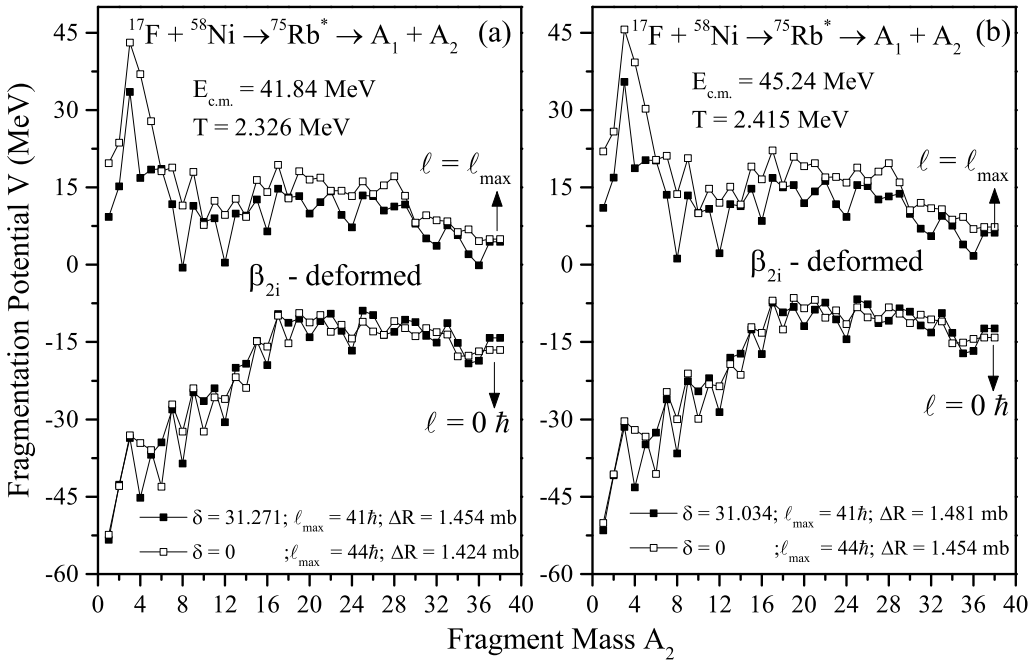

Figure 4.11 Comparison of fragmentation potential ($V(A_2)$) calculated using zero and non zero pairing coefficients is represented by its variation with fragment mass (A_2) for both cases at two given center-of-mass energies.

relatively more prominent for ^{16}O-induced channel for the majority of ℓ-states.

4.2.2(b) Role of pairing coefficient

In this section, the role of temperature-dependent pairing strength ($\delta(T)$) is discussed. The coefficient of pairing energy term is used as an input in liquid drop potential, which is further responsible for structural effects through the fragmentation potential. The pairing term of liquid drop part of binding energy is given as follows:

$$Pairing\ \ energy = \delta(T)\frac{f(A,Z)}{A^{3/4}} \tag{4.1}$$

where $f(A,Z)$=(-1,0,1) for even-even, even-odd, and odd-odd nuclei, respectively. The coefficient of pairing energy is constrained to be positive definite at all values of temperature. In the reaction under investigation, i.e., ^{17}F + ^{58}Ni, the temperature (calculated from the compound nucleus excitation energy using Eq. (2.10) of chapter 2) is greater than 1.5 MeV and the coefficient ($\delta(T)$) of pairing energy term in semi empirical mass

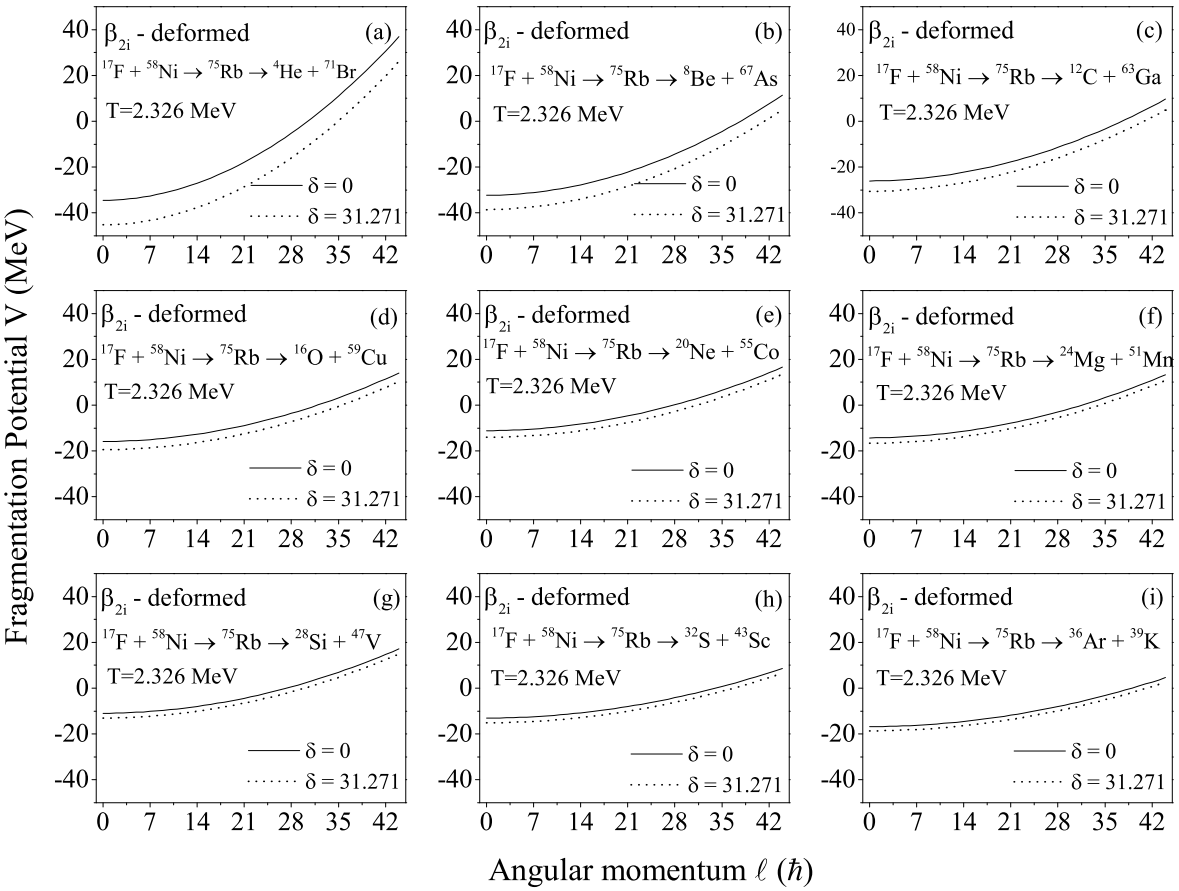

Figure 4.12 Variation in the fragmentation potential ($V(A_2)$) of 4n-group fragments as a function of angular momentum (ℓ) obtained with the inclusion of zero [39] and non-zero [40] pairing coefficient at lowest center-of-mass energy ($E_{c.m.}$=41.84 MeV).

formula estimated by Davidson *et al.* converges to zero at T≥1.5 MeV [39]. Thus the odd-even effect of binding energy is supposed to be negligibly small for T>1.5 MeV. However, Bansal *et al.* [40] suggested significant values of $\delta(T)$ even at temperatures higher than 1.5 MeV. Thus, it would be interesting to explore the effect of $\delta(T)$ on the decay of compound nucleus $^{75}Rb^*$ formed by the ^{17}F-induced reaction. Subsequently, a comparative study of results obtained using zero [39] and non zero [40] values of pairing strength is performed.

Fig. 4.11 shows the fragmentation potential ($V(A_2)$) for each fragment lying in ER, IMF, HMF, and fission regions calculated using the collective clusterization approach of DCM at two given energies (a) $E_{c.m.}$ = 41.84 MeV and (b) 45.24 MeV. It is noticed from the figure that the minima in potential energy surfaces obtained after including the non-

zero pairing strength ($\delta(T) \neq 0$) appears for 4n-clusters, i.e., fragments having mass (A_2) equal to 4, 8, 12, 16, ..., and therefore, these fragments are more prominent toward decay mode. On the contrary, for the zero pairing coefficient ($\delta(T) = 0$) taken from Davidson *et al.*, the fragments having 4n+2 clusters (A_2 = 6, 10, 14, 18, ...) acquire minimal value of $V(A_2)$, which implies that stable clusters are formed at A_2=4n+2. Furthermore, the neck length parameter for $\delta(T) \neq 0$ is greater than that for $\delta(T) = 0$. Hence, lesser barrier modification is required for the former case. Additionally, it is worthwhile to inscribe that similar observations are drawn for other compound nuclei investigated by the DCM [46]. Furthermore, to analyze the role of pairing strength, the variation in fragmentation potential of 4n-type fragments as a function of angular momentum is depicted for both $\delta(T) = 0$ and $\delta(T) \neq 0$ cases as shown in Fig. 4.12. It is clearly evident from the figure that $V(A_2)$ follows an increasing trend with angular momentum for all possible 4n fragments. However, this rise in fragmentation potential with ℓ-values is more for lighter fragments than that for heavier ones, which implies that it is maximum for ^{4}He and minimum for ^{36}Ar. With regard to the influence of pairing strength on the fragmentation potential of 4n fragments, one may observe from Fig. 4.12 that the potential of 4n-group fragments calculated with the inclusion of non zero pairing coefficient is less (see Fig. 4.11 also), which signifies that these fragments are more prominent toward decay for $\delta(T) \neq 0$ case. In addition, the difference in values of $V(A_2)$ calculated using zero and non-zero pairing strength decreases with the increase in fragment mass, which means that the temperature dependence of pairing strength is more significant for smaller clusters.

4.3 Summary

In summary, the decay mechanism of ^{6}Li + ^{159}Tb reaction has been studied within the framework of DCM. Since the probability of capturing of lighter fragment (^{2}H) is greater as compared to that of heavier fragment (^{4}He) so the analysis of ICF process is studied for ^{2}H + ^{159}Tb channel. In view of considered reaction, it is noticed that, there is not much

difference in the structure of potential energy surfaces as we move from CF to ICF except for some minor changes in the HMF and fission region. The ICF cross sections within DCM framework find a nice accordance with the experimental data and the emergence of larger neck at higher incident energies seems to support the suppression of above barrier fusion cross-sections.

To widen this horizon, the dynamics of another nuclear reaction (^{17}F+^{58}Ni) having a loosely bound projectile is also explored. Here for this reaction, keeping in mind about the loosely bound nature of ^{17}F, the comparison of CF and ICF for different decay modes (ER, IMF, HMF, and fission) is examined within the DCM framework at two center-of-mass energies. The decay paths of both CF and ICF are examined using various components of DCM such as fragmentation potential V(A_2), preformation probability (P_0), and barrier height. It has been noticed that the structure of potential energy surfaces of fragments is almost similar for both processes (CF and ICF); however, the magnitude of fragmentation potential is significantly influenced, which in turn modifies the preformation probability of fragments. It is noticed that the preformation probability of ER is the highest among the four decay modes (ER, IMF, HMF, and fission) for both CF and ICF channels. Furthermore, the contribution of HMF and fission is almost negligible for both the processes. The cross-sections estimated for CF and ICF processes agree well with the available data. The ICF channel requires smaller neck and hence demands barrier modification of higher magnitude. Additionally, it has also been observed that the magnitude of ER decay cross-sections at common reduced center-of-mass energy (E_R) is greater for ^{75}Rb* (formed through ^{17}F + ^{58}Ni) than that for ^{74}Kr* (formed through ^{16}O + ^{58}Ni). However, this trend is reversed at common center-of-mass energy ($E_{c.m.}$) due to loosely bound nature of ^{17}F. Finally, the study regarding the role of pairing coefficient states that 4n-clusters are more dominant in the decay modes estimated using the modified temperature-dependent pairing coefficient.

After studying the CF and ICF mechanisms, it will be of further interest to explore the nCN processes such as DIC, QF. These processes occur before the formation of equi-

librated compound nucleus and the dynamics of these mechanisms is investigated in the forthcoming chapters.

Bibliography

[1] R. K. Gupta, M. Balasubramaniam, R. Kumar, D. Singh, C. Beck, Nucl. Phys. A **738**, 479 (2004).

[2] M. Kaur, and M. K. sharma, Eur. Phys. J. A **50**, 61 (2014).

[3] R. K. Gupta, S. K. Arun, R. Kumar, and M. Bansal, Nucl. Phys. A **834**, 176c (2010).

[4] M. Kaur, M. K. Sharma, and R. K. Gupta, Phys. Rev. C **86**, 064610 (2012); K. Sandhu, G. Kaur and M. K. Sharma, Nucl. Phys. A **921**, 114 (2014).

[5] R. Kumar, K. Sandhu, M. K. Sharma, and Raj K. Gupta, Phys. Rev. C **87**, 054610 (2013);D. Jain, R. Kumar, M. K. Sharma, R. K. Gupta, Phys. Rev. C **85**, 024615 (2012).

[6] G. Sawhney and M. K. Sharma, Eur. Phys. J. A **48**, 57 (2012).

[7] G. Sawhney, G. Kaur, M. K. Sharma, and R. K. Gupta, Phys. Rev. C **88**, 034603 (2013).

[8] M. Kaur, R. Kumar, and M. K. Sharma, Phys. Rev. C **85**, 014609 (2012); K. Sandhu, M. K. Sharma and R. K. Gupta, Phys. Rev. C **85**, 024604 (2012).

[9] R. K. Gupta, M. Balasubramanium, R. Kumar, N. Singh, M. Manhas, and W. Greiner, J. Phys. G: Nucl. Part. Phys. **31**, 631 (2005);R. K. Gupta, M. Manhas, W. Greiner, Phys. Rev. C **73**, 054307 (2006).

[10] M. K. Pradhan, A. Mukherjee, P. Basu, A. Goswami, R. Kshetri, S. Roy, P. R. Chowdhury, M. S. Sarkar, R. Palit, V. V. Parkar, S. Santra and M. Ray, Phys. Rev. C **83**, 064606 (2011).

[11] M. Mazzocco, C. Signorini, D. Pierroutsakou, T. Glodariu *et al.* Phys. Rev. C **82**, 054604 (2010).

[12] M S Gautam, N. Grover, and Manoj K. Sharma, Eur. Phys. J. A **53**, 12 (2017).

[13] N. Grover, K. Sandhu, Manoj K. Sharma, Nucl. Phys. A **974**, 56-71 (2018).

[14] L.F. Canto, P.R.S. Gomes, R. Donangelo, J. Lubian, M.S. Hussein Physics Reports **596**, 1-86 (2015).

[15] K. E. Rehm, H. Esbensen, C. L. Jiang, B. B. Back, *et al.*, Phys. Rev. Lett. **81**, 16 (1998).

[16] P. R. S. Gomes, J. Lubian, L. F. Canto, D. R. Otomar, *et al.*, Few-Body Syst. **57**, 165 - 176 (2016).

[17] N. Takigawa and H. Sagawa, Phys. Lett. B **265**, 23 (1991).

[18] M. S. Hussein, M. P. Pato, L. F. Canto and R. Donangelo, Phys. Rev. C **46**, 377 (1992).

[19] M. S. Hussein, M. P. Pato and A. F. R. de Toledo Piza, Phys. Rev. C **51**, 846 (1995).

[20] L. F. Canto, R. Donangelo, P. Lotti and M. S. Hussein, Phys. Rev. C **52**, R2848 (1995).

[21] C. H. Dasso and R. Donangelo, Phys. Lett. B **276**, 1 (1992).

[22] C. H. Dasso and A. Vitturi, Phys. Rev. C **50**, R12 (1994).

[23] E. F. Aguilera, J. J. Kolata, F. D. Becchetti, P. A. D.Young, J. D. Hinnefeld, A. Horvth, L. O. Lamm, Hye-Young Lee, D. Lizcano, E. Martinez-Quiroz, P. Mohr, T. W. O. Donnell, D. A. Roberts, and G. Rogache, Phys. Rev. C **63**, 061603 (2001).

[24] J. J. Kolata, V. Guimares, D. Peterson, P. Santi, R. White-Stevens, P. A. D. Young, G. F. Peaslee, B. Hughey, B. Atalla, M. Kern, P. L. Jolivette, J. A. Zimmerman, M. Y. Lee, F. D. Becchetti, E. F. Aguilera, E. Martinez-Quiroz, and J. D. Hinnefeld, Phys. Rev. Lett. **81**, 4580 (1998).

[25] M. Trotta, J. L. Sida, N. Alamanos, A. Andreyev, F. Auger, D. L. Balabanski, C. Borcea, N. Coulier, A. Drouart, D. J. C. Durand, G. Georgiev, A. Gillibert, J. D. Hinnefeld, M. Huyse, C. Jouanne, V. Lapoux, A. Lpine, A. Lumbroso, F. Marie, A. Musumarra, G. Neyens, S. Ottini, R. Raabe, S. Ternier, P. V. Duppen, K. Vyvey, C. Volant and R. Wolski, Phys. Rev. Lett. **84**, 2342 (2000).

[26] M. Dasgupta, P. R. S. Gomes, D. J. Hinde, S. B. Moraes *et al.* Phys. Rev. C **70**, 024606 (2004).

[27] S. P. Hu, G. L. Zhang, J. C. Yang, H. Q. Zhang, *et al.*, Phys. Rev. C **91**, 044619 (2015).

[28] M. S. Gautam, Phys. Scr. **90**, 125301 (2015).

[29] J. J. Kolata, V. Guimarães, D. Peterson, P. Santi, *et al.* Phys. Rev. Lett. **81**, 4580 (1998).

[30] M. Trotta, J. L. Sida, N. Alamanos, A. Andreyev, *et al.*, Phys. Rev. Lett. **84**, 2342 (2000).

[31] J. F. Liang and C. Signorini, Int. J. Mod. Phys. E **14**, 1121 (2005).

[32] P R S Gomes, I Padron, J O Fernández Niello, G V Martí *et al.* J. Phys. G: Nucl. Part. Phys. **31**, S1669-S1673 (2005).

[33] L. F. Canto, P. R. S. Gomes, R. Donangelo, and M. S. Hussein, Phys. Rep. **424**, 1 (2006).

[34] N. Keeley, R. Raabe, N. Alamanos, J.L. Sida, Prog. Part. Nucl. Phys. **59**, 579 (2007).

[35] E. F. Aguilera, E. Martinez-Quiroz, D. Lizcano, A. Gomez-Camacho *et al.* Phys. Rev. C **79**, 021601(R) (2009).

[36] N. Keeley, N. Alamanos, K.W. Kemper, K. Rusek Prog. Part. Nucl. Phys. **63**, 396 (2009).

[37] M. Mazzocco Int. J. Mod. Phys. E **19**, 977 (2010).

[38] R. Morlock, R. Kunz, A. Mayer, M. Jaeger *et al.* Phys. Rev. Lett. **79**, 3837 (1997).

[39] N. J. Davidson, S. S. Hsiao, J. Markram, H. G. Miller, Y. Tzeng, Nucl. Phys. A **570**, 61c (1994).

[40] M. Bansal, Raj Kumar, and Raj K. Gupta, Journal of Physics: Conference Series **321**, 012046 (2011).

[41] P. R. S. Gomes, J. Lubian, I. Padron, and R. M. Anjos *et al.*, Phys. Rev. C **71**, 017601 (2005).

[42] M. Mazzoccoa, A. Boiano, C. Boiano, A. Di Pietro *et al.*, Nucl. Phys. A **834**, 488c (2010).

[43] E. Strano, D. Torresi, M. Mazzocco, N. Keeley, *et al.*, Phys. Rev. C **94**, 024622 (2016).

[44] N. Keeley, J.A. Christley, N.M. Clarke, B.R. Fulton *et al.*, Nucl. Phys. A **582**, 314 (1995).

[45] N. Keeley, J.S. Lilley, J.X. Wei, M. Dasgupta *et al.*, Nucl. Phys. A **628**, 1 (1998).

[46] N. Grover, G. Kaur, and M. K. Sharma Proceedings of the DAE-BRNS Symp. on Nucl. Phys. **61**, 586 (2016).

Chapter 5

Addressal of Fusion fission and deep inelastic collision

In previous chapters, the compound nucleus mechanisms were explored in context to different compound nuclei $^{74}Kr^*$, $^{75}Rb^*$, $^{118,120,122}Xe^*$, $^{161}Dy^*$ and $^{165}Er^*$. So far the dynamics of reactions involving both loosely and tightly bound projectiles have been investigated in DCM framework. The comparative analysis of decay profiles associated with CF and ICF processes was also presented for ^{6}Li + ^{159}Tb and ^{17}F + ^{58}Ni reaction. Also, the role of deformations, orientations, excitation energy, angular momentum, and iso-spin (N/Z ratio) was investigated in the decay of different compound nuclei. After exploring the compound nucleus mechanisms, DCM [1–7] has been employed to study the non compound nucleus (nCN) processes, in which the composite system dissociates before achieving the fully equilibrated state of compound nucleus. The present chapter aims to investigate the contribution of nCN process in light mass region of the periodic table. Here, the compound system $^{47}V^*$ formed in ^{20}Ne + ^{27}Al reaction is considered to investigate the comparative contribution of fusion fission (FF) and deep inelastic collision (DIC), where FF represents the CN component and DIC lies in the category of nCN process. It is relevant to mention here that DIC is the most commonly observed nCN process in the light mass region. Calculations are made over a wide energy span ($E_{c.m.}$=83-125 MeV), in reference to the

experimental data of Dey *et al.* [8]. The results of this study are published in [9]. A brief introduction associated with present study is given in the following section Sec. 5.1. The calculations and results are presented in Sec. 5.2 and finally the summary and conclusions are briefed in Sec. 5.3.

5.1 Introduction

In last few decades, collisions involving heavy ions forming compound nucleus in light mass region ($A_{CN} \leq 80$) have been studied extensively [10–15]. The study regarding the decay of compound nucleus having mass in the mentioned region, provide a lot of interesting opportunities to analyze competing compound nucleus formalisms such as evaporation residues (ER)($A_2 \leq 4$), intermediate mass fragments (IMF)($5 < A_2 < 20$), heavy mass fragments (HMF)($20 < A_2 < \frac{A_{CN}}{2} - 20$) and fusion fission (FF)($\frac{A_{CN}}{2} - 20 \leq A_2 \leq \frac{A_{CN}}{2} + 20$) etc. along with some non compound nucleus paths. Collisions or fusion processes forming the composite systems in the specified region may invite various nCN or exotic processes like quasi elastic (QE), deep inelastic (DI) processes. Our main focus here is to address FF and DIC mechanism. The exercise concerning such type of nuclear reactions may provide some important input to investigate the mononuclear or di nuclear system more precisely [16]. Many reactions from this region like $^{16}O + ^{27}Al$, $^{16}O + ^{28}Si$, $^{20}Ne + ^{27}Al$, $^{20}Ne + ^{59}Co$ [17], $^{20}Ne + ^{20}Ne$, $^{20}Ne + ^{16}O$ [18], $^{20}Ne + ^{12}C$ [19], $^{16}O + ^{12}C$ [20] etc. have been examined in last few years. Information extracted from above mentioned reactions unfold distinctive interesting aspects about the formation and decay of nuclear system. As mentioned above, the well known forms of decay modes of compound nucleus are ER, IMF, HMF and fission. But there are distinctive parameters like energy, mass, angular momentum etc. which inhibit these decay channels because of some competing anomalous processes. It is found that for lighter nuclei at energy much higher than the Coulomb barrier, the compound nucleus dissipate enormous component of its own mass and in this decay process, fragments possessing mass comparable to projectile or target come out with highest probability [18]. Apart from energy, in some cases the structure

of the colliding nuclei has been observed to play crucial role. Reactions ^{20}Ne + ^{12}C [21], ^{24}Mg + ^{12}C [22], and ^{28}Si + ^{12}C [23] have α cluster amalgamating nuclei and inquisition on these reactions demonstrate that excitation functions of the outgoing channel are similar to entrance channel, which is an explicit indication of the presence of deep inelastic collisions (DIC). Deep inelastic collisions are defined as the phenomenon which maintains the memory of incoming channel and form a dinuclear molecular complex system, which subsequently decays into target and projectile like fragments which inturn contribute towards DIC cross sections, σ_{DIC}. In addition to mass, energy and structure, the angular momentum (ℓ) also play very important role. It is to be noted that the reactions yields corresponding to DIC occur mainly due to some of the partial waves near grazing angular momentum [24].

Deep-inelastic transfer reactions are generally inspected at impact parameter smaller than grazing at sufficiently high energy so that the angular momentum of these orbits exceeds the critical value [25]. The peculiarity of DIC is an enthusiastic subject to study for considerable number of reasons. One of the most important reason is that it is an intermediate process in compound nucleus formation and direct reaction mechanism. Here, the kinetic energy degrees of freedom are equilibrated and di nuclear composite system is formed, while the remembrance of the entrance channel is maintained [25]. The di nuclear system formed accomplish equilibration via subsequent emission of IMFs or cluster(s). To distinct these two processes (FF and DIC) for nuclei having fissility less than Businaro-Gallone point [26,27], is not an easy task for experimentalists and theoreticians.

Many efforts have been done by the scientists to identify the DIC and FF exclusively in nuclear reactions such as Shapira *et al.* [18] using Oak ridge isochronous Cyclotron for ^{20}Ne + ^{20}Ne, ^{20}Ne + ^{16}O. Bhattacharya *et al.* at variable energy cyclotron center examined ^{16}O + ^{27}Al using nonlinear optimization procedure [28]. Besides this, Dey *et al.* [19] and Van Sen *et al.* [29] also explained the DIC process respectively in ^{20}Ne + ^{12}C and ^{20}Ne + ^{40}Ca reactions and Agassi [30] and Ko [31] explained the transport theory of deeply inelastic heavy ion collisions based on random matrix model. In extension of above, some

theoretical models e.g. phenomenological model for two-body friction force [32], theory of Lindblad [33] for open quantum systems, diffusion model [34] etc. have been proposed to interpret such kind of exotic processes. Apart from above theories and models, we use Dynamical Cluster-decay Model (DCM) [1–7] to address such phenomenon. DCM has been practiced in some reactions [35, 36] to analyze deep inelastic collisions or orbiting processes and few other exotic processes, besides having extensive applications in the addressal of compound nucleus dynamics. Additionally, it has successfully explained the fragment emission of light mass compound nuclei ^{31}P, ^{32}S, ^{39}K, ^{48}Cr, ^{56}Ni, ^{66}As [1,2,35–37] etc.

Here, an effort is made to examine the decay of ^{47}V* formed through ^{20}Ne + ^{27}Al reaction using DCM. The decay of this peculiar compound nucleus has been studied extensively using both symmetric and asymmetric entrance channels [38–46]. Decay of ^{47}V* formed in inverse kinematics [38–42] show that it disintegrates through FF. On the other hand same compound nucleus formed in direct kinematics [8, 43–45] might include the presence of DIC. The present work is constrained to the decay of ^{47}V* formed in one of the direct kinematics reaction.The calculations are done in context to the experimental data of [8]. It has been observed that there exist two possible decay modes (FF and DIC) for ^{47}V*. Thus, both FF and DIC cross-sections are addressed in the present work. These processes are different from each other in view of compound nucleus formation and angular momentum dependence. The FF cross sections contribute in ℓ-window ($0 \leq \ell \leq \ell_{cr}$) whereas, DIC cross sections contribute in $\ell_{cr} < \ell \leq \ell_{gr}$ window. In present work, calculations are done using quadrupole (β_{2i}-deformed) choice of fragments by taking optimum orientations and coplanar collisions. Here, only coplanar ($\phi = 0$) degree of freedom is exercised, considering the fact that difference observed in results obtained through coplanar and non-coplanar ($\phi \neq 0$) interactions is small as shown in [47–49]. The quantities like fragmentation potential, preformation probability, scattering potential, penetrability and emission time etc. have been scrutinized in the framework of DCM. The calculations and results are presented in the following section.

5.2 Calculations and results

This section describes the calculations and results attained for the decay of $^{47}V^*$ formed in $^{20}Ne + ^{27}Al$ reaction over wide energy range ($E_{c.m.}$ = 83-125 MeV). As stated in section 5.1, there are two feasible disintegration modes of $^{47}V^*$ formed in $^{20}Ne + ^{27}Al$ reaction. One of the decay channel fusion-fission follows the compound nucleus path, whereas the Deep inelastic collision lies in category of non compound nucleus (nCN) process. Firstly, FF is studied by using collective clusterization approach of DCM by calculating fragmentation potential, preformation probability, penetrability and scattering potential etc. Some of these quantities provide significant information regarding the nuclear structure effects and hence provide an opportunity to identify the most favorable fragments in the decay of $^{47}V^*$. Secondly, DIC is studied by dissociating preformation probability (P_0=1), equally among the most contributing fragments in the emission channel. In addition, the summed up cross sections of most favorable fragments having charge in the range of ($3 \leq Z \leq 9$) are calculated for both FF and DIC. Finally, the emission time of DIC fragments is estimated along with their penetration probability analysis. It may be noted that the range of partial waves of angular momentum for FF and DIC is "$0 \leq \ell \leq \ell_{cr}$" and "$\ell_{cr} < \ell \leq \ell_{gr}$" respectively. All observations and results shown in this section are for β_{2i}-deformed choice of fragments.

Firstly, to examine the comparative contribution of fragments in case of FF, behavior of fragmentation potential is analyzed. Fig. 5.1 depicts the behavior of fragmentation potential ($V(\eta)$) as a function of fragment mass at minimum and maximum center of mass energies in given energy range ($E_{c.m.}$∼83-125 MeV) at two extreme angular momentum values i.e. at ℓ=0 $\hbar$ and ℓ=ℓ_{cr}. It is apparently evident from the Fig. 5.1 that the overall structure of potential energy surfaces remains same at the extreme energies hence, one can say that the fragmentation structure effects are silent in the considered range of incident energies. Although, there is no evident effect of energy on the structure of potential energy surfaces but the magnitude of fragmentation potential increases with

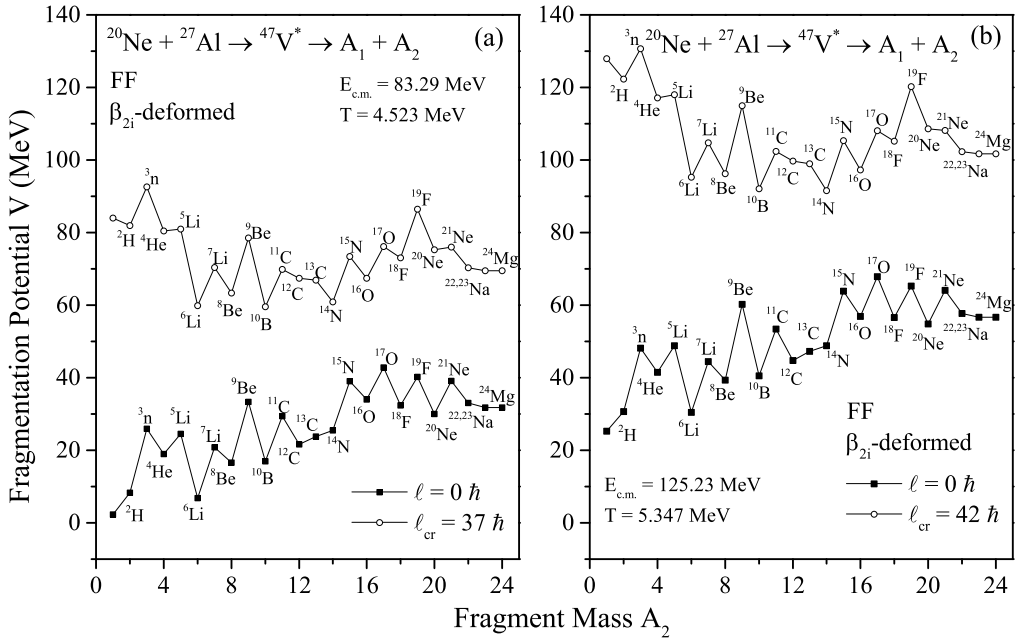

Figure 5.1 Fragmentation potential V (MeV) as a function of fragment mass for fusion fission (FF) type of decay channel plotted at (a) $E_{c.m}$=83.29 and (b) $E_{c.m}$=125.23 MeV at two extreme angular momentum values (ℓ=0 and ℓ_{cr}) for β_{2i}-deformed (i=1,2) choice of fragments.

the increase in incident energy, possibly due to the corresponding increase in critical angular momentum. As behavior of fragmentation potential is shown at extreme angular momentum values, so it is worth to discuss the ℓ-effect on fragmentation structure. The overall structure at both ℓ-values i.e. at ℓ=0 and ℓ_{cr} is quite different and the magnitude increases with increase in angular momentum. The fragments with Z=3 to 9 contribute less at lower ℓ-states and then start dominating the evaporation residue and symmetric fission fragments at higher ℓ-values, almost independent of the incident energy used. In DCM, it has been observed [6, 7] that the minima in fragmentation potential signify the maxima in preformation probability hence, fragments possessing minima in Fig. 5.1 are more favorable as emitting fragments. A careful look of potential energy surfaces reveals that the most dominant minima lie in territory of charge varying from 3 to 9. Further, inspecting the structure at extreme ℓ-values, one may recognize that the fragments having equal number of protons and neutrons (N=Z) are more favorable as compare to N≠Z fragments except for ^{12,13}C fragments. Isotopes of carbon (^{12,13}C) show different trend

at extreme ℓ-values i.e. at ℓ=0, ^{12}C is possessing minima but near $\ell = \ell_{cr}$, ^{12}C starts competing with ^{13}C fragment. This type of behavior of ^{12,13}C made us curious to analyze which of them contribute most in the decay of $^{47}V^{*}$ nucleus. To explore this, summed up fragmentation potential from $0 \leq \ell \leq \ell_{cr}$ is plotted for all fragments as shown in Fig. 5.2. Summed up fragmentation potential determines the contribution of fragments more precisely as it includes the effect of all partial waves. One can see from the Fig. 5.2 that behavior of summed up fragmentation potential is almost identical as that of behavior of fragmentation potential at individual angular momentum with some minor variation. The minima here lies for same fragments, on which it lie in Fig. 5.1(a) and (b). Also, the anomaly of ^{12,13}C fragments at two extreme angular momenta is resolved, as evident from the potential dip for ^{12}C fragment as shown in Fig. 5.2. In this figure, ^{12}C seems to possess minima at both the energies and hence we can say that, fragments having N=Z are the prominent contributors towards decay cross sections, other isotopes with N$\neq$Z shown in Fig. 5.2 also contribute, but with lesser probability. All the contributing isotopes with their mass number (A) are shown and identified in Fig. 5.1 and 5.2. It is worth reminding that the fragmentation potential serves as an important input in solving the stationary Schrödinger wave equation (in terms of η coordinates) (refer Eq. (2.6) of chapter 2) which further give rise to the preformation probability P_0 as discussed in Sec. 2.5 of chapter 2.

The preformation probability is calculated using collective clusterization approach of DCM for the binary fragments as shown in Fig. 5.3. It shows the P_0 trend of all possible fragments at two extreme values of energies and angular momentum, (ℓ=0 and ℓ_{cr}), for quadrupole choice of fragmentation. Before proceeding further, it is important to note that the critical angular momentum is always less than that of liquid drop limit of angular momentum where the fission barrier actually vanishes [16]. This is also in agreement with the experiments by Morgenstern and Lehr *et al.* [46]. However, it is found that at ℓ=ℓ_{cr}, the data obtained is in agreement with the prediction of modified version of LDM [16]. Hence, the calculations for FF are done upto ℓ_{cr}. Furthermore, the most probable emitting

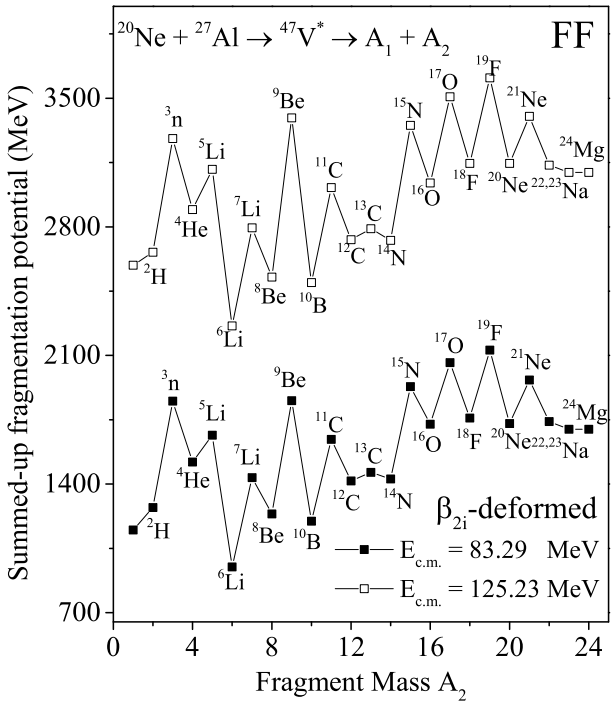

Figure 5.2 Summed up fragmentation potential V (MeV) (for all partial waves of angular momentum) as a function of fragment mass for Fusion Fission (FF) type of decay channel plotted at $E_{c.m}$=83.29 and 125.23 MeV for β_{2i}-deformed (i=1,2) choice of fragments.

fragments through decay of $^{47}V^{*}$ at ℓ=0 and ℓ_{cr} are identified and are marked in Fig. 5.3. One may notice here that the most contributing fragments identified in Fig. 5.3 keep their identity independent of incident energy and ℓ-values used in both cases depicted as Fig. 5.3(a) and (b). Further, a careful inspection of Fig. 5.3 indicates that at ℓ=ℓ_{cr}, the probability of fragments with charge number from "$3 \leq Z \leq 9$" ($5 \leq A_2 \leq 19$) is higher as compare to others at both the energies. However, at ℓ=0 $\hbar$, particles with Z$\geq$7 possess lesser probability as compare to at ℓ=ℓ_{cr}. Also, the preformation probability of fission region ($10 \leq Z \leq 11$; $20 \leq A_2 \leq 23$) is very low at lower angular momentum and becomes significant at ℓ=ℓ_{cr}. In other words, the contribution of fission fragment increases with increase in angular momentum. This trend of preformation probability with fragment mass make us curious to know about the finally contributing fragments in fusion fission. For this, the emitting fragments are divided into three regions according to their charge number: $0 \leq Z \leq 2$, $3 \leq Z \leq 9$ and $10 \leq Z \leq 11$. These three regions include all

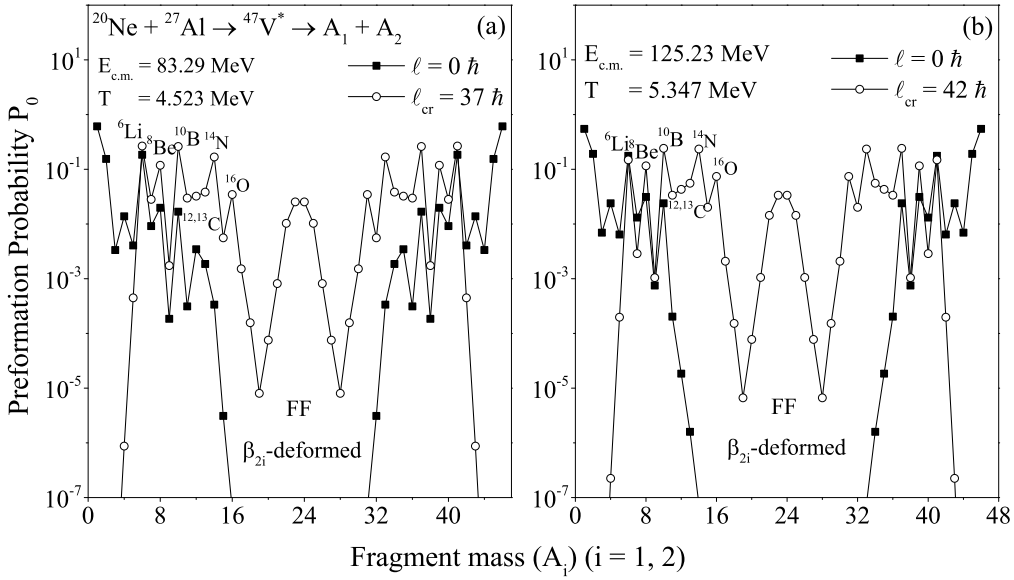

Figure 5.3 Preformation probability (P_0) as a function of fragment mass for Fusion Fission (FF) type of decay channel plotted at (a) $E_{c.m}$=83.29 and (b) $E_{c.m}$=125.23 MeV at two extreme angular momentum (ℓ=0 and ℓ_{cr}) for β_{2i}-deformed (i=1,2) choice of fragments.

possible isotopes associated with respective charge number. Subsequently, the summed up preformation probability (P_0) for these three charge regions is plotted as a function of angular momentum at lowest center of mass energy ($E_{c.m}$ = 83.29 MeV) upto ℓ_{cr} as depicted in Fig. 5.4. It can be seen that the territory with charge "$10 \leq Z \leq 11$" has negligible preformation probability at all ℓ-values due to which the anticipation of these clusters in dominant emitting channel becomes inconsequential. The other two regions seem to compete with each other. The summed up preformation probability is higher for "$0 \leq Z \leq 2$" upto certain value ($\ell \sim 15\hbar$) of angular momentum but decreases with increasing ℓ-values. At $\ell > 15\hbar$, the contribution of charge ($3 \leq Z \leq 9$) fragments start increasing, but a precise analysis of Fig. 5.4 reveals that the minima in $\sum P_0$ for "$3 \leq Z \leq 9$" at $\ell \simeq 0\hbar$ is higher in magnitude than the minimal point of $\sum P_0$ for "$0 \leq Z \leq 2$" at $\ell \geq 32\hbar$. Shifting towards the discussion of higher magnitude of summed up preformation probability, the maxima of $\sum P_0$ for "$3 \leq Z \leq 9$" at $\ell \geq 32\hbar$ is higher in magnitude than the maximal point of summed up preformation probability for "$0 \leq Z \leq 2$" at $\ell \simeq 0\hbar$. Also, the region "$3 \leq Z \leq 9$" is dominant at higher ℓ-values

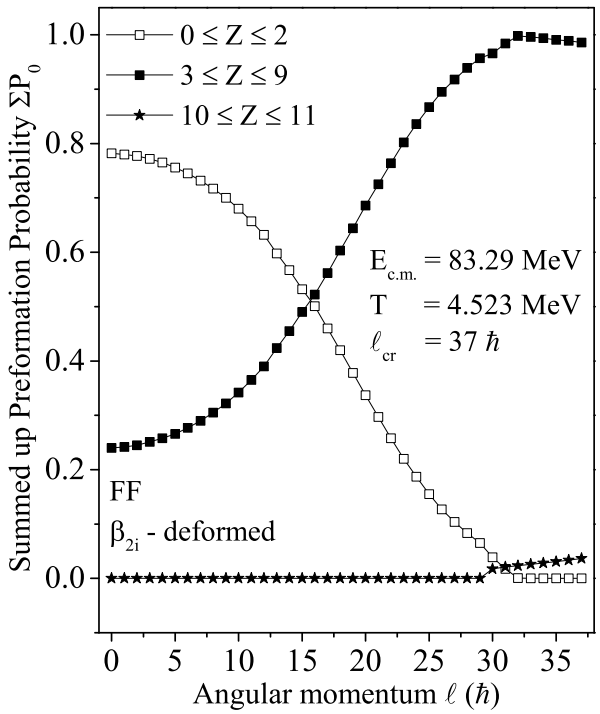

Figure 5.4 Summed up preformation probability ($\sum P_0$) as a function of angular momentum (ℓ) for Fusion Fission (FF) decay channel of ^{20}Ne+^{27}Al$\rightarrow^{47}$V* reaction plotted at E$_{c.m}$=83.29 MeV for β_{2i}-deformed (i=1,2) choice of fragments.

in comparison to that of "$0 \leq Z \leq 2$" region of charge fragments, with a relatively wider ℓ-window for the earlier case. Therefore, one can say that the overall contribution in FF decay is due to charge fragments with Z = 3 to 9, which is also in accordance with the available experimental data [8]. The equivalent behavior is observed at higher center of mass energy (E$_{c.m.}$=125.23 MeV) also (not shown here). After analyzing the above results, the further analysis is confined on the fragments lying in $3 \leq Z \leq 9$ region only.

In addition to preformation probability, penetration probability (penetrability, P) is likewise an important component in calculation of decay cross sections (see Eq. 2.43 of chapter 2). Thus, variation of penetrability with increasing angular momentum upto critical one (ℓ_{cr}) is plotted at extreme center of mass energies (E$_{c.m.}$=83.29 and 125.23 MeV) and the results are presented in Fig. 5.5. The barrier penetrability is plotted for the most probable fragments (with $3 \leq Z \leq 9$), having equal number of protons and neutrons (N=Z). Fig. 5.5 illustrates that there is negligible magnitude of penetrability upto $\ell \sim 23\hbar$

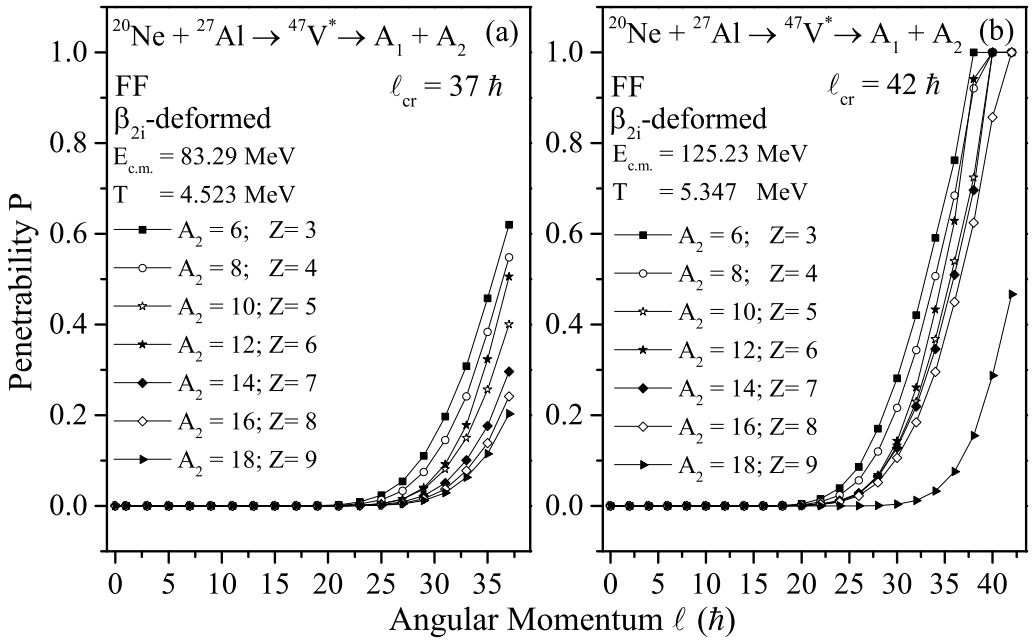

Figure 5.5 Dependence of penetration probability (P) on angular momentum (ℓ) for Fusion Fission (FF) decay channel at (a) $E_{c.m}$=83.29 and (b)$E_{c.m}$=125.23 MeV for selected charge fragments ($3 \leq Z \leq 9$) for β_{2i}-deformed (i=1,2) choice of fragments.

and farther increases with increase in angular momentum at both energies. Also, it seems that there is increment in "P" with increase in center of mass energy, which might be owing to the fact that with increase in energy, critical ℓ-value increases (ℓ_{cr}=37 $\hbar$ and 42 $\hbar$ at $E_{c.m.}$=83.29 and 125.23 MeV respectively) which results in contribution of more partial waves with rise in energy. At maximum energy, penetrability approaches almost equivalent to one at higher angular momentum for all fragments except the heaviest one ^{18}F. Other observation from the Fig. 5.5 is that with an accretion in charge and mass number, the magnitude of penetrability decreases at both energies. This result is in accordance with [35]. However, there is one fragment (^{12}C) which does not follow this trend. According to change in variation of penetrability with charge and mass, value of "P" for $^{12}_{6}$C should be less than that of the $^{10}_{5}$B, but Fig. 5.5 clearly shows that it is greater for $^{12}_{6}$C. This behavior of $^{12}_{6}$C may be due to the observation retrieved from Fig. 5.1. The information about concerned isotope revived from Fig. 5.1 is that, at lower ℓ-values, ^{13}C (with N $\neq$ Z) is more probable as compare to ^{12}C (with N=Z) but the situation get

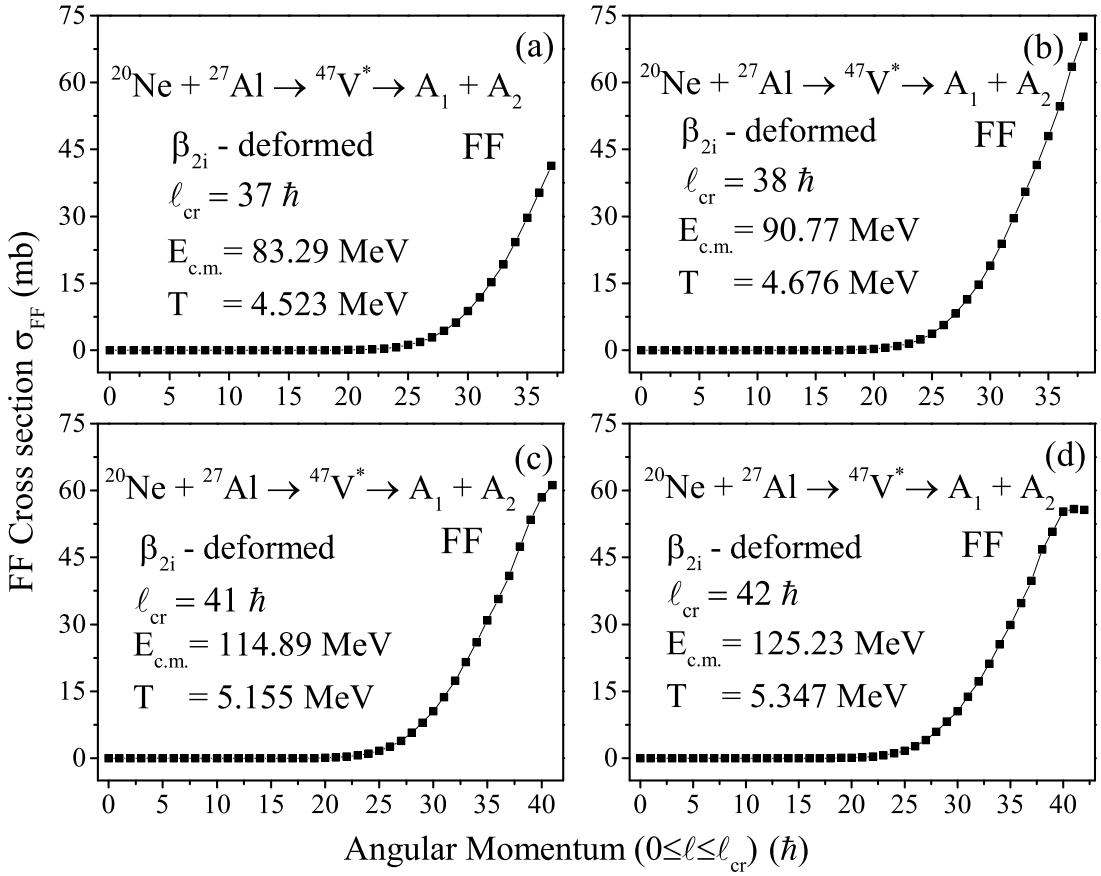

Figure 5.6 Fusion Fission (FF) cross sections as function of angular momentum ($0 \leq \ell \leq \ell_{cr}$) at all center of mass energies (a) $E_{c.m.}$=83.29 MeV, (b) $E_{c.m.}$=90.76 MeV, (c) $E_{c.m.}$=114.89 MeV and (d) $E_{c.m.}$ = 125.23 MeV for quadrupole (β_{2i}-deformed) choice of fragments.

Table 5.1 The total FF and DIC cross sections ($3 \leq Z \leq 9$) for $^{47}V^*$ formed in ^{20}Ne + ^{27}Al reaction channel calculated using DCM for quadrupole (β_{2i}-deformed) (i=1,2) choice of fragments in given center of mass energy range ($E_{c.m.}$∼83-125 MeV) compared with the experimental data [8]. Also, the temp., angular momentum and neck length parameter (ΔR) are shown.

S.No.	E_{lab} (MeV)	E^*_{CN} (MeV)	$E_{c.m.}$ (MeV)	T (MeV)	ℓ_{crit} (ħ)	ℓ_{graz} (ħ)	FF ΔR (fm)	FF σ_{DCM} (mb)	FF $\sigma_{Exp.}$ (mb)	DIC ΔR (fm)	DIC σ_{DCM} (mb)	DIC $\sigma_{Exp.}$ (mb)
1	145.00	102.03	83.29	4.523	37	49	1.604	204	205.5	0.730	130.0	133.4
2	158.00	109.51	90.76	4.676	38	52	1.783	435	438.1	1.130	488.0	489.5
3	200.00	133.64	114.89	5.155	41	60	1.825	441	443.7	0.600	449.0*	437.2
4	218.00	143.98	125.23	5.347	42	63	1.891	482	480.9	0.600	596.0*	567.5

* These cross sections are calculated upto ℓ_{gr}-4.

reversed with increase in angular momentum. Further, it is also interesting to note that similar kind of behavior for ^{12}C has been observed in the decay of ^{48}Cr [2]. Now, stepping ahead, the two types of probabilities discussed above i.e. preformation probability "P_0" and penetrability "P" which provide essential inputs in DCM to estimate the decay cross sections, an endeavour is made to address and predict the decay cross sections.

The effect of angular momentum on fusion fission cross sections (σ_{FF}) over an extensive range of center of mass energies ($E_{c.m.}$=83.29 - 125.23 MeV) is exhibited in Fig. 5.6. Before proceeding further, it is worth mentioning here that FF cross sections estimated using DCM consist of the contribution of fragments with charge varying as $3 \leq Z \leq 9$ only, and the variation of σ_{FF} with angular momentum is depicted in Fig. 5.6. The fusion fission process results due to partial waves of angular momentum only upto their critical value, hence the behavior of σ_{FF} is shown for the same ℓ-window. It is observed from the figure that the magnitude of cross sections upto $\ell \sim 23\hbar$ is approximately equals to zero for all the energies. Fig. 5.6 seems to confirm that the major part of σ_{FF} lie in angular momentum window varying as "$24 \leq \ell \leq \ell_{cr}$". The FF cross sections calculated using DCM along with their ℓ-values, ΔR, and temp. etc. are shown in Table.5.1 of present section.

Next, we present the results related to DIC path observed in the decay of ^{47}V* formed in ^{20}Ne + ^{27}Al reaction [8]. As discussed in Sec. 5.1, the decay of ^{47}V* formed through above mentioned reaction, might include the possibility of nCN process in reference to the data of [8]. It is found that there is a strong competition between fusion fission and deep inelastic collision (DIC) in decay of ^{47}V* composite system formed in ^{20}Ne + ^{27}Al reaction. Therefore, an attempt has been made to analyze DIC contribution using DCM as an extension of our previous work [35].

Now, to differentiate fusion fission (FF) and deep inelastic collision (DIC), the scattering potential V(R) is plotted as a function of internuclear distance, R(fm) for both FF and DIC at different values of angular momentum lying in the vicinity of their contributing ℓ-values ($0 < \ell \leq \ell_{cr}$ for FF and $\ell_{cr} < \ell \leq \ell_{gr}$ for DIC). Fig. 5.7(a) presents the scatter-

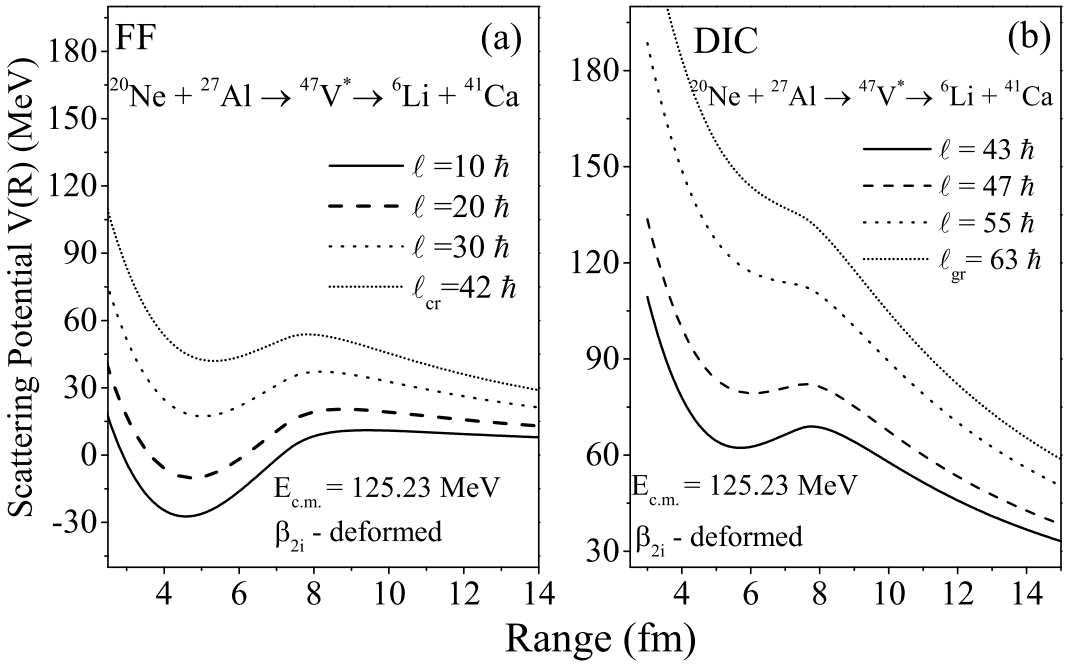

Figure 5.7 Variation of scattering potential V(R) (sum of V_P, V_C and V_ℓ) as function of range for (a) Fusion Fission (FF) and (b) Deep inelastic collision (DIC) at maximum center of mass energy ($E_{c.m.}$=125.23 MeV) for β_{2i}-deformed (i=1,2) choice of fragments.

ing potential of FF varying with "R" for different values of angular momentum upto ℓ_{cr} taking ^{6}Li + ^{41}Ca as the outgoing channel at maximum energy ($E_{c.m.}$ =125.23 MeV). It is clearly evident from the figure that with increase in angular momentum, the pocket of potential barrier becomes more shallow but still exist upto critical angular momentum. On the other hand, the behavior of potential barrier for another channel (DIC) is depicted in Fig. 5.7(b) for different angular momentum values varying as "$\ell_{cr} < \ell \leq \ell_{gr}$" for the same emission channel and energy as that of FF. It is observed from Fig. 5.7(b) that the barrier starts vanishing with rise in angular momentum and almost disappears at grazing angular momentum (ℓ_{gr}). The Figs. 5.7 (a) and (b) demonstrate that the pocket of barrier becomes shallow for FF but barrier does not vanish for the same. On the contrary, for other decay mode (DIC), it disappears at higher partial waves near the grazing angular momentum. Therefore, it can be concluded that the main difference between the FF and DIC lies in the behavior of their potential barriers. The disappearance of barrier

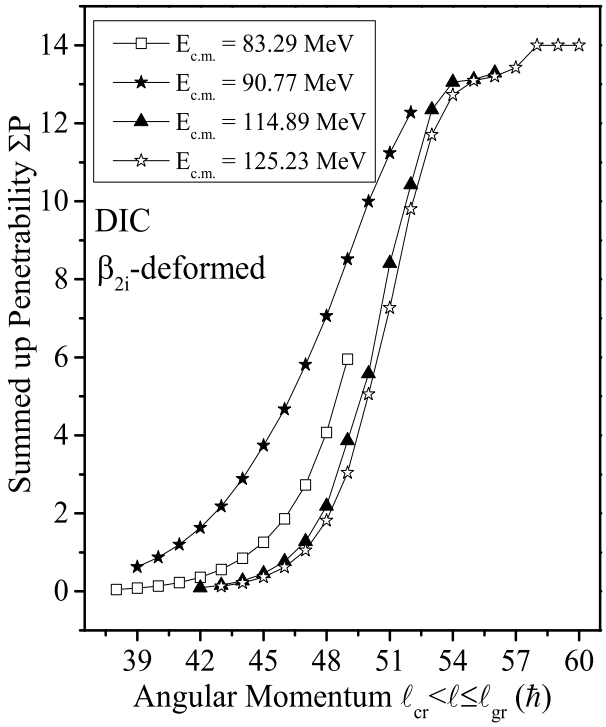

Figure 5.8 Summed up penetration probability for all most probable charge fragments ($3 \leq Z \leq 9$) as a function of angular momentum ($\ell_{cr} < \ell \leq \ell_{gr}$) at all center of mass energies varying from $E_{c.m.}\sim$ 83-125 MeV decaying via Deep inelastic collision (DIC) choice of decay for ^{20}Ne+^{27}Al$\rightarrow^{47}$V* reaction using β_{2i}-deformed (i=1,2) choice of fragments.

pocket in the case of DIC at near grazing angular momentum indicates that the nucleus is not getting trapped inside the pocket, and hence its penetrability at and around ℓ_{gr} approaches to one for DIC. Same behavior is observed for other outgoing channels and incident energies (not shown here to avoid the repetition).

As the barrier properties provide crucial inputs regarding the penetration path of the fragments involved in the decay process. So, after inquisition of scattering potential and barrier characteristics, the barrier penetrability results are discussed ahead. Here, the summed up penetrability ($\sum_{Z=3}^{9}$P) for all isotopes with charge number varying from Z=3 to 9 is plotted as a function of angular momentum ($\ell_{cr} < \ell \leq \ell_{gr}$) in Fig. 5.8. One may notice from the figure that with increment in angular momentum, the penetrability increases at all the energies. This information overlays with the observation extracted from Fig. 5.5 that magnitude of "P" increases due to rise in ℓ-value for fusion fission process. The

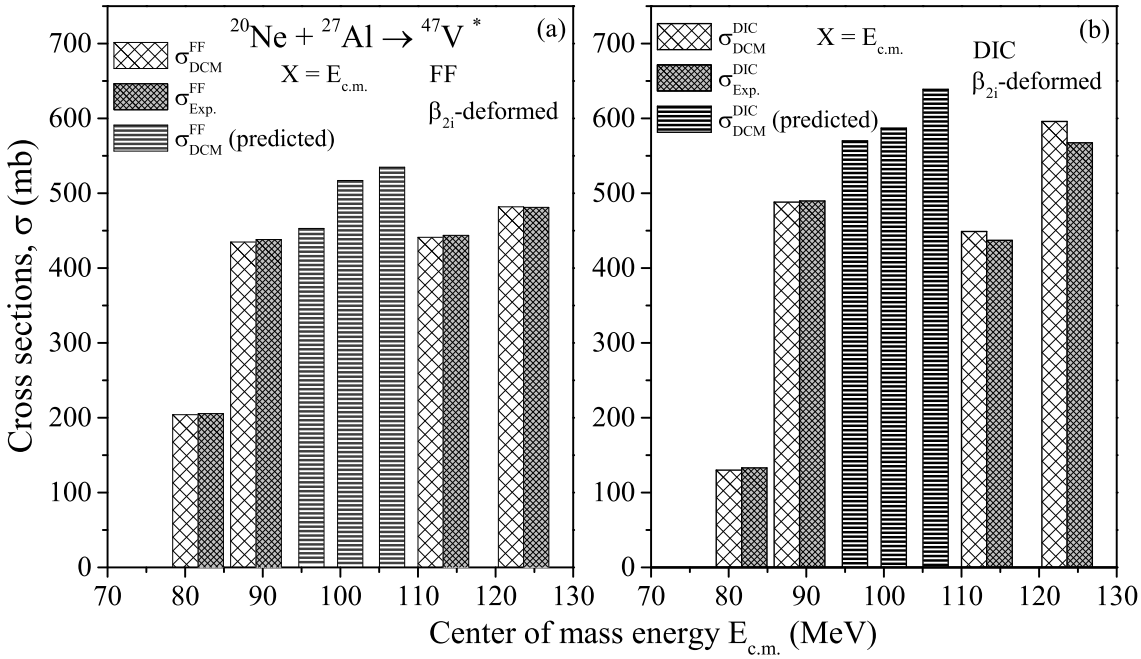

Figure 5.9 Summed up charge ($3 \leq Z \leq 9$) cross sections plotted as function of center of mass energies for both type of decays (a) Fusion Fission (FF) and (b) Deep inelastic collision (DIC). Also, predicted cross sections at some energies are shown for β_{2i}-deformed (i=1,2) choice of fragments.

order of penetrability can be linked with their associated neck length parameter (ΔR) shown in Table 5.1. It can be seen from the Fig. 5.8 that the order of penetrability is in accordance with the ΔR values shown in the Table 5.1. The neck length parameter used at higher energies ($E_{c.m.}$=114.89 and 125.23 MeV) is same i.e. ΔR = 0.6 fm due to which, penetrability at these energies is almost equivalent. At highest energy ($E_{c.m.}$= 125.23 MeV), the value of grazing angular momentum (ℓ_{gr}=63 $\hbar$) is greater as compare to its value (ℓ_{gr}=60 $\hbar$) at $E_{c.m.}$= 114.89 MeV thus possess slightly higher magnitude of penetrability.

Further, total cross sections resulting due to the charge fragments having Z = 3 to 9 for both type of decay modes FF and DIC are tabulated in Table 5.1 along with their ℓ-values, neck length parameter (ΔR), temperature and other related inputs. The cross sections shown in Table 5.1 are addressed by using single parameter of DCM i.e. neck length parameter. It can be noticed from the table that FF cross sections are in good accordance with the experimental data [8]. For DIC, the cross sections are fitted nicely at

two lower energies within prescribed ℓ-window ($\ell_{cr} < \ell \leq \ell_{gr}$), but at higher two energies, the calculated cross sections overestimate the experimental data even at much lower value of ΔR. However, the cross sections at these energies are addressed in "$\ell_{cr} < \ell \leq \ell_{gr} - 4$" range of angular momentum. This might be due to the presence of some other nCN process at higher ℓ-values. Apart from this, an endeavour is made to predict the cross sections at three more center of mass energies, $E_{c.m.}$=93, 98 and 103 MeV by fitting cubic polynomial for neck length parameter as a function of $E_{c.m.}$ as given below

$$\Delta R_{FF} = (1.947 \times 10^{-5})X^3 - 0.006308X^2 + 0.6786X - 22.399 \tag{5.1}$$

and

$$\Delta R_{DIC} = (7.217 \times 10^{-5})X^3 - 0.02324X^2 + 2.45818X - 84.473 \tag{5.2}$$

respectively for FF and DIC with X=$E_{c.m.}$. The predicted values of cross sections (σ) are represented by bars with dense horizontal lines in Fig. 5.9(a) for FF and Fig. 5.9(b) for DIC.

Next, in order to understand the DIC behavior further, the decay life times of the most favorable emitting fragments are estimated. The Assault/impinging frequency (ν_0), the Preformation factor (P_0) and barrier penetration (P) provide essential inputs to determine the emission time (τ) of outgoing fragments using Eq. 2.46 of chapter 2. The value of preformation probability considered to calculate the decay life time is same as the one used to address the σ_{DIC}, which means that P_0=1 is distributed equally among the most favorable isotopes contributing towards the cross sections. Penetrability and decay life times for all fragments computed using DCM at given center of mass energy range ($E_{c.m.} \sim$ 83-125 MeV) are tabulated in Table 5.2. The calculations are performed at ℓ_{cr} and ℓ_{gr} angular momentum values. Life times at ℓ_{cr} are addressed using a constant neck length parameter (ΔR=1.5 fm) for all energies and fragments. On the other hand at ℓ_{gr}, the ΔR value remains same as that of its value used to compute the σ_{DIC}. One may observe that the emission time at all energies calculated using DCM are in good accordance with the experimental data [8], except for $^{18}_{9}$F. The impinging frequency (ν_0) used to calculate the emission time is computed as per Eq. 2.46, and is found to be nearly constant

Table 5.2 The DCM calculated penetrability and emission time ($\tau_{1/2}$ in sec.) at critical (ℓ_{cr}) as well as grazing (ℓ_{gr}) angular momentum for the most probable fragments ranging from Z=3-9 contributing towards the decay of $^{47}V^{*}$ nucleus. The comparison of emission time at the four given energies is made with the experimental data [8].

		ℓ_{cr}			ℓ_{gr}		
			$\log_{10}\tau_{1/2}$			$\log_{10}\tau_{1/2}$	
S.No.	Fragments	Penetrability	DCM	Experimental	Penetrability	DCM	Experimental
		E_{Lab} = 145 MeV; $E_{c.m.}$=83.29 MeV					
1	Li	0.424	-20.58	-20.68	0.562	-20.82	-20.82
2	Be	0.348	-20.41	-21.22	0.531	-20.71	-21.36
3	B	0.222	-20.15	-21.66	0.284	-20.38	-21.80
4	C	0.291	-20.25	-21.84	0.701	-20.74	-21.98
5	N	0.197	-20.02	-21.95	0.252	-20.22	-22.09
6	O	0.156	-19.88	-22.08	0.170	-20.01	-22.22
7	F	0.010	-18.71	-22.08	0.006	-18.59	-22.22
		E_{Lab} = 158 MeV; $E_{c.m.}$=90.76 MeV					
1	Li	0.450	-20.64	-21.05	0.802	-21.00	-21.20
2	Be	0.373	-20.48	-21.29	0.898	-21.97	-21.44
3	B	0.242	-20.23	-21.46	0.779	-20.86	-21.61
4	C	0.316	-20.32	-21.75	0.720	-20.78	-21.90
5	N	0.214	-20.08	-21.79	0.955	-20.85	-21.94
6	O	0.167	-19.94	-22.89	0.739	-20.71	-22.05
7	F	0.012	-18.79	-22.16	0.194	-20.12	-22.31
		E_{Lab} = 200 MeV; $E_{c.m.}$=114.89 MeV					
1	Li	0.526	-20.70	-21.12	0.515	-20.79	-21.30
2	Be	0.434	-20.54	-21.36	0.482	-20.67	-21.55
3	B	0.292	-20.30	-21.54	0.660	-20.76	-21.73
4	C	0.384	-20.40	-21.79	0.432	-20.52	-21.98
5	N	0.251	-20.15	-21.93	0.632	-20.64	-22.12
6	O	0.197	-20.01	-21.97	0.788	-20.71	-22.15
7	F	0.014	-18.86	-22.07	0.587	-20.61	-22.25
		E_{Lab} = 218 MeV; $E_{c.m.}$=125.23 MeV					
1	Li	0.541	-20.72	-21.48	0.744	-20.95	-21.67
2	Be	0.444	-20.56	-21.52	0.727	-20.85	-21.72
3	B	0.298	-20.32	-21.55	0.543	-20.67	-21.74
4	C	0.398	-20.42	-21.78	0.635	-20.69	-21.97
5	N	0.252	-20.15	-21.79	0.507	-20.54	-21.98
6	O	0.196	-20.01	-22.00	0.588	-20.58	-22.20
7	F	0.013	-18.84	-22.08	0.422	-20.46	-22.28

($\nu_0 \sim 10^{22} s^{-1}$) for all the preferred fragments shown in Table 5.2.

Also, column III and VI of the Table 5.2 depict the tunnelling probability (P) of emitting fragments in decay of $^{47}V^*$ at ℓ_{cr} and ℓ_{gr} respectively. From the table, it can be concluded that at critical angular momentum, the penetrability decreases with increase in fragment charge and hence with mass at all energies. This behavior of penetrability is same as that of its behavior for FF mode shown in Fig. 5.5. Also, the value of "P" at partial waves near and at grazing angular momentum (ℓ_{gr}) is greater than that of its value at ℓ_{cr}. This is possibly due to the fact that, the barrier vanishes as the partial waves of angular momentum approach the grazing limit. This can be better understood from Fig. 5.7, which clearly shows that for DIC channel, the barrier starts vanishing at $\ell = 47\hbar$ and almost disappears at ℓ_{gr}. This is in agreement with the liquid drop limit where barrier vanishes and shown in ref. [16].

5.3 Summary

The dynamics of $^{47}V^*$ formed in ^{20}Ne + ^{27}Al reaction is investigated. It is observed [8] that both FF (CN) and DIC (nCN) components are present in the decay of $^{47}V^*$ formed via direct kinematics reaction. Hence, present work covers both FF and DIC mechanisms in framework of dynamical cluster-decay model. DCM based calculations describe FF and DIC nicely over an extensive range of incident energies using the neck length parameter ΔR for quadrupole choice of fragments. The ℓ-values used to address the cross sections are $0 \leq \ell \leq \ell_{cr}$ for FF and $\ell_{cr} \leq \ell \leq \ell_{gr}$ for DIC. The pocket of potential barrier becomes shallower at larger value of angular momentum for FF and the same gets disappeared for DIC. It is noticed that the structure of potential energy surfaces does not depend on the incident energy. Here, the most favorable fragments identified through the minima in fragmentation potential and maxima in preformation probability are the isotopes lying in the range varying as $3 \leq Z \leq 9$ ($5 \leq A_2 \leq 19$) and match with the ones reported in [8]. Among all isotopes lying in the specified region, the fragments having equal number of

protons and neutrons (N=Z) are found to contribute most. Furthermore, the penetrability of fragments decrease with increase in mass of fragment, and increases with increase in angular momentum. In addition to above, σ_{FF} and σ_{DIC} are predicted at three center of mass energies ($E_{c.m.}$=93, 98, and 103 MeV) by fitting cubic polynomial for ΔR with center of mass energy as variable, which can be verified in future experiments. At last, the emission time computed using DCM are observed to be in good accordance with the reported data [8].

After explaining the comparative contribution of CN and nCN mechanism in light mass region of nuclei, it would be of further interest to explore the competing contribution of such processes in heavy mass region of compound systems. To accomplish this, the dynamics of $^{215}Fr^{*}$, ^{223}Pa*, ^{227}Np* and ^{233}Am* nuclei is studied in view of fission and quasi fission (QF), where QF represents the nCN component observed in heavy mass nuclei. This work is presented in chapter 6.

Bibliography

[1] R. K. Gupta, M. Balasubramaniam, R. Kumar, D. Singh and C. Beck, Nucl. Phys. A **738**, 479c (2004); R. K. Gupta, M. Balasubramaniam, R. Kumar, D. Singh, C. Beck and W. Greiner, Phys. Rev. C **71**, 014601 (2005).

[2] B. B. Singh, M. K. Sharma, R. K. Gupta, W. Greiner, Int. J. Mod. Phys. E **15**, 699 (2006).

[3] S. Kanwar, M. K. Sharma, B. B. Singh, R. K. Gupta and W. Greiner, Int. J. Mod. Phys. E **18**, 1453 (2009).

[4] R. K. Gupta, *Clusters in Nuclei*, Lecture Notes in Physics **818**, Vol. I, p. 223 (2010); ed. C. Beck, Springer-Verlag, Berlin, Heidelberg; S. K Arun, R. Kumar and R. K. Gupta, J. Phys. G: Nucl. Part. Phys. **36**, 085105 (2009).

[5] M. K. Sharma, S. Kanwar, G. Sawhney, R. K. Gupta and W. Greiner, J. Phys. G: Nucl. Part. Phys. **38**, 055104 (2011); D. Jain, R. Kumar, M. K. sharma and R. K. Gupta, Phys. Rev. C **85**, 024615 (2012).

[6] M. K. Sharma, G. Sawhney, R. K Gupta and W. Greiner, J. Phys. G: Nucl. Part. Phys. **38**, 105101 (2011);G. Sawhney, R. Kumar and M. K. Sharma, Phys. Rev. C **86**, 034613 (2012).

[7] N. Grover, I. Sharma, G. Kaur and M. K.Sharma, Nucl. Phys. A **959**, 10 (2017).

[8] A. Dey, C. Bhattacharya, S. Bhattacharya, T. K. Rana, S. Kundu, K. Banerjee, S. Mukhopadhyay, S. R. Banerjee, D. Gupta, and R. Saha, Phys. Rev. C **75**, 064606 (2007).

[9] N. Grover, K. Sharma, and Manoj K. Sharma, Eur. Phys. J. A **53**, 239 (2017).

[10] S. J. Sanders, D. G. Kovar, B. B. Back, C. Beck, D. J. Henderson, R. V. F. Janssens, T. F. Wang, and B.D. Wilkins, Phys. Rev. C **40**, 2091 (1989).

[11] S. J. Sanders, B. B. Back, R. V. F. Janssens, D. G. Kovar, D. Habs, D. Henderson, T. L. Khoo, H. Korner, G-E. Rathke, T. F. Wang, and F. L. H. Wolfs, Phys. Rev. C **41**, R1901 (1990).

[12] S. J. Sanders, A. Szanto de Toledo, and C. Beck, Phys. Rep. **311**, 487 (1999).

[13] B. B. Back, H. Esbensen, C. L. Jiang, and K. E. Rehm, Rev. Mod. Phys. **86**, 317 (2014).

[14] L. F. Canto, P. R. S. Gomes, R. Donangeloa, J. Lubianb , M.S. Hussein, Phys. Rep. **596**, 1 (2015).

[15] J. J. Kolata, V. Guimarães, and E. F. Aguilera, Eur. Phys. J. A **52**, 123 (2016).

[16] C. Beck, A. Szanto de Toledo, Phys. Rev. C **53**, 4 (1996).

[17] C. Bhattacharya, S. Bhattacharya, T. Bhattacharjee, A. Dey, S. Kundu, S. R. Banerjee, P. Das, S. K. Basu, and K. Krishan, Phys. Rev. C **69**, 024607 (2004).

[18] D. Shapira, D. DiGregorio, J. Gomez del Campo, R. A. Dayras, J. L. C. Ford, Jr., A. H. Snell, and P. H. Stelson, R. G. Stokstad, F. Pougheon, Phys. Rev. C **28**, 1148 (1983).

[19] A. Dey, C. Bhattacharya, S. Bhattacharya, S. Kundu, K. Banerjee, S. Mukhopadhyay, D. Gupta, T. Bhattacharjee, S. R. Banerjee, S. Bhattacharyya, T. K. Rana,

S. K. Basu, R. Saha, K. Krishan, A. Mukherjee, D. Bandopadhyay, and C. Beck, Phys. Rev. C **76**, 034608 (2007).

[20] S. Kundu, A. Dey, K. Banerjee, T. K. Rana, S. Muhkopadhayay, D. Gupta, R. Saha, S. Bhattacharya, and C. Bhattacharya, Phys. Rev. C **78**, 044601 (2008).

[21] D. Shapira, J. L. C. Ford, J. Gomez del Campo, R. G. Stokstad and R. M. Devries, Phys. Rev. Lett. **43**, 1781 (1979).

[22] W. Dünnweber, A. Glaesner, W. Hering, D. Konnerth, R. Ritzka, and W. Trombik, Phys. Rev. Lett. **61**, 927 (1988).

[23] D. Shapira, D. Schull, J. L. C. Ford, Jr., and B. Shivakumar, R. L. Parks, R. A. Cecil, and S. T. Thornton, Phys. Rev. Lett. **53**, 1634 (1984).

[24] S. Kundu, Pramana J. Phys., Vol. **82**, No. 4, (2014).

[25] T. M. Cormier, A. J. Lazzarini, M. A. Neuhausen, Phys. Rev. C **13**, 682 (1976).

[26] U. L. Businaro and S. Gallone, Nuovo Cimento **5**, 315 (1957).

[27] C. Beck, B. Djerroud, B. Heuseh, R. Dayras, R.M. Freeman, F. Haas, A. Hachem, J.P. Wieleczko, and M. Youlal, Z. Phys. A **334**, 521 (1989).

[28] C. Bhattacharya, K. Mullick, S. Bhattacharya, K. Krishan, T. Bhattacharjee, P. Das, S. R. Banerjee, D. N. Basu, A. Ray, S. K. Basu, and M. B. Chatterjee, Phys. Rev. C **66**, 047601 (2002).

[29] N. V. Sen, J. C. Gondrand, F. Merchez, and R. Darves-Blanc, Phys. Rev. C **22**, 2424 (1980).

[30] D. Agassi, C. M. Ko, and H. A. Weidenmüller, Ann. Phys. **107**, 140-167 (1977).

[31] C. M. Ko, D. Agassi, and H. A. Weidenmüller, Ann. Phys. **117**, 237-267 (1979)

[32] K. Siwek-Wilczyñska, J. Wilczyñski, Nucl. Phys. A **264**, 115-131 (1976).

[33] A. Sandulescu, H. Scutam and W Scheid, J. Phys. A: Math. Gen. **20**, 2121-2131 (1987).

[34] P. A. Gottschalk and M. Westrom, Phys. Rev. Lett. **39**, 20 (1977).

[35] G. Kaur. and M. K. Sharma, Int. J. Mod. Phys. E **23**, No. 10, 1450063 (2014).

[36] M. Kaur, B. B. Singh, S. K. Patra, and R. K. Gupta, Phys. Rev. C **95**, 014611 (2017).

[37] B. B. Singh, M. Kaur, M. K. Sharma and R. K. Gupta, J. Phys.: Conf. Ser. **569**, 012030 (2014); EPJ Web Conf. **86**, 00049 (2015).

[38] C. Beck, B. Djerroud, F. Haas, R. M. Freeman, A. Hachem, B. Heusch, A. Morsad, M. Youlal, Y. Abe, R. Dayras, J. P. Wieleczko, T. Matsuse, and S. M. Lee, Z. Phys. A **343**, 309 (1992).

[39] S. Pirrone, S. Aiello, N. Arena, S. Cavallaro, S. Femino, G. Lanzalone, G. Politi, F. Porto, S. Romano, and S. Sambataro, Phys. Rev. C **55**, 2482 (1997).

[40] C. Beck D. Mahboub, R. Nouicer, T. Matsuse, B. Djerroud, R. M. Freeman, F. Haas, A. Hachem, A. Morsad, M. Youlal, S. J. Sanders, R. Dayras, J. P. Wieleczko, E. Berthoumieux, R. Legrain, E. Pollacco, Sl. Cavallaro, E. De Filippo, G. Lanzano, A. Pagano, and M. L. Sperduto, Phys. Rev. C **54**, 227 (1996).

[41] C. Beck, B. Djerroud, F. Haas, R. M. Freeman, A. Hachem, B. Heusch, A. Morsad, M. Vuillet-A-Cilles, and S. J. Sanders, Phys. Rev. C **47**, 2093 (1993).

[42] A. Ray, D. Shapira, J. Gomez del Campo, H. J. Kim, C. Beck, B. Djerroud, B. Heusch, D. Blumenthal, and B. Shivakumar, Phys. Rev. C **44**, 514 (1991).

[43] R. L. Kozub, N. H. Lu, J. M. Miller, D. Logan, T. W. Debiak, and L. Kowalski, Phys. Rev. C **11**, 1497 (1975).

[44] J. B. Natowitz, M. N. Namboodri, R. Eggers, P. Gonthier, K. Geoffroy, R. Hanus, C. Towsley, and K. Das, Nucl. Phys. A **277**, 477 (1977).

[45] N. V. Sen, R. Darves-Blanc, J. C. Gondrand, and F. Merchez, Phys. Rev. C **27**, 194 (1983).

[46] H. Morgenstern, W. Bohne, K. Grabisch, H. Lehr, W. Stoffler, Z. Phys. A **313**, 39 (1983); H. Lehr, W. Bohne, K. Grabisch, H. Morgenstern, W. Von Oertzen, Nucl. Phys. A **415**, 149 (1984).

[47] M. Bansal, S. Chopra, R. K. Gupta, R. Kumar and M. K. Sharma, Phys. Rev. C **86**, 034604 (2012).

[48] Sahila Chopra, Hemdeep, Arshdeep Kaur, and Raj K. Gupta, Phys. Rev. C **93**, 024603 (2016).

[49] R. K. Gupta and M. Bansal, Int. Rev. Phys. (IREPHY) **5**, 74 (2011).

Chapter 6

Fission and quasi fission contributions for ^{18}O, ^{26}Mg, ^{30}Si and ^{36}S induced reactions at E^*_{CN}=60 MeV

So far an extensive analysis of decay outcomes associated with different compound nucleus mechanisms is concerned in previous chapters. The decay profiles for CN processes were explored in terms of potential energy surfaces, mass distribution, penetrability, and barrier modification etc. Besides this, the most commonly observed nCN process in light mass region of nuclei, termed as DIC, was also explored. Next, to extend the analysis of nCN processes in DCM framework, the present chapter aims to explain another such mechanism known as Quasi Fission (QF), which is generally observed in heavy and superheavy mass region of nuclei. Here, in this chapter, the comparative analysis of fission and quasi fission is described for ^{18}O+^{197}Au$\rightarrow^{215}$Fr*, ^{26}Mg+^{197}Au$\rightarrow^{223}$Pa*, ^{30}Si+^{197}Au$\rightarrow^{227}$Np* and ^{36}S+^{197}Au$\rightarrow^{233}$Am* reactions at common excitation energy, E$^*_{CN}$=60 MeV. This work is done in context to the experimental data of [1] and is published in [2]. Also, the analysis of ^{223,227}Pa* isotopes and isobaric nuclei-^{227}Pa*, ^{227}Np* is worked out to have a comprehensive

idea about the dynamics involved. A brief introduction related to this work is presented in Sec. 6.1. The calculations and results are discussed in Sec. 6.2 and finally the results are summarized in Sec. 6.3.

6.1 Introduction

In low energy regime, exploring the fusion-fission phenomenon has been a topic of immense importance since ages. The vigorous research carried out in this domain may be attributed to the fact that fusion-fission studies help in understanding the nuclear behavior to a better extent, mainly by addressing numerous aspects related to synthesis and decay patterns of nuclear system. Formerly, the fusion-fission studies were confined to reactions involving light mass projectiles such as protons, alpha, and stable heavy ions etc. induced on stable targets such as gold, lead and bismuth nuclei. Later, with the discovery of radioactive nuclear beams, examining the fusion-fission decay patterns for heavy ion reactions became an exciting area of research [3]. In such reactions, fusion may involve complete amalgamation of projectile and target nucleus leading to a composite system formed inside the fission barrier. This composite system is equilibrated in all degrees of freedom and is termed as compound nucleus (CN) which can be better understood via evaporation or fission decay channel. In general, the decay of CN is governed by the statistical laws and is independent of its entrance channel. However as an exception to fusion-fission decay of CN, there may also be a possibility that fusion of heavy nuclei is significantly obstructed and consequently the formation of CN is inhibited giving rise to non-equilibrium composite system i.e. the non compound nucleus (nCN). The fission fragments emitted from the decay of nCN geometry retain the entrance channel memory and may be understood in terms of Quasi Fission (QF) process. It represents a competing non-compound nucleus process in which the composite system re-separates before reaching an equilibrium state and thus retains the entrance channel properties, unlike CN.

Various reaction conditions such as “incident energy, charge product, mass asymme-

try (α), deformations and orientations" of the incoming channel play crucial role in the emergence of QF [4]. It is observed that for the reactions in which the charge product of interacting nuclei is high, i.e. $Z_P Z_T$ >1600 (where Z_P and Z_T are the charges of projectile and target nuclei) or the mean fissility exceeds 0.72, the chances of presence of QF component become significant. This may also be understood via dynamics of mass flow in the composite system in terms of entrance channel mass asymmetry. The critical "Businaro-Gallone mass asymmetry" (α_{BG}) distinguish the "mass symmetric liquid drop fission barrier" from "asymmetric" one and thus forms an important parameter in governing the onset of quasi fission [5]. For the reactions with entrance channel mass asymmetry (α) greater than α_{BG} ($\alpha > \alpha_{BG}$), the mass flows from projectile to target nucleus, and quickly results into an equilibrated composite system [6]. Contrarily, for symmetric reactions (with $\alpha < \alpha_{BG}$), the mass flows in direction of more symmetric composite system which re-separates before achieving the equilibrium, thus giving rise to QF [7–10]. Apart from the above mentioned conditions, the deformations and orientations of interacting nuclei also play a crucial role in contribution of QF. When the projectile strikes at the tip point of the deformed target then the composite system formed just after the head on collision can achieve fully equilibrated compound nucleus configuration only if, it is able to reside within the saddle point; otherwise, it decays before acquiring the full equilibration due to the elongated configuration and consequently results into the nCN fission contribution. The reactions exhibiting quasi fission occur faster than those involving fusion fission process [11]. However, recent studies reveal that the quasi fission may also occur as an exception to some of above mentioned conditions [1]. Consequently, the decay of heavy nuclear systems under the extreme conditions of temperature, angular momentum, deformations, etc., has been studied extensively in order to find useful information regarding fusion-fission and competing QF process. However, the knowledge so obtained is still very scarce and opens many questions for attaining a comprehensive picture of heavy ion induced dynamics.

In view of this, an attempt has been made to explore the reaction dynamics associated

with fission and quasi fission processes for odd mass ^{215}Fr*, ^{223}Pa*, ^{227}Np* and ^{233}Am* nuclei using collective clusterisation approach of DCM [12–20]. In a recent experiment [1], the decay cross-sections of above mentioned nuclei formed using ^{18}O, ^{26}Mg, ^{30}Si and ^{36}S projectiles with ^{197}Au target have been measured at common excitation energy of E^{*}_{CN}=60 MeV. Also, it has been noticed that fission is the dominant decay mode for given compound systems. Here, in the present work, owing to the deformed nature of projectile and target, the role of deformation is explored by carrying out the comparative study of spherical and quadrupole (β_{2i}) deformed approach. Also the effect of different projectiles induced on a common target and hence the role of mass of compound nucleus is examined in the present study. Another interesting aspect explored is the probable influence of shell closure effects [21] of the outgoing fragments on the decay process. The existence of such effects signify the contribution of some competing nCN process along with the CN decay [22]. Moreover, since the orientation degree of freedom also plays a crucial role in the onset of nCN, the same has been investigated for the heavy mass nuclei under study.

In view of above, the novelty of the present work is (i) to scrutinize the characteristic behavior of different compound mass nuclei formed in reactions involving different projectile with same target nucleus (ii) to explore the role of deformations and its behavior with increment in mass of compound nucleus (iii) to investigate the competing QF process in terms of shell closure effect and orientation degree of freedom, studied for the oblate deformed target for the first time and (iv) to analyze the dynamics of ^{223,227}Pa* isotopes and isobaric nuclei-^{227}Pa*, ^{227}Np*.

6.2 Calculations and results

The present study reveals some interesting aspects associated with nuclear structure and reaction dynamics of various compound systems with mass A=215-233. The reactions under consideration involve four different projectiles - ^{18}O, ^{26}Mg, ^{30}Si and ^{36}S induced

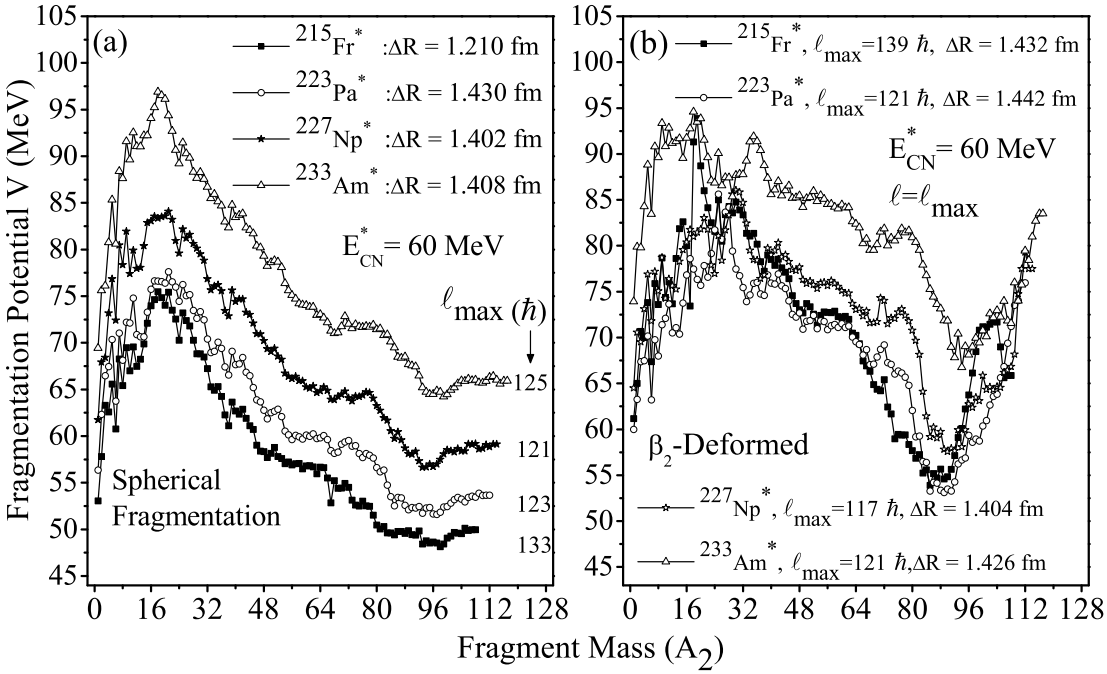

Figure 6.1 The variation of fragmentation potential V (MeV) as a function of fragment mass A_2 for the decay of ^{215}Fr*, ^{223}Pa*, ^{227}Np* and ^{233}Am* nuclei, at ℓ=ℓ_{max} for (a) Spherical and (b) β_2-deformed approach at E^*_{CN}=60 MeV.

on a unique target, ^{197}Au at common excitation energy of E^*_{CN}=60MeV. For the heavy mass nuclei, the fission decay mode forms an unambiguous tool to address the reaction dynamics and the same has been explored in this work, for the pre-actinide and trans-actinide systems in reference to the data of [1] using DCM framework. To estimate the decay cross-sections in DCM, partial wave analysis (PWA) has been applied with angular momentum range from ℓ=0$\hbar$ to ℓ=ℓ_{max}. It is pertinent to inscribe here that the DCM has been applied to explore the dynamic evolution of numerous composite systems lying in different mass regions of periodic table. In the present work, an endeavour has been made to understand the dynamics of ^{215}Fr*, ^{223}Pa*, ^{227}Np* and ^{233}Am* nuclei and the decay patterns of these nuclei are explored by striking different projectiles on an oblate deformed target. Firstly, the role of deformations is studied by comparing the potential energy surfaces, mass distribution and barrier characteristics of outgoing fragments obtained using spherical approach and with the inclusion of deformations effects. Besides this, the related shell closure effect and the impact of hot (equatorial) versus cold (polar)

orientation degree of freedom has been investigated for the aforementioned nuclei. Besides this, attributing to the signatures observed for the nCN process, the contribution of QF has also been examined in the framework of DCM. Figs. 6.1(a) and (b) depict the fragmentation potential V (A_2) minimized in mass co-ordinate η_A for the decay of odd mass nuclei plotted for spherical and quadrupole (β_2) deformed approach respectively at maximum value of angular momentum, ℓ=ℓ_{max}. It can be seen that, the characteristic behavior of fragmentation potential and hence the preformation probability is not identical for maximum and minimum angular momentum. At ℓ=0$\hbar$, the preformation probability is maximum for lighter fragments (with mass 0<A_2≤4) and decreases with increase in fragment mass. Contrarily, at higher angular momentum, i.e. $\ell = \ell_{max}$, the probability for fission fragments is more dominant as compared to light mass fragments. Also, in the present work, fission is the dominant decay mode, thus the analysis is illustrated at ℓ_{max} only as lower ℓ-values corresponds to the ER decay mode. From Fig. 6.1(a), it is noticed that, although the structure of fragmentation potential is similar for all four nuclei, a considerable difference in magnitude of potential is observed. Interestingly, in framework of DCM, it has been observed that for a given nucleus, the centrifugal potential plays a crucial role in the decay study and contributes towards the magnitude of fragmentation potential. However, in the present work involving comparative study of different mass nuclei, it has been observed that, despite of relatively higher angular momentum (ℓ_{max}=133$\hbar$), the magnitude of fragmentation potential is minimum for the lightest nucleus, ^{215}Fr* and increases with increase in mass, being maximum for the heaviest nucleus ^{233}Am*. This trend of fragmentation potential with respect to mass of the compound nucleus suggests that, the magnitude of fragmentation potential is relatively more influenced by its fragment mass as compared to the corresponding centrifugal potential. In other words, the magnitude of fragmentation potential is governed by mass of compound nucleus formed irrespective of the magnitude of the angular momentum. Further, from the variation of fragmentation potential plotted for deformed approach as shown in Fig. 6.1(b), it is evident that potential energy surfaces (PES) for HMF and fission region get

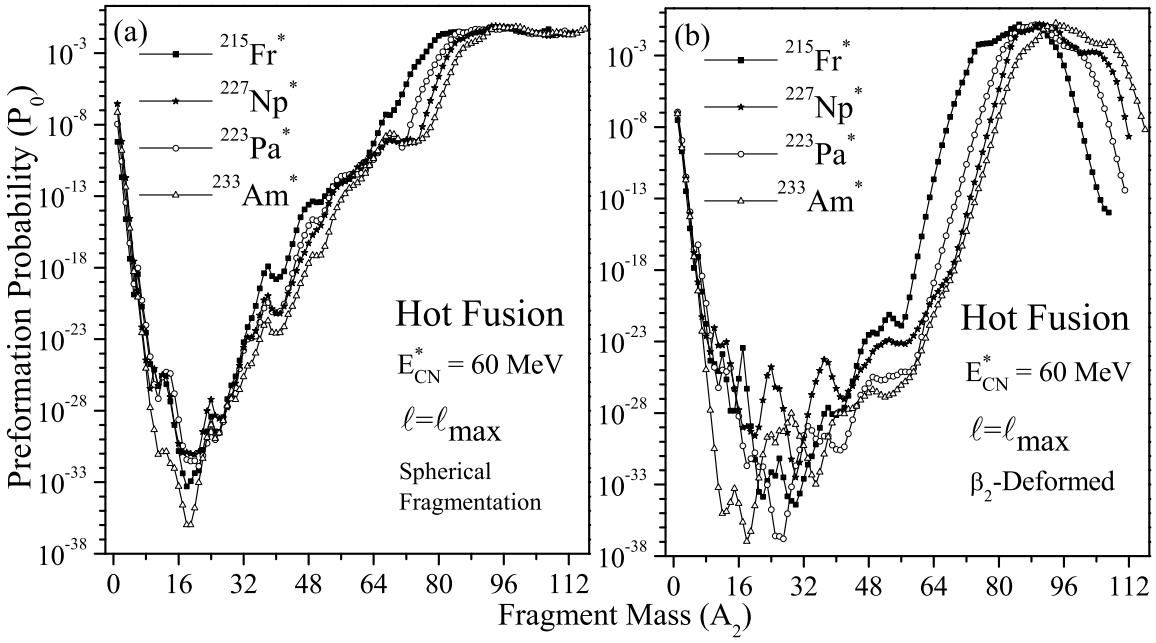

Figure 6.2 Preformation probability (P_0) plotted as a function of fragment mass (A_2) for the decay of $^{215}Fr^*$, $^{223}Pa^*$, $^{227}Np^*$, $^{233}Am^*$ nuclei for (a) Spherical and (b) β_2-deformed choice within optimum orientation (θ_i^{opt}) approach for hot (equatorial) compact configuration at E^*_{CN}=60 MeV.

significantly influenced with the inclusion of quadrupole (β_2) deformations. Evidently, the fragment distribution changes from symmetric to asymmetric distribution when spherical fragmentation is replaced by quadrupole deformed approach. Moreover, for the spherical approach, the potential energy surfaces (PES) for each compound nucleus are easily distinguishable for all fragments masses whereas with the inclusion of quadrupole deformations they almost coincide with each other for ER and IMF region. However, for the HMF and fission region, the PES are distinguishable at some extent for $^{215}Fr^*$, $^{223}Pa^*$, $^{227}Np^*$, $^{233}Am^*$ nuclei.

Table 6.1 The fission decay cross-sections of ^{215}Fr*, ^{223}Pa*, ^{227}Np* and ^{233}Am* compound systems formed in different reactions involving common target (^{197}Au) are catalogued in DCM framework for spherical and quadrupole (β_2-deformed) choice of fragments. The cross-sections are shown at E^*_{CN}=60 MeV, compared with the experimental data [1]. Also, ΔR, and ℓ_{max} values are tabulated.

S. No.	Projectile	Target	Compound Nucleus	$E_{c.m.}$ (MeV)	T (MeV)	Fission Fragments Sph. A_2	Fission Fragments β_2 A_2	ΔR Sph. (fm)	ΔR β_2 (fm)	ℓ_{max} Sph. ($\hbar$)	ℓ_{max} β_2 ($\hbar$)	$\sigma^{DCM}_{fission}$ Sph. (mb)	$\sigma^{DCM}_{fission}$ β_2 (mb)	$\sigma^{Expt.}_{capture-fission}$ (mb)
1	^{18}O	^{197}Au	^{215}Fr*	92.8	1.61	85-107	80-93	1.432	1.210	133	139	756	830	834 ±4
2	^{26}Mg	^{197}Au	^{223}Pa*	130.1	1.56	87-111	81-97	1.442	1.417	123	121	557	580	749 ±6
3	^{30}Si	^{197}Au	^{227}Np*	148.3	1.57	91-113	84-97	1.404	1.402	121	117	439	486	770 ±10
4	^{36}S	^{197}Au	^{233}Am*	165.1	1.54	96-116	89-103	1.426	1.408	125	121	356	384	748 ±10

Table 6.2 The fission decay cross-sections of ^{215}Fr*, ^{223}Pa*, ^{227}Np* and ^{233}Am* compound systems calculated for the use of cold (polar) elongated configuration in the DCM framework. The cross-sections are shown at E^*_{CN}=60 MeV, compared with the experimental data [1]. Also, ΔR, and ℓ_{max} values are tabulated.

S. No.	Projectile	Target	Compound Nucleus	$E_{c.m.}$ (MeV)	T (MeV)	Fission fragments(A_2)	ΔR (fm)	ℓ_{max} ($\hbar$)	$\sigma^{DCM}_{fission}$ (mb)	$\sigma^{Expt.}_{capture-fission}$ (mb)
1	^{18}O	^{197}Au	^{215}Fr*	92.8	1.61	95-107	1.413	106	834.3	834 ±4
2	^{26}Mg	^{197}Au	^{223}Pa*	130.1	1.56	95-112	1.418	107	606	749 ±6
3	^{30}Si	^{197}Au	^{227}Np*	148.3	1.57	93-114	1.435	120	530	770 ±10
4	^{36}S	^{197}Au	^{233}Am*	165.1	1.54	93-112	1.417	117	481	748 ±10

Above observations suggest that for the heavy mass nuclei under study, the deformations are of considerable importance. To further explore the role of deformations, the preformation probability (P_0) is depicted as a function of fragment mass A_2, for spherical as well as deformed approach within optimum orientation approach (θ_i^{opt}) for hot (equatorial) compact configuration and exhibited in Fig. 6.2(a) and (b) respectively, for spherical and deformed approach. It is noticed that the preformation probability also gets affected with the inclusion of deformations. Further, in accordance with the observation drawn from Fig. 6.1(a) and (b), the variation of P_0 confirms that for all the four nuclei, the mass distribution deviates from symmetric to asymmetric with the inclusion of quadrupole deformations within optimum orientation approach. Thus, it may be concluded that deformations effects are more pronounced for the heavy mass and fission fragments, and relatively silent for light mass fragments. Also, for a given fragment mass A_2, the preformation probability is higher for $^{215}Fr^*$ nucleus in intermediate mass region and heavy mass fragments (HMF) region, being least for heaviest mass nucleus $^{233}Am^*$.

In framework of DCM, the preformation probability (P_0) also helps in identifying the individual fragments contributing towards the decay of a given compound systems under study. From the variation of P_0 plotted in Fig. 6.2(a) and (b), it is clearly evident that corresponding to each compound nucleus mass, the fragment mass range contributing towards the fission decay is higher for spherical choice as compared to that for deformed approach. Further, the contributing fission fragments in decay of $^{215}Fr^*$, $^{223}Pa^*$, $^{227}Np^*$ and $^{233}Am^*$ nuclei along with the corresponding fission cross-sections are presented in Table 6.1 for both spherical and quadrupole deformed choice of fragments using optimum orientation approach. The decay cross-sections of all given nuclei are addressed by optimizing the neck length parameter (ΔR) of DCM. The ΔR in DCM symbolize the relative separation between two outgoing fragments in the decay of given compound systems. It is well known that the long-range Coulomb and centrifugal interactions are not adequate to explain the emergence of a compound nuclear system. Besides this, the short-range nuclear interaction play a crucial role. In DCM, the pocket formula of Blocki *et al.* [32] is employed

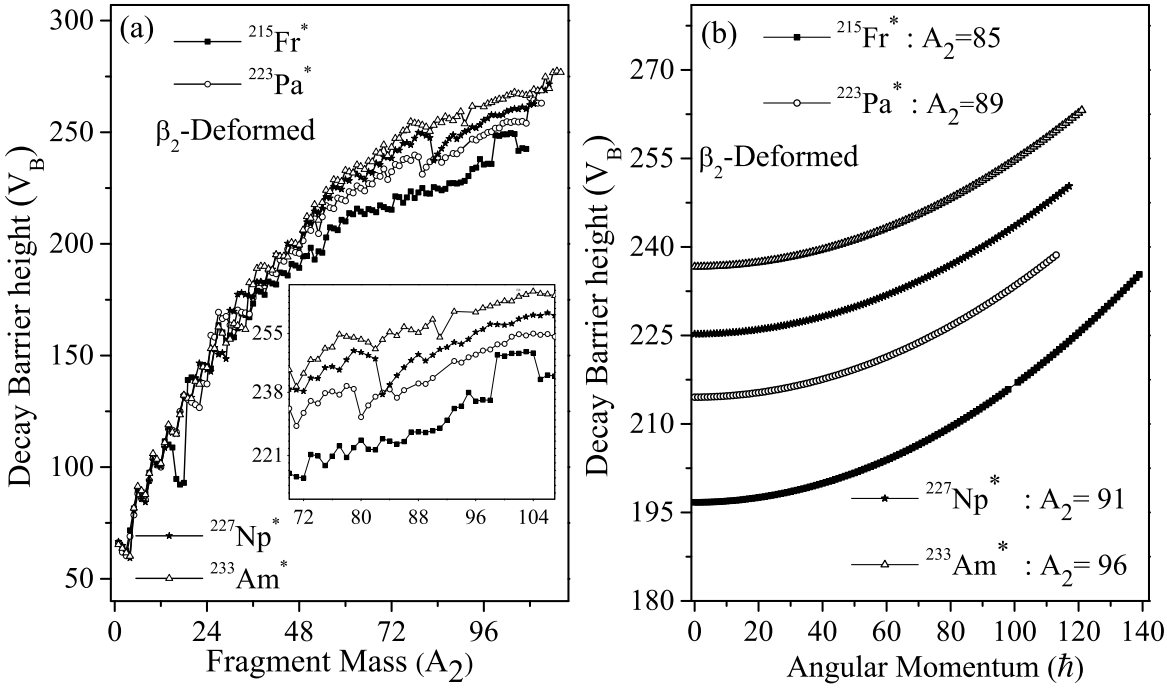

Figure 6.3 Variation of barrier lowering parameter as a function of (a) fragment mass, A_2 and (b) angular momentum, ℓ ($\hbar$) (for most probable fragment) plotted for the decay of given compound nuclei for β_2-deformed choice of fragmentation at ℓ=ℓ_{max}.

for proximity potential which uses the computed values of surface tension and surface diffuseness. Since both the thickness of the nuclear surface and the range of the nuclear interaction are of the order of 1.5 - 2 fm, the range of ΔR is constrained to a limit of $\sim$ 2 fm. The corresponding values of ΔR and ℓ_{max} used in the present work are tabulated in Table 6.1 along with the experimental data. From the table it is evident that, the neck-length parameter, ΔR implied to calculate the fission cross-sections is relatively higher for spherical approach. It may be noted that, despite of high mass range of contributing fragments and higher neck length, the fission cross-sections attained for spherical approach show large difference from the measured experimental data. On the other hand, the fission cross-sections attained with inclusion of quadrupole (β_2) deformations are relatively higher and find better agreement with the experimental data. This comparative behavior for spherical and deformed approach seems to suggest that the deformations of decaying fragments play a crucial role, so the further study is confined to the use of quadrupole

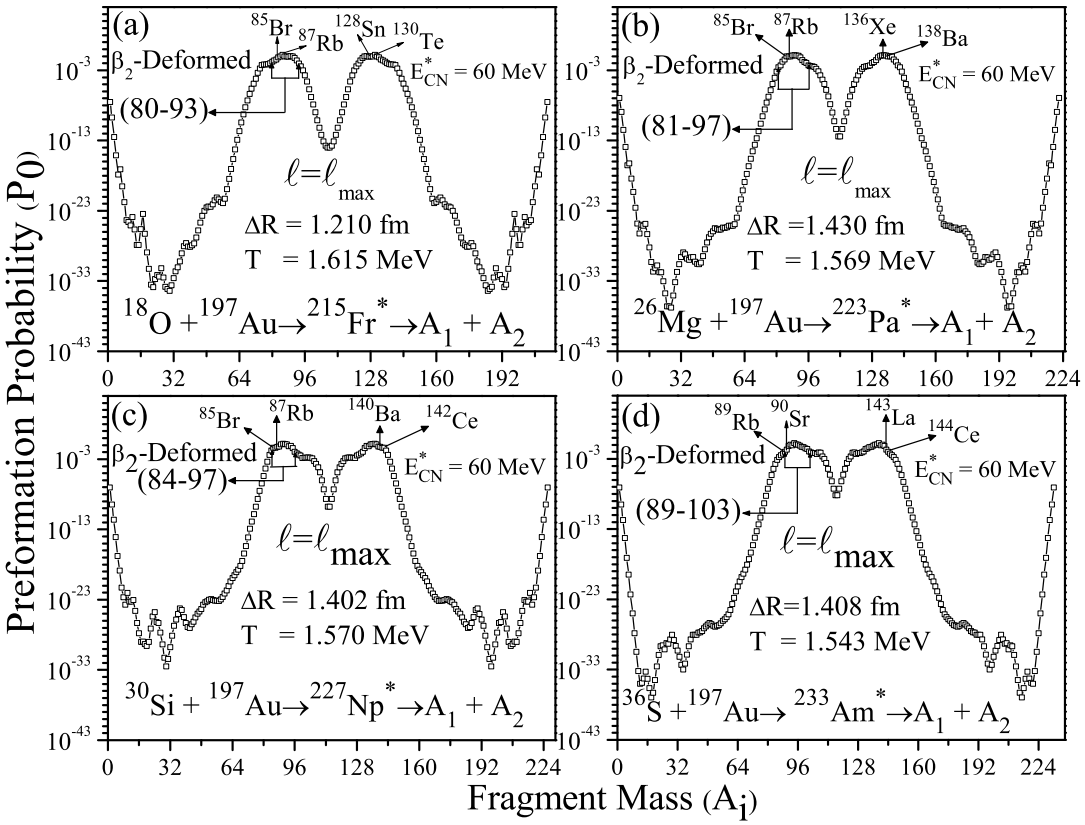

Figure 6.4 Preformation probability P_0 plotted as a function of fragment mass A_i (i=1,2) for different compound systems (a)$^{215}Fr^*$ (b)$^{223}Pa^*$ (c)$^{227}Np^*$ (d)$^{233}Am^*$ for β_2-deformed approach, showing the presence of shell effects.

deformed approach only. Another interesting observation drawn from Table 6.1 is that for ^{215}Fr* nucleus, using quadrupole deformed approach, the DCM based calculations reproduce the experimentally data nicely. However, for the transactinide nuclei, the DCM estimated fission cross-sections are noticed to deviate from the experimental measured capture-fission cross-sections, thus bringing one of the nCN process, i.e. quasi fission (QF) into picture [1]. After analyzing the role of deformations through the variation of fragmentation potential and preformation probability P_0, the characteristic behavior of decay barrier height V_B is studied as a function of fragment mass A_2 and angular momentum ℓ, as depicted in Fig. 6.3. The variation of barrier height as a function of fragment mass A_2 is exhibited in Fig. 6.3(a) for the odd mass nuclei, formed in X+^{197}Au reaction channels where X represents ^{18}O, ^{26}Mg, ^{30}Si and ^{36}S projectile nuclei.

The behavior is studied at corresponding maximum angular momentum, ℓ=ℓ_{max}. It is observed that, the barrier height increases with increase in fragment mass A_2, for all the nuclei under study. As witnessed earlier, from the variation of preformation probability, the decay barrier height almost overlap each other for heavy mass fragment region, for different decay regimes such as ER, IMF and HMF, one may see the variation in barrier height profile but clearly distinct pattern is not observed for fission fragments, the decay barrier height depends upon the mass of compound nucleus (A_{CN}) being maximum for heaviest nucleus $^{233}Am^*$ and minimum for relatively lighter, ^{215}Fr* nucleus. This suggests that for a given fragment mass A_2 lying in fission window, the decay probability is more for ^{215}Fr* and relatively less for other heavier nuclei. This behavior justifies the observation drawn earlier from Fig. 6.2 and Table 6.1, where the preformation yield and hence the decay cross sections were found to be highest for ^{215}Fr*. As Fig. 6.3(a) deals with the variation of decay barrier height at an explicit ℓ value, it would be interesting to examine its behavior at extreme ℓ-values, i.e. ℓ=0 to ℓ_{max}. To investigate this, the decay barrier height V_B is plotted at different ℓ values for the most likely fission decay fragments contributing towards the decay of ^{215}Fr*, ^{223}Pa*, ^{227}Np* and ^{233}Am* nuclei composed in the given reaction channels (mentioned above), as shown in Fig. 6.3(b). For a given compound nucleus, the variation of decay barrier height obey the regular trend and increases with increase in angular momentum, being maximum at highest ℓ-value. Moreover, at a given ℓ-value, the barrier height is least for ^{215}Fr* nucleus, which re-confirms that the CN decay probability is maximum for ^{215}Fr* nucleus and decreases with increase in mass of the CN. Besides studying the role of deformations and exploring the relative dynamics associated with X+^{197}Au reactions, an attempt has been made to explore the shell closure effect of decay fragments and its behavior corresponding to the mass of the compound nucleus. In the earlier work on DCM [17], the shell-closure effects of the decay fragments were noticed to play significant role for various Fr isotopes formed at E^*_{CN}=47 MeV. In the current study, we intend to scrutinize the uniformity of results so obtained at E^*_{CN}=60 MeV for ^{215}Fr* nucleus, as well as for the heavy mass transactinide nuclei, ^{223}Pa*, ^{227}Np*

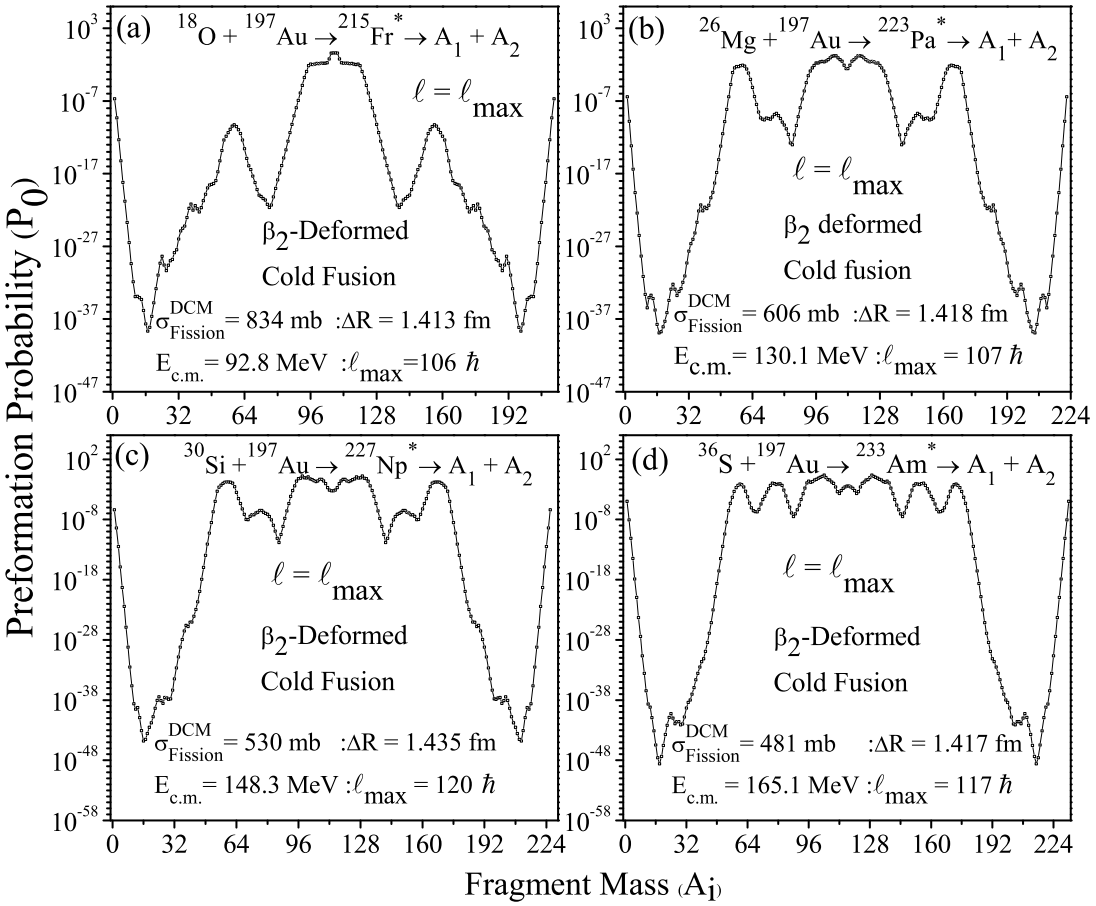

Figure 6.5 The variation of preformation probability (P_0) as a function of fragment mass (A_i) for the decay of (a) ^{215}Fr*, (b) ^{223}Pa*, (c) ^{227}Np* and (d) ^{233}Am* nuclei formed in X+^{197}Au reactions plotted at ℓ=ℓ_{max} for the use of cold polar orientation.

and ^{233}Am*. The preformation probability of four odd mass nuclei is plotted as a function of fragment mass A_2, for the use of quadrupole deformed approach as depicted in Fig. 6.4. For the nuclei under study, the fragments with higher preformation probability, contributing towards the fission cross-sections are explicitly marked in this figure along with the possible shell closure (magic shells), represented as maxima's in the fission region corresponding to both the light- and heavy-mass fragments (for ^{215}Fr*, ^{223}Pa*, ^{227}Np* and ^{233}Am* nuclei). The mass distribution is asymmetric for all the compound nuclei and a small hump or shoulder can be noticed in the fragment preformation yields.

Table 6.3 The Quasi fission cross-sections calculated using DCM for ^{223}Pa*, ^{227}Np*, ^{233}Am* nuclei formed by using unique target (^{197}Au) at E^{*}_{CN}=60 MeV.

S.No.	Projectile	Z_1Z_2	$E_{c.m.}$ (MeV)	T (MeV)	Hot Fusion				Cold Fusion				$P^{Expt.}_{CN}$
					ΔR (fm)	ℓ_{max} ($\hbar$)	σ^{DCM}_{QF} (mb)	$\sigma^{Expected}_{QF}$ (mb)	ΔR (fm)	ℓ_{max} ($\hbar$)	σ^{DCM}_{QF} (mb)	$\sigma^{Expected}_{QF}$ (mb)	
1	^{26}Mg	948	130.1	1.56	1.350	121	168	169	1.219	108	143	143	1.00
2	^{30}Si	1106	148.3	1.57	1.332	117	283	283	1.200	121	269	272	0.06
3	^{36}S	1264	165.1	1.54	1.342	121	361	364	1.207	119	296	298	0.13

The emergence of these humps is owing to the presence of deformed shell closure around light fragment Z_2=36 (actually Z_2=35 and Z_2=37) and spherical shell closure of heavy fragment Z_1 = 50 (actually at Z_1 = 50 and 52), and is relatively more pronounced for the decay of $^{215}Fr^*$ nucleus (having N = 128). However, with increase in mass of projectile and hence compound nucleus A_{CN}, the asymmetric mass distribution tends to diminish and the isospin (N/Z) ratio decreases but the presence of magic shells is observed for all nuclei. For $^{215}Fr^*$ (having N=128), the shell effects arise around deformed proton magic Z_1=36 and spherical magic Z_2=50 whereas for heavier nucleus,$^{223}Pa^*$, the shell closure is observed for spherical neutron magic N_1=50 and N_2=82 and for $^{227}Np^*$, it is observed to be at spherical neutron magic N_1=50 and around N_2=82 (actually at N_2=84). Further, for the $^{233}Am^*$ nuclei, the shell closure corresponds to neutron magic N_1=50 (actually at N_2=52) and N_2=82 (actually at N_1=86). Thus it can be concluded that the the shell closure effect of decaying fragments are of large significance and the same are relatively more pronounced for lighter nuclei. The observations drawn from Fig. 6.4 are consistent with those of [17], which shows that shell effects are relatively prominent for lightest nucleus and diminishes with increase in mass. Moreover, from our earlier study [33], it was observed that, for $^{213}Fr^*$ with N=126, the shell effects are more prominent and the contribution of competing quasi fission (QF) process is less as compared to heaviest isotope $^{217}Fr^*$ for which shell effects are less pronounced and contribution of QF is more. A similar observation is drawn here, which suggests that the contribution of QF is less for asymmetric reactions $^{18}O+^{197}Au\rightarrow^{215}Fr^*$ and $^{26}Mg+^{197}Au\rightarrow^{223}Pa^*$ as compared to relative symmetric reactions, $^{30}Si+^{197}Au\rightarrow^{227}Np^*$ and $^{36}S+^{197}Au\rightarrow^{233}Am^*$. Evidently, apart form the role of deformations and shell effects, the orientation degree of freedom holds equal importance as far as heavy ion reaction dynamics is concerned. Thus, after having an insight of quadrupole deformations and the shell closure effects, we aspire to probe the explicit role of orientation degrees of freedom for the reactions involving oblate deformed target ^{197}Au. The presence of deformed target is mainly associated with the compactness/non-compactness of the compound nuclear structure. This is because,

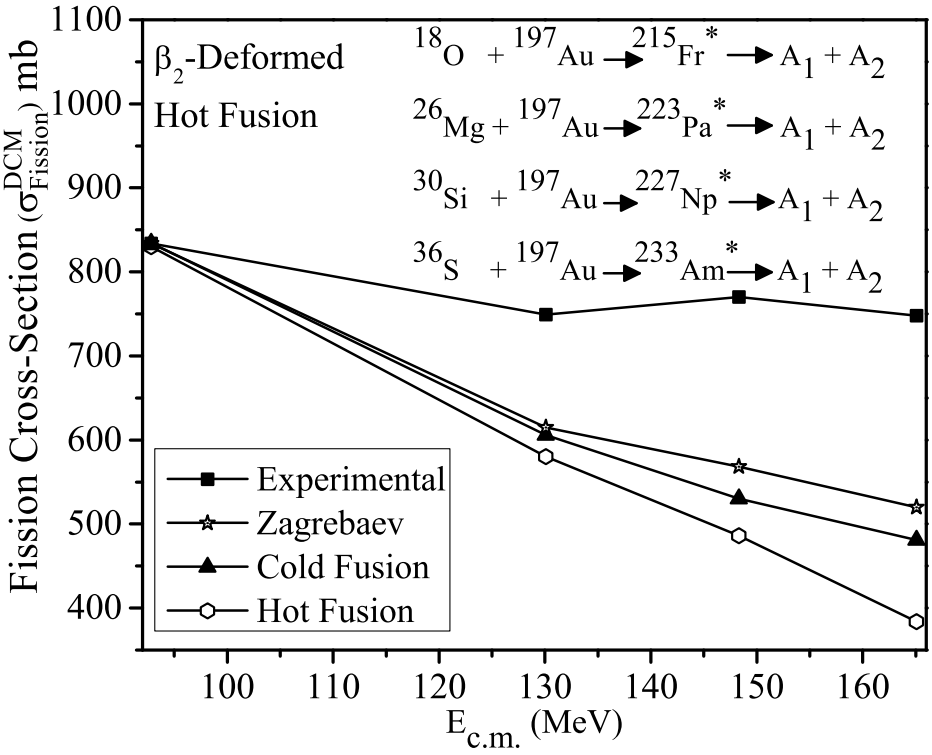

Figure 6.6 Comparison of DCM calculated cross-section with prediction of Zagrebaev and the measured experimental data [1].

the orientations of the deformed target explores the opportunity that the projectile may hit the equatorial part of the target nucleus and thus form the most compact starting configuration on way to the compound nucleus formation, which may subsequently decay further. Interestingly, the possibility of equatorial collisions leading to hot (equatorial) compact nuclear structure is relatively more at energies above the Coulomb barrier but the situation may change drastically when equatorial collisions are substituted by polar collisions in the sub-barrier region, leading to elongated configuration for which the re-separation of the reaction partners is relatively large and hence the probability of quasi fission gets enhanced [34]. A lot of theoretical and semi-empirical calculations have been made to understand the quasi fission process and to estimate its contribution towards fusion cross-sections [35]. In view of this, we intend to investigate the role of orientation degree of freedom in the decay of ^{215}Fr*, ^{223}Pa*, ^{227}Np* and ^{233}Am* nuclei. From Fig. 6.5, showing variation of preformation probability as a function of fragment mass A_2 for

cold (polar) elongated configuration, it is noticed that the mass distribution is relatively symmetric when compared with hot orientation (shown in Fig. 6.4). Comparing Fig. 6.5 with Fig. 6.4, it may be observed that significant structural variation is observed and the mass distribution changes from asymmetric to near symmetric distribution when hot (equatorial) compact configuration is replaced with cold (polar) elongated orientation. On the contrary, in earlier DCM calculations it has been observed that for the use of prolate deformed target, the symmetric mass distribution for hot orientation changes to asymmetric distribution for the use of cold orientation [14]. Thus, one may conclude that the mass distribution depends upon the orientation as well as on the type of deformation (prolate or oblate) of target nuclei. One may observe in Fig. 6.5, that the fission distribution is symmetric for $^{215}Fr^{*}$ nucleus, with negligible contribution from asymmetric fragments. However, with increase in mass of projectile the asymmetric shoulders start emerging. In other words the role of projectile mass and that of composite system is distinctly visible in the preformation profile generated using cold orientations. The DCM estimated fission cross-sections for cold orientation approach are tabulated in Table 6.2. It may be recorded that the fission decay cross-sections are large for cold configuration (see Table 6.2) and relatively small for hot orientation (See Table 6.1). Interestingly, the DCM estimated fission cross-sections lie in the vicinity of semi-empirical predictions of Zagrebaev and Griener [35]. However, the predicted cross-sections and the DCM calculated cross-sections both do not saturate the measured experimental capture-fission cross-section, which inturn suggest the possibility of competing quasi fission channel. Corresponding to the ΔR values tabulated in Table 6.1 and 6.2, the DCM calculated fission cross-sections for hot (equatorial) compact and cold (polar) elongated orientations have been depicted in Fig. 6.6, compared with theoretical predictions stated in [1] and the experimentally measured capture-fission cross-section data. The cross-sections have been plotted as a function of center-of mass energy, $E_{c.m.}$, each of which corresponds to individual reaction channels and hence mass of the compound nucleus under study. It is observed that for cold orientation, the fission cross-sections calculated using DCM are larger in magnitude

as compared to the hot orientation and are in better agreement with the theoretically predicted cross-sections of Zagrebaev [35]. However, except from the lightest nucleus ^{215}Fr*, the DCM calculated fission cross-sections do not accord with the experimentally measured capture fission cross-sections, for both hot and cold orientation approach. The large deviation in DCM cross-sections from the experimental measurements seems to suggest that the decay of ^{223}Pa*, ^{227}Np* and ^{233}Am* nuclei involve the contribution of one of the non-compound nucleus process, which is addressed in the form of quasi fission in the present case. From the figure it is also clear that, with increase in energy and hence with mass of the compound nucleus, the deviation of calculated fission cross-sections ($\sigma_{fission}^{DCM}$) from the experimental observations ($\sigma_{capture-fission}^{Expt.}$) also increases. Thus signifying the possible contribution of quasi fission cross-sections for these nuclei. Here, the contribution of QF is associated with difference between calculated and measured results, i.e.

$$\sigma_{Quasifission} = \sigma_{capture-fission}^{Expt.} - \sigma_{fission}^{DCM} \tag{6.1}$$

and is calculated for the incoming channel by considering maximum preformation probability, i.e. P_0=1. With this scenario, the QF contribution is attained for the heavy mass nuclei under study by implying neck-length parameter, ΔR. It is pertinent to note here that for all three trans-actinide nuclei, the QF cross-sections have been attained at a unique neck-length of ΔR $\sim$1.3 fm for hot orientation and at relatively smaller neck, i.e. ΔR $\sim$1.2 fm for cold orientation. The cross-sections so obtained are tabulated in Table 6.3 for both hot and cold approach. Further, the variation of quasi fission cross sections as a function of angular momentum, ℓ ($\hbar$) for the ^{26}Mg+^{197}Au, ^{30}Si+^{197}Au and ^{36}S+^{197}Au reactions has been plotted in Fig. 6.7. The pre-actinide nucleus, ^{215}Fr* formed in ^{18}O+^{197}Au reaction shows no signature of QF and hence has not been depicted in this study. From variation of Fig. 6.7 it is noticed that the quasi fission cross sections (σ_{QF}^{DCM}) increases with increase in angular momentum. Thus, it may be said that higher angular momentums contribute more towards the QF component. All the reactions exhibiting QF process involve different incoming channels, having same excitation energy (E_{CN}^{*} =

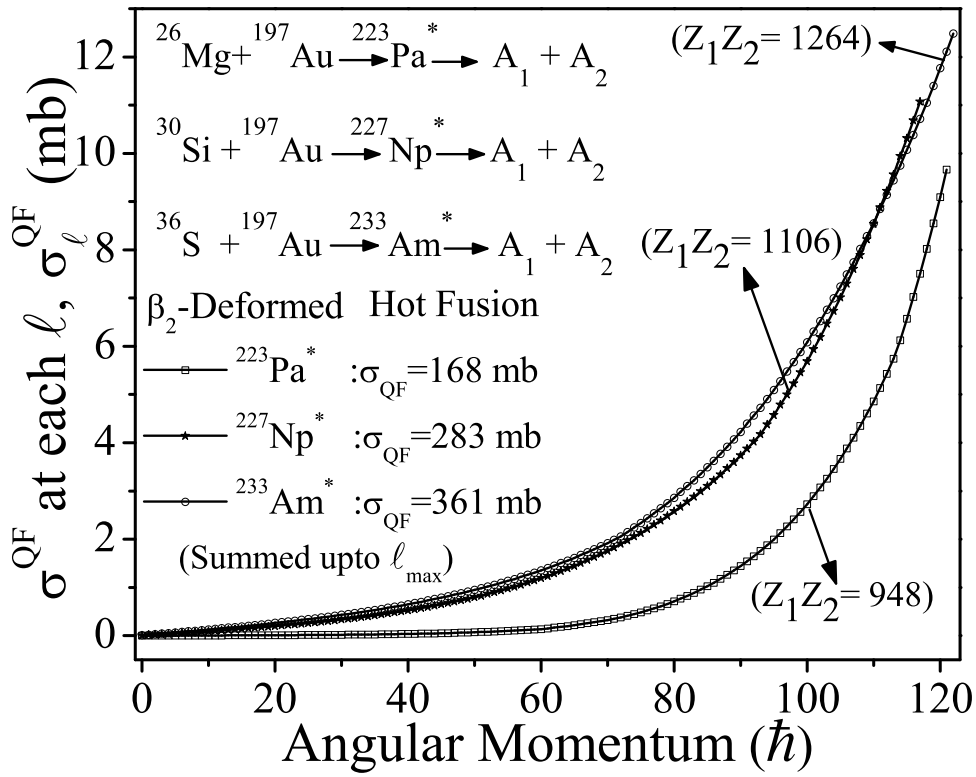

Figure 6.7 Individual contribution of quasi fission cross-section (σ_{QF}^{DCM}) plotted as a function of angular momentum ($\hbar$) for β_2-deformed choice of fragmentation.

60 MeV) and involve unique target nucleus ^{197}Au. Also, for the chosen set of reactions, the projectile and target charge product (Z_PZ_T), changes being 948 for ^{26}Mg, 1106 for ^{30}Si and 1264 for ^{36}S induced reactions. Thus one may observe that with the increase in charge of projectile (Z_P), the product Z_PZ_T increases, which inturn leads to higher chances of presence of quasi fission. It is observed that at maximum Z_PZ_T which is 1264 for ^{233}Am*, the contribution of quasi fission is maximum for almost all ℓ-values and decreases as the Z_PZ_T product decreases. Moreover, the effect of charge product is visible at ℓ-values>20 but remain silent at lower ℓ-values.

To converge the study of odd heavy mass nuclei, the comparative decay profile of ^{227,223}Pa* isotopes and that of isobaric nuclei ^{227}Pa* and ^{227}Np* has been studied in reference to [36]. Fig. 6.8(a,b) depicts the variation of fragmentation potential and preformation probability of ^{227,223}Pa* isotope formed in ^{19}F+^{208}Pb and ^{26}Mg+^{197}Au reactions at

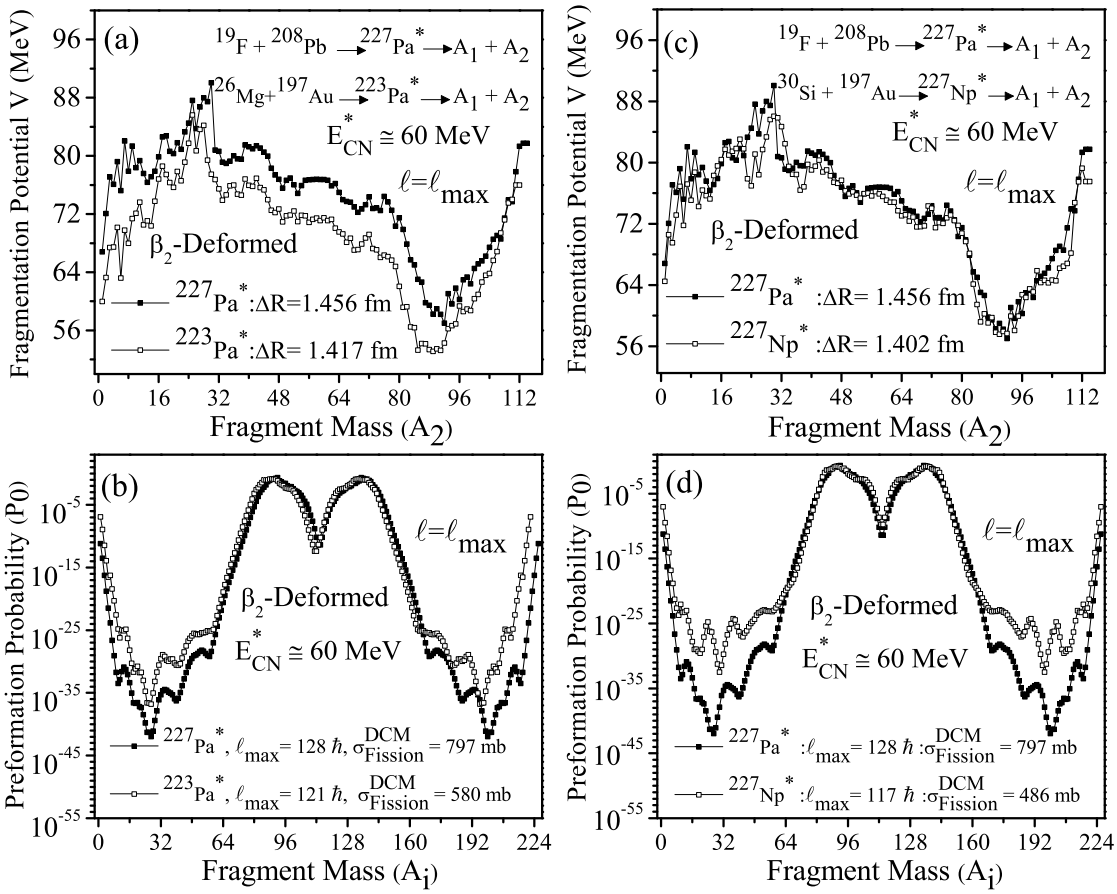

Figure 6.8 Comparison of fragmentation potential and preformation probability of ^{227,223}Pa* isotopes plotted in (a,c) and isobaric nuclei ^{227}Pa* and ^{227}Np* plotted in (b,d).

E^*_{CN}=60 MeV. It is observed that the structure of PES and mass distribution is nearly identical for both the isotopes. Amongst both of them, the neutron deficient nucleus has lower neck length parameter (ΔR=1.417 fm) and angular momentum value (ℓ=121ħ) as compared to heavier isotope. Also, the contribution of fission cross section increases with increase in isotopic mass. It is worth noting that DCM calculated fission cross sections for neutron rich ^{227}Pa* isotope is 797 mb which is less than the reported experimental cross section of 958 mb. This suggest that analogous to ^{223}Pa* isotope studied earlier, the neutron rich ^{227}Pa* isotope also involves contribution of quasi fission process. Since, the charge product of incoming channel for ^{227}Pa* (Z_PZ_T=738) is smaller than that for

^{223}Pa* isotope (Z_PZ_T=948), the relative contribution of quasi fission ought to be lower for neutron rich ^{227}Pa* isotope ($\sigma^{DCM}_{Quasifission}$=161 mb) as compared to neutron deficient ^{223}Pa* isotope ($\sigma^{DCM}_{Quasifission}$=168 mb). Besides this, the role of charge product has also been explored for isobaric nuclei-^{227}Pa* and ^{227}Np* formed in ^{19}F+^{208}Pb and ^{30}Si+^{197}Au reactions at similar excitation energy, i.e. $E^{*}_{CN}\cong$60 MeV. Figs. 6.8(c,d) represents the variation of fragmentation potential and preformation probability for the isobaric nuclei. No significant difference in structure is observed for both the nuclei. Furthermore, similar to the observation drawn from the isotopic analysis, the isobaric study shows that the quasi fission contribution is greater for neutron deficient ^{227}Np* ($\sigma^{DCM}_{Quasifission}$=283 mb) system with Z_PZ_T=1106 as compared to that for neutron rich ^{227}Pa* ($\sigma^{DCM}_{Quasifission}$=161 mb) system whose charge product of incoming channel is relatively lower (Z_1Z_2=738).

6.3 Summary

In this chapter, the explicit role of quadrupole (β_2) deformations has been studied for the heavy mass ^{215}Fr*, $^{223}Pa^{*}$, $^{227}Np^{*}$ and ^{233}Am* nuclei formed by striking different projectiles on oblate deformed target ^{197}Au at excitation energy, E^{*}_{CN}=60 MeV. The relative behavior of these nuclei has been investigated through potential energy surfaces, mass distribution and decay barrier height using collective clusterization approach. The fission cross-sections are estimated for both spherical and quadrupole (β_2) deformed choice of fragmentation. It has been noticed that for spherical approach, the magnitude of fragmentation potential is relatively more influenced by its fragment mass as compared to the corresponding centrifugal potential. In other words, the magnitude of fragmentation potential is governed by mass of compound nucleus formed irrespective of the magnitude of the angular momentum. Further, the deformations seem to play a significant role and their effect is more pronounced for IMF, HMF and fission region. Apart from this, the shell closure effect has also been looked upon. It has been observed that shell effects are more prominent for lighter mass projectiles. Further, the orientation degree of freedom studied

using DCM suggest the presence of competing QF process for $^{223}Pa^*$, $^{227}Np^*$ and $^{233}\mathrm{Am}^*$ nuclei. It is observed that mass fragment distribution becomes relatively symmetric when hot orientations are replaced by cold orientations. The oblately deformed shape of target may be responsible for this switching of behavior in the mass distribution. Furthermore, the contribution of quasi fission component has been examined for the transactinide nuclei. It has been noticed that as we move from asymmetric to symmetric incoming channel the QF component increases. This point is verified further by working out isotopic and isobaric analysis of nuclei.

After an extensive analysis of various decay outcomes for both compound and non compound nucleus processes shown in chapters 3-6, the summary and conclusions of the present work along with the future scope are given in the next chapter.

Bibliography

[1] R. Yanez, W. Loveland, J. S. Barrett, and L. Yao, *et al.*, Phys. Rev. C **88**, 014606 (2013).

[2] N. Grover, G. Kaur, and M. K. Sharma, Phys. Rev. C **93**, 014603 (2016).

[3] H. Q. Zhang, C. L. Zhang, C. J. Lin, Z. H. Liu, and F. Yang, *et al.*, Phys. Rev. C **81**, 034611 (2010).

[4] S. M. Mirfathi, and M. R. Pahlavani, Phys. Rev. C **78**, 064612 (2008).

[5] U. L. Businaro and S. Gallone, Nuovo Cimento **5**, 315 (1957).

[6] T. K. Ghosh, and K. Banerjee, *et al.*, Phys. Rev. C **79**, 054607 (2009).

[7] R. G. Thomas, *et al.*, Phys. Rev. C **77**, 034610 (2008).

[8] E. Prasad, *et al.*, Phys. Rev. C **81**, 054608 (2010).

[9] H. Q. Zhang, C. L. Zhang, C. J. Lin, A. K. Nasirov, G. Mandagleo, M. Manganaro, and G. Giardina, J. Phys. Conf. Ser. **282**, 012013 (2011).

[10] S. Appannababu, *et al.*, Phys. Rev. C **80**, 024603 (2009).

[11] E. Williams, D. J. Hinde, M. Dasgupta, *et al.*, Phys. Rev. C **88**, 034611 (2013).

[12] R. K. Gupta, M. Balasubramaniam, R. Kumar, D. Singh, C. Beck, Nucl. Phys. A **738**, 479c (2004); M. Kaur, and M. K. sharma, Eur. Phys. J. A **50**, 61 (2014).

[13] R. K. Gupta, S. K. Arun, R. Kumar, and M. Bansal, Nucl. Phys. A **834**, 176c (2010).

[14] M. Kaur, M. K. Sharma, and R. K. Gupta, Phys. Rev. C **86**, 064610 (2012); K. Sandhu, G. Kaur and M. K. Sharma, Nucl. Phys. A **921**, 114 (2014); G. Kaur and M. K. Sharma, Phys. Rev. C **87**, 044601 (2013).

[15] R. Kumar, K. Sandhu, M. K. Sharma, and Raj K. Gupta, Phys. Rev. C **87**, 054610 (2013); D. Jain, R. Kumar, M. K. Sharma, R. K. Gupta, Phys. Rev. C **85**, 024615 (2012).

[16] G. Sawhney and M. K. Sharma, Eur. Phys. J. A **48**, 57 (2012); G. Kaur and M. K. Sharma, Phys. Rev. C **87**, 044601 (2013); G. Kaur, D. Jain, R. Kumar, M. K. Sharma, Nucl. Phys. A **916**, 260 (2013).

[17] G. Sawhney, G. Kaur, M. K. Sharma, and R. K. Gupta Phys. Rev. C **88**, 034603 (2013).

[18] M. Kaur, R. Kumar, and M. K. Sharma, Phys. Rev. C **85**, 014609 (2012); K. Sandhu, M. K. Sharma and R. K. Gupta, Phys. Rev. C **85**, 024604 (2012).

[19] R. K. Gupta, M. Balasubramanium, R. Kumar, N. Singh, M. Manhas, and W. Greiner, J. Phys. G: Nucl. Part. Phys. **31**, 631 (2005); R. K. Gupta, M. Manhas, W. Greiner, Phys. Rev. C **73**, 054307 (2006).

[20] G. Kaur, N. Grover, K. Sandhu, M. K. Sharma, Nucl. Phys. A **927**, 232 (2014).

[21] M. G. Itkis, *et al.*, Nucl. Phys. A **734**, 136 (2004).

[22] A. M. Stefanini, *et al.*, Eur. Phys. J. A **23**, 473 (2005).

[23] R K Gupta and W Greiner , in *Heavy Elements and Related New Phenomenon*, edited by W. Greiner and R. K. Gupta (World Scientific, Singapore) Vol. **I**, Chapter 14, p. 536 (1999).

[24] J Maruhn and W Greiner, Z. Phys. **251**, 431 (1972); R K Gupta, W Scheid and W Greiner, Phys. Rev. Lett. **35**, 353 (1975).

[25] R. K. Gupta, M. K. Sharma, S. Singh ,R. Nouicer and C. Beck, Phys. Rev. C **56**, 3242 (1997); R. K. Gupta, M. K. Sharma, N. V. Antonenko and W. Scheid, J. Phys. G: Nucl. Part. Phys. **25** L47 (1999); M. K. Sharma, R. K. Gupta and W. Scheid, J. Phys. G: Nucl. Part. Phys. **26**, L45 (2000).

[26] N. J. Davidson, S. S. Hsiao, J. Markram, H. G. Miller, Y. Tzeng, Nucl. Phys. A **570**, 61c (1994).

[27] R. K. Gupta, R. Kumar, N. K Dhiman, M. Balasubramaniam, W. Scheid, C. Beck, Phys. Rev. C **68**, 014610 (2003); B. B. Singh, M. K. Sharma, and R. K. Gupta, Phys. Rev. C **77**, 054613 (2008).

[28] G. Audi, A. H. Wapstra, C. Thiboult, Nucl. Phys. A **729**, 337 (2003); G. Audi, A. H. Wapstra, Nucl. Phys. A **595**, 4 (1995).

[29] W. Myers, W. J. Swiatecki, Nucl. Phys. **81**, 1 (1966).

[30] G. Royer, J. Mignen, J. Phys. G: Nucl. Part. Phys. **18**, 1781 (1992).

[31] P. Möller, J. R. Nix, W. D. Myers, W. J. Swiatecki, At. Data Nucl. Data Tables **59**, 185 (1995).

[32] J. Blocki, J. Randrup, W. J. Swiatecki, and C. F. Tsang, Ann. Phys. (NY) **105**, 427 (1977).

[33] M. K. Sharma, S. Kanwar, G. Sawhney, and R. K. Gupta, Phys. Rev. C **85**, 064602 (2012).

[34] K. Nishio, H. Ikezoe, S. Mitsuoka, I. Nishinaka, Y. Nagame, Y. Watanabe, T. Ohtsuki, K. Hirose, and S. Hofmann, Phys. Rev. C **77**, 064607 (2008); K. Sandhu, M. K. Sharma, and R. K. Gupta, ibid. **86**, 064611 (2012).

[35] V. Zagrebaev, Phys. Rev. C **64**, 034606 (2001); V. Zagrebaev and W. Greiner, J. Phys. G: Nucl. Part. Phys. **34**, 1 (2007).

[36] M. B. Tsang, H. Utsunomiya, C. K. Gelbke, W. G. Lynch, B. B. Back, S. Saini, P. A. Baisden, and M. A. McMahan, Phys. Lett. B **129**, 18 (1983).

Chapter 7

Summary and outlook

In this thesis work, various decay mechanisms associated with both compound nucleus (CN) and non compound nucleus (nCN) processes are studied for an extensive mass range (A=45-235) of compound systems formed in heavy ion induced reactions at low energy regime. The CN mechanisms are studied by using both loosely bound and tightly bound projectiles, where for the reactions comprising of loosely bound projectiles, the comparative analysis of decay profiles corresponding to complete fusion (CF) and incomplete fusion (ICF) is investigated. Further, the relative contribution of CN and nCN component is explored in light and heavy mass region of periodic table. Also, the role of deformations, orientations, excitation energy, angular momentum, and iso-spin (N/Z ratio) is investigated. A brief introduction of different nuclear reactions and corresponding decay mechanisms studied in the present work is given in the chapter 1. This chapter gives an overview and current status of research in related area of nuclear physics. The methodology used to pursue the present work is the Dynamical Cluster-decay Model (DCM) and is described in chapter 2. DCM is originated from the dynamical (or quantum mechanical) fragmentation theory. In this approach, all decay processes are taken as the dynamical collective mass motion of preformed fragments through the interaction barrier and thus it estimates the relative probability of all the decay channels by treating them on equal footing. The decay analysis of different compound systems in DCM framework

is presented in chapters 3-6.

Firstly, the DCM has been employed to study the dynamics of ^{118,120,122}Xe* isotopes in chapter 3. In this chapter, the decay profiles of aforementioned isotopes of Xenon formed in ^{28}Si + ^{90,92,94}Zr reactions are discussed over an extensive range of center-of-mass energy varying from $E_{c.m.}$= 63.3 - 93.5 MeV, which is a spread across the Coulomb barrier. Here, the role of deformations is examined for ^{122}Xe* by studying the behavior of fragmentation potential at two extreme energies. It has been noticed that the barrier characteristics and potential energy surfaces get influenced with the inclusion of quadrupole deformations (β_{2i}) and hexadecapole (β_{2i-4i}) deformations. This impact of deformations is relatively more significant at lower energy as compare to higher energies. Further, the influence of isospin (N/Z ratio) is studied for ^{118,120,122}Xe* isotopes through the variation of fragmentation potential and preformation probability (P_0) at two comparable energies ($E_{c.m} \sim$ 65.0 and 89.0 MeV). The comparative analysis of these isotopes reveals that the decay probability is highest for ^{122}Xe* as its fragmentation potential is minimum of all. The mass distribution is found to be symmetric for all isotopes. The Evaporation Residue (ER) decay cross-sections show nice agreement with the experimental fusion cross-sections. The neck length parameter used to address the ER decay cross section increases with increase in energy and hence the barrier lowering parameter decreases with increase in energy. This inturn suggest that the lesser barrier modification is requisite at higher energies, which is responsible for the fair addressal of experimental data. Also, the role of projectile beam is examined in context to ^{118}Xe* and ^{123}Ba* nuclei, by changing the projectile ^{28}Si with ^{33}S. It is observed that for both nuclei, the light fragments are more favored at minimum ℓ-value and the change in projectile does not affect the relative contribution of ER fragments. Finally, the ER cross-sections for ^{118,120}Xe* isotopes are predicted at extreme energies, $E_{c.m.}$=63.3 and 93.5 MeV. Additionally, the cross sections for neighboring isotopes of Xe i.e. ^{116,124}Xe* are predicted at four center of mass energies ($E_{c.m.}\approx$72, 73, 75, 76 MeV), which may be verified in future experiments.

After analyzing the decay mechanisms of compound nuclei formed through CF, the

DCM is further applied to explore the dynamics of ICF and thus to present the comparative analysis of CF and ICF component in chapter 4. This chapter deals with the decay profiles associated with complete and incomplete fusion for ^{6}Li and ^{17}F induced reactions. The decay paths of both processes are examined using various components of DCM such as fragmentation potential V(A_2), preformation probability (P_0), and barrier height etc. Firstly, the dynamics of ^{6}Li + ^{159}Tb reaction reveals that there is not much difference in the structure of potential energy surfaces as we move from CF to ICF, except for some minor changes in the HMF and fission region. The CF and ICF cross sections within the DCM framework find nice accordance with the experimental data, and the emergence of larger neck for CF channel is possibly due to the smaller size of the composite system formed in ICF. Next, the decay patterns of both processes for ^{17}F+^{58}Ni reaction show similar observation as obtained for ^{6}Li induced reaction, i.e. the structure of potential energy surfaces of fragments is almost homogeneous for both CF and ICF; however, the magnitude of fragmentation potential is significantly influenced, which in turn influences the preformation probability of fragments. Further, to have deeper insight of the comparative analysis of CF and ICF, four decay modes (ER, IMF, HMF and fission) are studied separately for ^{17}F+^{58}Ni reaction. It is observed that for both CF and ICF channel, the preformation probability of ER is the highest amongst all and the contribution of HMF and fission is almost negligible for both the processes. The CF and ICF cross-sections estimated for ^{17}F+^{58}Ni reaction find fair agreement with the available data. The neck length parameter used to address the cross-sections is smaller for ICF channel (as observed for ^{6}Li + ^{159}Tb) and therefore higher magnitude of barrier modification is required for ICF as compared to CF. Besides above, the role of temperature-dependent pairing strength is analyzed for ^{17}F induced reaction. It is observed that 4n-clusters are more dominant in the decay modes estimated using the modified temperature-dependent pairing coefficient. After studying the CN mechanisms in chapter 3 and 4, DCM is further extended to explore the nCN component in the form of deep inelastic collisions (DIC) and quasi fission (QF) processes. These processes occur prior to the formation of equilibrated compound

system and the dynamics of these mechanisms is investigated in chapters 5 and 6.

In chapter 5, the contribution of nCN process is investigated for light mass composite system, $^{47}V^*$ formed in a ^{20}Ne + ^{27}Al reaction over an extensive span of center of mass energy ($E_{c.m.}$=83-125 MeV). It is noticed that there is strong competition between FF (CN) and DIC (nCN) components in the decay of $^{47}V^*$ composite system. Hence, analysis of both FF and DIC mechanisms is studied in framework of DCM. All calculations are done for quadrupole (β_{2i}-deformed) choice of fragments and the cross-sections are addressed by optimizing the neck length parameter (ΔR) of DCM. The behavior of fragmentation potential, preformation probability, penetrability and emission time etc. is explored to identify the most favorable decay fragments for both FF and DIC. It is observed that the structure of potential energy surfaces and mass distribution of fragments does not depend upon the incident energy. Further, the DCM calculations suggest that the most favourable fragments are the isotopes lying in the range varying as $3 \leq Z_2 \leq 9$ ($5 \leq A_2 \leq 19$). The fragments identified, match with the ones reported in the experimental data. From all isotopes lying in the specified region, fragments having equal number of protons and neutrons (N=Z) are found to contribute the most. Furthermore, the penetrability of fragments decreases with increase in mass of fragment and increases with increase in the angular momentum. The cross-sections estimated for both FF and DIC agree well with the experimental data. Also, it is pertinent to inscribe here that the ℓ-window to address the cross-sections is $0 \leq \ell \leq \ell_{cr}$ for FF and $\ell_{cr} \leq \ell \leq \ell_{gr}$ for DIC. Additionally, σ_{FF} and σ_{DIC} are predicted at three center of mass energies ($E_{c.m.}$=93, 98, and 103 MeV) by fitting the cubic polynomial for ΔR with center of mass energy as variable, which can be verified by future experiments. At last, the emission times computed using DCM are observed to be in nice accordance with the reported data. In view of above, one can say that the DCM based calculations describe FF and DIC nicely over an extensive spread of incident energies.

Next, to extend the analysis of nCN processes in DCM framework, chapter 6 aims to explain such process in heavy mass range of composite systems. To accomplish this,

the dynamics of $^{215}Fr^*$, $^{223}Pa^*$, $^{227}Np^*$ and $^{233}Am^*$ nuclei is studied in view of fission and quasi fission (QF), where QF represent the nCN process observed in heavy mass nuclei. In this chapter, the decay pattern and related behavior of $^{215}Fr^*$, $^{223}Pa^*$, $^{227}Np^*$ and $^{233}Am^*$ nuclei is explored at common excitation energy, E^*_{CN}=60 MeV. The relative behavior of the aforementioned nuclei is investigated through the fragmentation potential, mass distribution and decay barrier height using the collective clusterization approach of DCM. To study the explicit role of deformations, calculations are made for both spherical and quadrupole (β_2) deformed choice of fragmentation. It is noticed that the deformations play a significant role and their effect is more pronounced for IMF, HMF and fission region. This observation is consistent with that obtained earlier for $^{122}Xe^*$ nucleus in chapter 3. Besides this, the shell closure effect for $^{223}Pa^*$, $^{227}Np^*$ and $^{233}Am^*$ nuclei formed by striking distinct projectiles (with mass A=18-36) on oblate deformed target ^{197}Au is also explored. It is observed that shell effects are more prominent for lighter mass projectiles. Further, the study regarding the role of orientation degree of freedom show the competing nature of QF in the decay of given nuclei. The mass fragment distribution becomes relatively symmetric when hot orientations are replaced by cold orientations. This may be due to the oblately deformed shape of target nucleus. Furthermore, it is observed that the contribution of QF component is absent in the decay of pre-actinide nucleus, $^{215}Fr^*$. Thus, the contribution of quasi fission cross-sections is examined for $^{223}Pa^*$, $^{227}Np^*$ and $^{233}Am^*$ nuclei. It has been observed that as we move from asymmetric to symmetric incoming channel, the QF component increases. This point is verified further by working out isotopic ($^{223}Pa^*$, $^{227}Pa^*$) and isobaric ($^{227}Pa^*$, $^{227}Np^*$) analysis of nuclear systems.

By compiling the above discussion, it can be concluded that the present thesis work exhibits a comprehensive picture of the decay analysis associated with both CN and nCN mechanisms over an extensive spread of incident energies. Thorough analysis of CF and ICF decay is analyzed in terms of ER, IMF, HMF and fission for CN channel, whereas DIC and QF components are addressed in view of nCN decay. However, there is always a possible scope to extend the research work. Thus, the present study can also be

carried forward or it can serve as a groundwork for further research in the relevant area. The DCM can be refined further to explore other breakup processes such as sequential complete fusion (SCF), transfer and stripping mechanisms etc. Further, the nCN analysis can also be extended further to study fast fission (ff) and pre-equilibrium fission (PEQ) mechanisms. Also, it is relevant to mention here that the present work is limited to primary decay fragments only, thus it would be interesting to explore the secondary particle emission in DCM framework.